Die approbierte Originalversion dieser Diplom-/Masterarbeit ist an der Hauptbibliothek der Technischen Universität Wien aufgestellt (http://www.ub.tuwien.ac.at).

The approved original version of this diploma or master thesis is available at the main library of the Vienna University of Technology (http://www.ub.tuwien.ac.at/englweb/).

TECHNISCHE UNIVERSITÄT WIEN

VIENNA UNIVERSITY OF TECHNOLOGY

DIPLOMARBEIT

Simulation of Quantum Transport Using the Non-Equilibrium Green's Functions Formalism

ausgeführt zum Zwecke der Erlangung des akademischen Grades eines Diplom-Ingenieurs unter der Leitung von

Ao.Univ.Prof. Dipl.-Ing. Dr.techn. Tibor Grasser

und

Dipl.-Ing. Markus Karner

E360 - Institut für Mikroelektronik

eingereicht an der Technischen Universität Wien

Fakultät für Elektrotechnik und Informationstechnik

von

Oskar Baumgartner

0125546 / E 066 439

Schloßstraße 64, 3550 Gobelsburg
eMail: oskar.baumgartner@iue.tuwien.ac.at

Wien, im Dezember 2006

Kurzfassung

Durch den rapiden Fortschritt der Mikroelektronik haben die charakteristischen Größen der realisierten Bauteile Dimensionen im Nanometerbereich erreicht. Dadurch treten quantenmechanische Effekte auf, die die Leistungsmerkmale der modernen Bauelemente entscheidend beeinflussen. Das stellt neue Herausforderungen an die Modellierung und Simulation der Halbleiterbauelemente, da semi-klassische Modelle nur empirische, quantenmechanische Korrekturen beinhalten.
Die Wellennatur der Elektronen in quantenmechanischen Systemen bedarf einer korrekten Beschreibung durch die Schrödingergleichung. Für die Darstellung des Quantentransports mussten fortschrittliche, physikalische Modelle, die offene Randbedingungen stellen, entwickelt werden.
Das Themengebiet der Greenschen Funktionen, die ein generelles Konzept zur Lösung von inhomogenen Differentialgleichungssystemen bieten, wird schrittweise aufgerollt. Alle Annahmen und Näherungen, die gemacht wurden, um stationären Transport unter Zuhilfenahme der Greenschen Funktionen Methode zu beschreiben, werden besonders hervorgehoben. Weiters wird der Übergang von einer generellen Quantentransporttheorie, die die Nichtgleichgewichts Greenschen Funktionen verwendet, hin zu einer numerischen Implementierung in einer rechnerunterstützten Simulation näher untersucht.
Im Zuge dieser Diplomarbeit wurde der Nichtgleichgewicht Greensche Funktionen Formalismus verwendet, um die Phänomene des Quantentransports zu simulieren. Der *Vienna Schrödinger Poisson-Gleichungslöser*, der am Institut für Mikroelektronik der Technischen Universität Wien entwickelt wurde, wurde um ein Modul zur Lösung eindimensionaler Nichtgleichgewichts Greenschen Funktionen erweitert. Die Schrödingergleichung in der effektiven Massennäherung wird im Rahmen des Greenschen Funktionen Formalismus behandelt und konsistent mit der Poissongleichung gelöst. Die Implementierung ermöglicht ebenso zukünftige Erweiterungen, um Effekte wie Streuung oder komplexere Bandstrukturen zu berücksichtigen. Die Simulation von ballistischem Transport in einer resonanten Tunneldiode wurde durchgeführt. Der Gleichungslöser liefert die lokale Zustandsdichte und Besetzung im Simulationsgebiet. Die erlangten Strom-Spannungs Kurven zeigen den typischen negativen differentiellen Widerstand der resonanten Tunneldiode.

Abstract

With the continuous progress of microelectronics, the featured structure size has been scaled down to the nanometer regime. Therefore, quantum mechanical effects significantly influence the characteristics of state-of-the-art devices. This poses new challenges to the modeling and simulation of semiconductor devices, since semi-classical models only allow to incorporate empirical quantum corrections.
The wavelike nature of the electrons in quantum mechanical systems requires a proper treatment by the Schrödinger equation. For quantum transport very elaborate physical models posing open boundary conditions have been developed.
The subject of Green's functions, which are a general concept to solve for inhomogeneous differential equation systems, is approached gradually. All assumptions and approximations that have been made to allow a numerical treatment of steady-state transport within the non-equilibrium Green's functions (NEGF) method are pointed out. The intersection of a general quantum transport theory using Green's functions and its numerical implementation within a computer simulation is examined in detail.
In this diploma thesis the NEGF formalism has been used to simulate quantum transport phenomena. The Vienna Schrödinger Poisson solver, developed at the Institute for Microelectronics at the Technical University of Vienna, has been extended with a one-dimensional non-equilibrium Green's functions solver. The effective mass Schrödinger equation is treated within the NEGF framework and solved self-consistently with the Poisson equation. The implementation allows for future improvements especially considering scattering events and more complicated bandstructures. The simulation of ballistic transport in resonant tunneling devices was performed. The NEGF solver provides the local density and occupation of states within the simulation domain. Furthermore, the current-voltage curves showing the characteristic negative differential resistance were obtained.

Acknowledgment

Foremost, I want to thank Prof. Erasmus Langer and Prof. Siegfried Selberherr for enabling my thesis in the domain of device simulation and for granting its financial support.

Furthermore, I value highly the special interest that was shown in my work by Prof. Hans Kosina and Mahdi Pourfath.

I thank Prof. Tibor Grasser for awakening my interest in semiconductor device simulation in the course of his lectures. He overwhelmed me with inquiries until I could no longer resist to meet this challenging topic in my thesis.

I would like to acknowledge the warm welcome of all the colleagues at the Institute for Microelectronics. I appreciate the many doors they opened for me. Most important, I thank Stefan Holzer for always having a helpful hand.

This diploma thesis would not exist without the everlasting support of my supervisor Markus Karner. I am deeply in debt to him and I hope that I adopted some of his endless optimism. I could not imagine a better and more competent advisor.

I want to thank everyone who shared my life through the last years, whether friendship or love, past or present. I am glad to have met so many different people during my studies. A lot of them left a permanent impression and hopefully some of them will further do so in the future.

Finally, I wish to express my gratitude to my parents, who let me cut my own path and supported every of my decisions as best they could. All the best and good luck to my not-so-little sister. A special thanks goes to my mother for the motivating conversations that helped me through some tough times.

Contents

List of Symbols **vi**
Notation . . . vi
Physical Quantities . . . vii
Constants . . . ix

List of Figures **x**

1 Introduction **1**

2 Theory of Open Quantum Systems **3**
2.1 The Schrödinger Equation . . . 3
2.1.1 Band Structure and Effective Mass Approximation . . . 4
2.1.2 Separation of the Schrödinger Equation . . . 6
2.2 Density of States and Occupation . . . 8
2.2.1 Density of States . . . 8
2.2.2 Occupation of States . . . 9
2.3 Transmission . . . 11
2.3.1 Transmission and Scattering Matrix . . . 12
2.3.2 Conductance - The Landauer Formula . . . 16
2.3.3 Resonant Tunneling . . . 18
2.4 Green's Function Method . . . 21
2.4.1 Introduction to Green's Functions . . . 21
2.4.2 Equilibrium Green's Functions . . . 24
2.4.3 Non-Equilibrium Green's Functions . . . 26
2.4.4 Scattering . . . 27

3 Numerical Methods **29**
3.1 Numerical Solution of Schrödinger Equation . . . 29
3.1.1 Closed Boundaries . . . 29

3.1.2 Open Boundaries . . . 31
3.2 Numerical Solution of NEGF . . . 32
3.2.1 Hamiltonian . . . 32
3.2.2 Discretization of Green's Functions . . . 33
3.2.3 Recursive Green's Function Algorithm . . . 35
3.2.4 Analogies to QTBM . . . 38
3.3 Adaptive Energy Integration . . . 38
3.3.1 Simpson's Rule . . . 39
3.3.2 Akima Interpolation . . . 40
3.3.3 Polynomial Interpolation . . . 41
3.3.4 Clenshaw-Curtis Integration . . . 43
3.3.5 Comparison of Integration Methods . . . 43
3.4 Self Consistent Solution . . . 44

4 Results **46**
4.1 Single Barrier . . . 46
4.2 Resonant Tunneling Diodes . . . 48
4.2.1 Linear Potential Drop . . . 48
4.2.2 Self Consistent Simulation . . . 52

5 Summary and Outlook **58**

Bibliography **59**

List of Symbols

Notation

x	Scalar
$\mathbf{x}$	Vector
$\tilde{x}$	Tensor
$\underline{\mathbf{X}}$	Matrix
X	Operator
$\lvert\Psi\rangle$	ket-vector
$\langle\Psi\rvert$	bra-vector
$\langle\Psi\rvert\mathrm{X}\lvert\Psi\rangle$	Matrix element X_{ij} of the operator X
$\underline{\mathbf{A}}^{\dagger}$	Hermitian conjugate of $\underline{\mathbf{A}}$
$\mathrm{Tr}\big(\mathrm{A}\big)$	Trace of A
$\langle\mathrm{A}\rangle$	Ensemble average of A
$\big[\mathrm{A},\mathrm{B}\big]$	Commutator of A and B
$\big\{\mathrm{A},\mathrm{B}\big\}$	Anti-commutator of A and B
$\delta(x)$	Dirac function
$\theta(x)$	Step function
∇	Nabla operator
$\nabla\cdot\nabla=\nabla^2=\Delta$	Laplace operator
∇x	Gradient of the scalar field x
$\nabla\cdot\mathbf{x}$	Divergence of the vector field $\mathbf{x}$
$\nabla\times\mathbf{x}$	Curl of the vector field $\mathbf{x}$
$\Re\{x\}$	Real part of x
$\Im\{x\}$	Imaginary part of x
$\mathfrak{P}\{x\}$	Principal part of x

Physical Quantities

Symbol	Unit	Description
$\mathbf{x}$, $\mathbf{r}$	m	Space vectors
x, r	m	Absolute vallue of space vectors
$\mathbf{k}$	m^{-1}	Wave vector
k	m^{-1}	Absolute value of the wave vector
t	s	Time
Ψ, ψ	m^{-n}	Wavefunction
φ_x	$\mathrm{m}^{-1/2}$	One-dimensional wavefunction
V	eV	Potential energy
$\mathcal{E}$	eV	Energy of a particle
ε_x	eV	Energy of a particle with wavefunction φ_x
ε_{tn}	eV	Energy of the state n
$\tilde{m}$	kg	Effective mass tensor
m_l	kg	Lateral effective mass
m_t	kg	Transversal effective mass
m_{yz}	kg	Density of states mass for the yz-plane
m_{xyz}	kg	Density of states mass for a three-dimensional system
ς	m^{-n}	Probability density for an n-dimensional system
ρ	$\mathrm{m}^{-n}\mathrm{eV}^{-1}$	Density of states for an n-dimensional system
ρ_x	$\mathrm{m}^{-1}\mathrm{eV}^{-1}$	Density of states for one-dimensional system (x-axis)
$\mathcal{E}_\mathrm{F}$	eV	Fermi level
$\mathcal{E}_\mathrm{C}$	eV	Conduction band edge
μ_i	eV	Chemical potential in lead i
ν_i	$\mathrm{m\ s}^{-1}$	Group velocity of electron gas in lead i
N_A	m^{-3}	Acceptor concentration
N_D	m^{-3}	Donor concentration
n	m^{-3}	Electron concentration
p	m^{-3}	Hole concentration
n_{n_x}	m^{-3}	Electron concentration of subband n_x
$\mathbf{j}$	$\mathrm{A\ m}^{-2}$	Current density
$T(\mathcal{E})$	1	Transmission probability
$R(\mathcal{E})$	1	Reflection probability
$\underline{\mathbf{M}}$	1	Transfer matrix
$\underline{\mathbf{S}}$	1	Scattering matrix
G_C	Ω^{-1}	Conductance
ϕ	V	Electrostatic potential
ϱ	A s	Space charge
$\tilde{\varepsilon}$	$\mathrm{AsV}^{-1}\mathrm{m}^{-1}$	Permittivity tensor
T	K	Temperature

Symbol	Unit	Description
G	1	Green's Function
G	eV^{-1}	Green's function in a discrete representation
G^{R}	1 / eV^{-1}	Retarded Green's function / discrete representation
G^{A}	1 / eV^{-1}	Advanced Green's function / discrete representation
$G^{<}$	1 / eV^{-1}	Lesser Green's function / discrete representation
$G^{>}$	1 / eV^{-1}	Greater Green's function / discrete representation
Σ^{R}	1 / eV	Retarded self-energy / discrete representation
Σ^{A}	1 / eV	Advanced self-energy / discrete representation
$\Sigma^{<}$	1 / eV	Lesser self-energy / discrete representation
$\Sigma^{>}$	1 / eV	Greater self-energy / discrete representation
Γ	eV	Energy broadening

Constants

h	Planck's constant	$6.6260755 \times 10^{-34}$ Js
$\hbar$	Reduced Planck's constant	$h/(2\pi)$
k_B	Boltzmann's constant	1.380662×10^{-23} JK^{-1}
m_0	Free electron mass	$9.1093897 \times 10^{-31}$ kg
q_0	Elementary charge	$1.6021892 \times 10^{-19}$ C

List of Figures

2.1 First Brillouin zone of silicon 5
2.2 Bandstructure of Silicon 6
2.3 Subbands 8
2.4 Fermi distribution 11
2.5 Single barrier 12
2.6 Transmission coefficient of a single barrier 14
2.7 Resonant tunneling state 18
2.8 Transmission coefficient for a double barrier 19
2.9 Schematic band edge diagram of a RTD 20
2.10 Excitation leading to the retarded Green's function 22
2.11 Excitation leading to the advanced Green's function 23

3.1 Discretization points on an equidistant one-dimensional grid 30
3.2 Illustration of the adaptive integration algorithm with grid refinement. Grid points are added as long as the error criterion is not met. 39
3.3 The deviation of two integration methods applied to the same integration interval is used as a local error criterion. 40
3.4 Points used to calculate the slope at point X_3 41
3.5 Self consistent calculation of potential and electron density 44

4.1 Local density of states of a single barrier 47
4.2 Occupied density of states of a single barrier 47
4.3 Transmission of a single barrier 48
4.4 Non-self-consistent local density of states of a RTD without bias 49
4.5 Non-self-consistent local density of states of a RTD under bias 50
4.6 Non-self-consistent occupied density of states of a RTD without bias . . . 50
4.7 Non-self-consistent occupied density of states of a RTD under bias 51
4.8 Transmission probability of a double barrier structure 51
4.9 Non-self-consistent calculation of the current-voltage curve of a RTD . . 52

4.10 Self-consistent local density of states of a RTD without bias 53
4.11 Self-consistent local density of states of a RTD under bias 54
4.12 Self-consistent occupied density of states of a RTD without bias 54
4.13 Self-consistent occupied density of states of a RTD under bias 55
4.14 Self-consistent band edge and carrier concentration of a RTD 55
4.15 Current density spectrum 56
4.16 Self-consistent calculation of the current-voltage curve of a RTD 57

Abandon all hope, you who enter here.

Dante Alighieri

CHAPTER 1

Introduction

Semiconductor industry has undergone a rapid development process through the last half century. It is best couched into terms by Moore's law stated by Gordon Moore, one of the co-founders of Intel. He predicted a doubling of the number of transistors in an integrated circuit every two years whereas the production costs would decrease by the same factor. Up until 2007, all encountered technological difficulties have been overcome and Moore's law is still valid. The pace in research and development to further continue on this path is set by the International Technology Roadmap for Semiconductors [1].
In the field of semiconductor device development, modeling and simulation are of increasing significance. Numerical simulation allows a deeper understanding of the physical processes within existing semiconductor devices and facilitates predictions for future developments. Computer simulations are no substitution to experiments but provide a valuable complement which give new insights to the physics within an iterative research process.
To accurately describe physical phenomena by numerical simulation the subjacent models have to be valid within the domain of application. For microelectronic devices, one effect of great interest is carrier transport. The simulation of transport in Metal-Oxide-Semiconductor (MOS) field effect transistors was dominated by the drift-diffusion model [2,3]. More advanced approaches considering higher order moments of the Boltzmann equation [4] allow to investigate hot carrier effects.
As device dimensions are going to hit the nanoscale, classical models fail due to emerging of quantum mechanical effects. Electrons show wavelike behavior and they are reflected or transmitted through finite barriers, i.e. tunneling occurs. Furthermore, electrons contained in a potential well lead to energy quantization. Unique effects such as resonances in double barrier structures are of growing interest for new devices. A wide range of different approaches to treat quantum mechanical transport phenomena have been proposed in the literature. For instance, they govern the solution of the Pauli master equation [5] or Monte Carlo methods to solve for the Wigner distribution function [6].

The approach presented in this thesis is called non-equilibrium Green's function (NEGF) method. Its roots go back to the sixties of the past century, where the foundation of the theory was developed by Kadanoff and Baym [7] and Keldysh [8]. In the last decade, increasing interest arose to apply Green's functions to device simulation because they enable computer simulations of resonant tunneling devices [9] and nanoscaled transistors [10].

Chapter 2 provides a compact overview of the theory of quantum transport. Furthermore, it points out the difficulties of open boundary conditions needed to describe transport phenomena. The Schrödinger equation is reviewed with regard to semiconductor device simulation. Therefore, the density and occupation of states are presented. A description of transmission through potential barriers has been given to facilitate the understanding of resonant tunneling devices, which is used as benchmark for the implementation of the non-equilibrium Green's function formalism presented at the end of the chapter.

In **Chapter 3**, the numerical methods to solve for the Schrödinger equation are summarized. The implementation of the NEGF method has been realized by means of a recursive algorithm. For comparison the quantum transmitting boundary method (QTBM) is illustrated. A great challenge is posed by the numerical integration methods which have been presented in further detail.

The results of the conducted simulations are given in **Chapter 4**. Plots of the local density of states, the occupation of states, and current-voltage curves are provided.

Finally, a summary and outlook for future developments are stated in **Chapter 5**.

To the electron:
may it never be of any use!

J. J. Thomson

CHAPTER 2

Theory of Open Quantum Systems

This chapter provides the necessary concepts of physics and mathematics that are essential for the treatment of open quantum mechanical systems. First, a brief introduction to the Schrödinger equation is given which finally will lead to the non-equilibrium Green's functions formalism.

2.1 The Schrödinger Equation

Approaching smaller and smaller dimensions classical mechanics based on Newton's law are no longer applicable to correctly describe the motion of the particles invoked. Therefore, quantum mechanics is necessary to obtain physical insight. Eighty years ago the formulation of Schrödinger's wave mechanics and Heisenberg's matrix mechanics provided the tools to understand the effects that can be seen regarding small particles such as electrons. Hence, it is unavoidable to apply quantum mechanics if one is interested in accurately describing the behavior of electrons in nanoscaled semiconductor devices. An introduction to this topic with emphasis on low-dimensional semiconductors is given by Davies [11].
In wave mechanics physical quantities are no longer given directly but have to be derived from the wave function Ψ. Since the wave functions only describe probabilities, quantum mechanical statistics have to be applied to obtain the expectation values of the desired quantities.
The one-dimensional time-dependent Schrödinger equation of a single particle under the influence of a varying potential $V(x)$ reads as

$$-\frac{\hbar^2}{2m}\frac{\partial^2}{\partial x^2}\Psi\left(x,t\right)+V\left(x\right)\Psi\left(x,t\right)=\imath\hbar\frac{\partial}{\partial t}\Psi\left(x,t\right). \tag{2.1}$$

In semiconductors the electrons are under the influence of the conduction band edge of the band structure and the applied electrostatic potential. Hence, the problem reduces

to the stationary case and the Schrödinger equation may be separated into a time-independent part $\psi(x)$ and a spatial-independent part $T(t)$:

$$\Psi(x,t) = \psi(x)\,T(t)\,. \tag{2.2}$$

Applying ansatz (2.2) to the time-dependent Schrödinger equation (2.1) leads to the equation system

$$\imath\hbar\frac{\partial}{\partial t}T(t) = \mathcal{E}T(t), \tag{2.3a}$$

$$-\frac{\hbar^2}{2m}\frac{\partial^2}{\partial x^2}\psi(x) + V(x)\psi(x) = \mathcal{E}\psi(x). \tag{2.3b}$$

The separation constant $\mathcal{E}$ can be identified as the energy of the particle. Equation (2.3b) is the one-dimensional time-independent Schrödinger equation. An expansion to three dimensions using the Laplace-operator $\nabla^2 = \frac{\partial^2}{\partial x^2} + \frac{\partial^2}{\partial y^2} + \frac{\partial^2}{\partial z^2}$ gives

$$\left(-\frac{\hbar^2}{2m}\nabla^2 + V(\mathbf{x})\right)\psi(\mathbf{x}) = \mathcal{E}\psi(\mathbf{x}). \tag{2.4}$$

An equivalent operator notation was introduced by Dirac. It combines all terms on the left-hand side of the Schrödinger equation into the Hamiltonian H which acts on the state $|\psi\rangle$ denoted by the infinitely-dimensional ket-vector.

$$\mathrm{H}|\psi\rangle = \mathcal{E}|\psi\rangle \tag{2.5}$$

2.1.1 Band Structure and Effective Mass Approximation

In semiconductors, the movement of electrons within the crystal is determined by the bandstructure. The periodicity of the lattice leads to a periodic potential. Hence, the Schrödinger equation can be solved by applying Bloch functions. This gives a wavevector for the electrons passing through the periodic lattice. For a face-centered cubic lattice, the reciprocal lattice which forms the Brillouin zone is body-centered cubic (Fig. 2.1). The dispersion relation of these electrons gives the band structure, which needs to be plotted within the first Brillouin zone in three-dimensional **k**-space. This can be done by defining directions between distinctive points in the Brillouin zone. There, the Γ-point defines the origin in **k**-space, X lies in the center of a square and L in the center of a hexagon. K is situated in the middle of an edge shared by two hexagons and U bisects the edge between a square and a hexagon. Finally, W is the intersection point of two hexagons and a square [11].
The bandstructure of silicon is shown in Figure 2.2. The dispersion relation is plotted along the secants between L, Γ, X, K and back to Γ. The full picture emerges by folding back higher Brillouin zones into the first one, which is called the reduced zone scheme. The gaps between different band edges are the so-called band gaps where classical propagation is not possible.

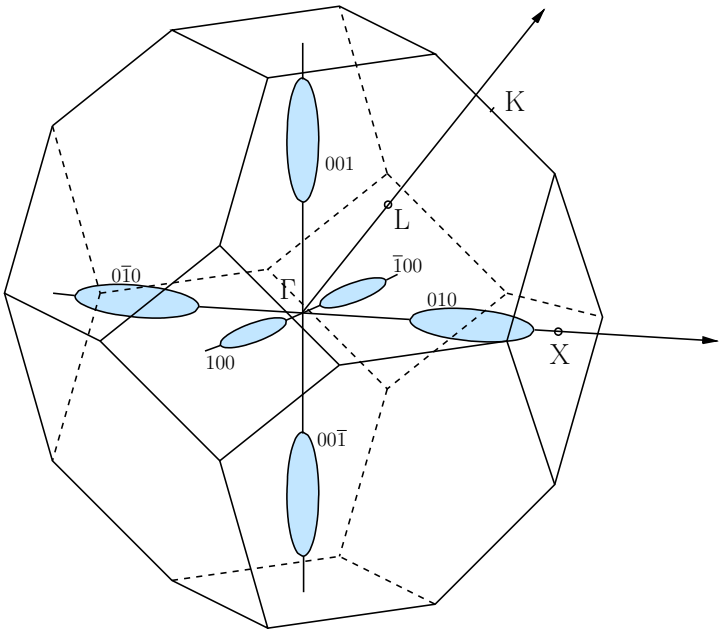

Figure 2.1: First Brillouin zone of silicon [12]. The significant points Γ, L, K , and X used in the band structure diagram of silicon are marked. Additionally, the equivalent energy surfaces of the three valley types forming ellipsoids and its minimum close to the X points are illustrated.

As shown in Fig. 2.2 the band structure has a very complex shape. Therefore, instead of a full description, a widely used concept, called effective mass approximation, is applied. The energy minimia in the bandstructure are called valleys. Around these a Taylor series expansion of the energy is performed. Thereby, the electron energy is approximated by

$$\mathcal{E}(\mathbf{k}) = \mathcal{E}(\mathbf{k}_{\min}) + \frac{\hbar^2}{2}\left[(\mathbf{k}-\mathbf{k}_{\min})^T \tilde{m}^{-1} (\mathbf{k}-\mathbf{k}_{\min})\right]. \tag{2.6}$$

The minimum energy of the valley is given by $\mathcal{E}(\mathbf{k}_{\min})$ and the curvature enters through the so-called effective mass tensor $\tilde{m}$ [12]. The inverse of this tensor is given by

$$\tilde{m}^{-1} = \frac{1}{\hbar^2}\begin{pmatrix} \frac{\partial^2\mathcal{E}}{\partial k_x^2} & \frac{\partial^2\mathcal{E}}{\partial k_x \partial k_y} & \frac{\partial^2\mathcal{E}}{\partial k_x \partial k_z} \\ \frac{\partial^2\mathcal{E}}{\partial k_y \partial k_x} & \frac{\partial^2\mathcal{E}}{\partial k_y^2} & \frac{\partial^2\mathcal{E}}{\partial k_y \partial k_z} \\ \frac{\partial^2\mathcal{E}}{\partial k_z \partial k_x} & \frac{\partial^2\mathcal{E}}{\partial k_z \partial k_y} & \frac{\partial^2\mathcal{E}}{\partial k_z^2} \end{pmatrix}. \tag{2.7}$$

The effective mass approximation to the band structure is reasonable for electrons with a low kinetic energy. It enters the Schrödinger equation by substituting the electron mass as follows:

$$\left(-\frac{\hbar^2}{2}\nabla\tilde{m}^{-1}\nabla + V(\mathbf{x})\right)\psi(\mathbf{x}) = \mathcal{E}\psi(\mathbf{x}). \tag{2.8}$$

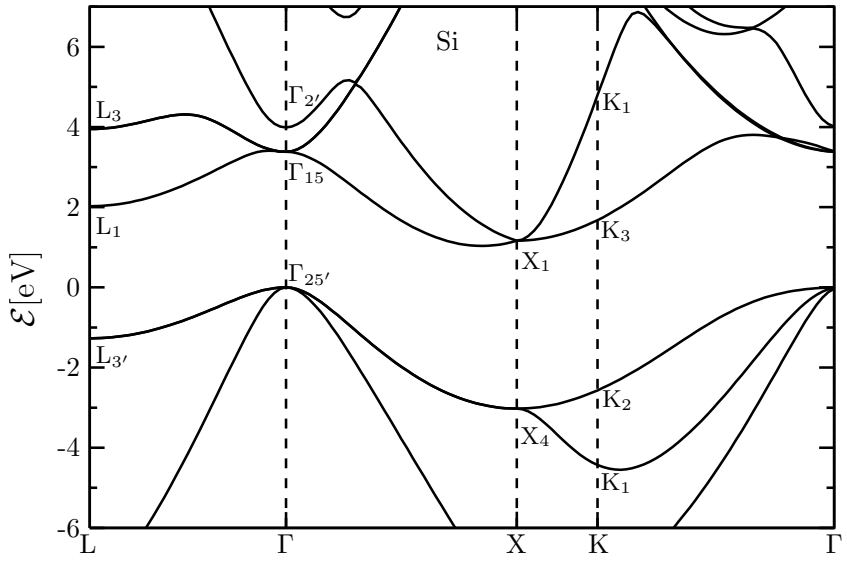

Figure 2.2: Bandstructure diagram of Silicon [13].

For some materials in certain directions, further simplifications are possible. The equivalent energy surface of the valleys of silicon form six ellipsoids, which can be described by a lateral and transversal mass m_l and m_t. According to their orientation, one can distinguish three valley types with a twofold degeneracy. The effective mass tensor for a silicon substrate with $\langle 100 \rangle$ orientation takes a diagonal form, given by

$$\tilde{m}^{-1} = \begin{pmatrix} \dfrac{1}{m_\mathrm{x}} & 0 & 0 \\ 0 & \dfrac{1}{m_\mathrm{y}} & 0 \\ 0 & 0 & \dfrac{1}{m_\mathrm{z}} \end{pmatrix}. \tag{2.9}$$

According to the orientation of the valley type, the coefficients equal $m_\mathrm{l} = 0.91 m_0$ and $m_\mathrm{t} = 0.19 m_0$, respectively. Hence, there are three different effective mass tensors conforming to the ellipsoids. Therefore, the Schrödinger equation needs to be solved three times and the solutions due to each valley have to be summed up.

2.1.2 Separation of the Schrödinger Equation

The geometrical structure of semiconductor devices often allows to reduce the simulation domain to a one-dimensional cross section of the device. For example, in heterostructures the electrons are not free to move in any direction. In a potential well their motion is confined perpendicular to the well and leads to discrete energy levels. The behavior of electrons bound to these discrete states is two-dimensional opposed to the continuous free or propagating states of higher energy than the confining potential well [14]. It is possible to separate the Schrödinger equation in a longitudinal and transversal part. The

general procedure will be shown in the following. Starting from the time-independent Schrödinger equation as derived in Section 2.1

$$\left(-\frac{\hbar^2}{2}\nabla\tilde{m}^{-1}(\mathbf{x})\nabla + V(\mathbf{x})\right)\psi(\mathbf{x}) = \mathcal{E}\psi(\mathbf{x}), \tag{2.10}$$

we are able to derive a formula that describes the motion of an electron in a low-dimensional system. We make use of the effective mass approximation and assume that the mass perpendicular to the heterostructure layers is $m_x(x)$ whereas the effective mass parallel to the layers is constant and therefore reads m_y and m_z respectively. Furthermore the electrostatic potential varies only normal to the heterostructure layers, i.e. $V(\mathbf{x}) = V(x)$. Hence, the Schrödinger equation reads

$$\left(-\frac{\hbar^2}{2}\frac{\partial}{\partial x}\frac{1}{m_x(x)}\frac{\partial}{\partial x} - \frac{\hbar^2}{2m_y}\frac{\partial^2}{\partial y^2} - \frac{\hbar^2}{2m_z}\frac{\partial^2}{\partial z^2} + V(x)\right)\psi(x,y,z) = \mathcal{E}\psi(x,y,z). \tag{2.11}$$

The following ansatz uses plane waves for the motion along y and z, which is plausible for a heterostructure with varying potential solely along the growth direction.

$$\psi(x,y,z) = \varphi_x(x)\exp(\imath k_y y)\exp(\imath k_z z). \tag{2.12}$$

Applying ansatz (2.12) to the Schrödinger equation (2.11) gives

$$\left(-\frac{\hbar^2}{2}\frac{\partial}{\partial x}\frac{1}{m_x(x)}\frac{\partial}{\partial x} + \frac{\hbar^2 {k_y}^2}{2m_y} + \frac{\hbar^2 {k_z}^2}{2m_z} + V(x)\right)\varphi_x(x) = \mathcal{E}\varphi_x(x). \tag{2.13}$$

The energy ε_x follows the solution φ_x of the one-dimensional Schrödinger equation, where

$$\varepsilon_x = \mathcal{E} - \frac{\hbar^2 {k_y}^2}{2m_y} - \frac{\hbar^2 {k_z}^2}{2m_z}. \tag{2.14}$$

Substituting (2.14) for the energy $\mathcal{E}$ in equation (2.13) yields

$$\left(-\frac{\hbar^2}{2}\frac{\partial}{\partial x}\frac{1}{m(x)}\frac{\partial}{\partial x} + V(x)\right)\varphi_x(x) = \varepsilon_x\varphi_x(x). \tag{2.15}$$

Therefore, the solution of the original three-dimensional problem can be rewritten with $\mathbf{r} = (y,z)$ and $\mathbf{k} = (k_y, k_z)$ and the effective mass of the y-z-plane m_{yz} to give

$$\psi_{\mathbf{k}}(\mathbf{r},x) = \exp(\imath\mathbf{k}\cdot\mathbf{r})\varphi_x(x), \tag{2.16a}$$

$$\mathcal{E}(\mathbf{k}) = \varepsilon_x + \frac{\hbar^2\mathbf{k}^2}{2m_{yz}}. \tag{2.16b}$$

Assuming closed boundary conditions implies discrete states as solution of (2.15) along the x-direction. For each quantum number n_x i.e. each allowed energy ε_x in x-direction, a dispersion relation (2.16b) for the y-z-plane holds. The wavefunctions, the parabolic dispersion relation and the stepwise growth of the electron density are illustrated in Figure 2.3. This introduces the concept of subbands.

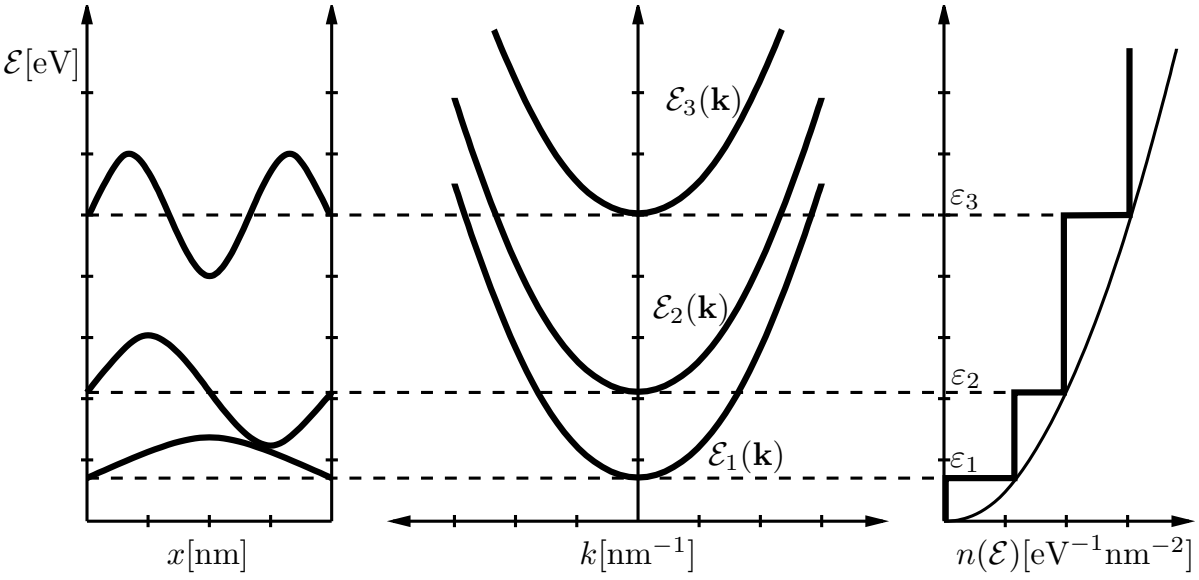

Figure 2.3: This diagram shows subbands corresponding to the discrete energy levels within a quantum confined system [11].

2.2 Density of States and Occupation

This section introduces the concept of the density of states and the distribution function. Together, they allow to determine the carrier concentration within a device.

2.2.1 Density of States

To be able to describe the number of states that are available in quantum mechanical systems the density of states $\rho(\mathcal{E})$ is defined. It gives the number of states within an energy range $[\mathcal{E}, \mathcal{E} + d\mathcal{E}]$ as $\rho(\mathcal{E})d\mathcal{E}$ [11]. The density of states is generally defined with Dirac delta functions $\delta(\mathcal{E})$

$$\rho(\mathcal{E}) = \sum_n \delta(\mathcal{E} - \varepsilon_n). \tag{2.17}$$

Each state n is accounted for by a Dirac function at its energy level ε_n. Therefore, the number of states within the energy range from $\mathcal{E}_1$ to $\mathcal{E}_2$ is given by the integration

$$Z = \int_{\mathcal{E}_1}^{\mathcal{E}_2} \rho(\mathcal{E})\mathrm{d}\mathcal{E} = \int_{\mathcal{E}_1}^{\mathcal{E}_2} \sum_n \delta(\mathcal{E} - \varepsilon_n)\mathrm{d}\mathcal{E} = \sum_n \int_{\mathcal{E}_1}^{\mathcal{E}_2} \delta(\mathcal{E} - \varepsilon_n)\mathrm{d}\mathcal{E}. \tag{2.18}$$

Equation (2.18) shows that due to the delta function only states within the given energy range contribute to the total sum of states, which is the desired property of the density of states.
The density of states for a free electron gas in one, two, and three dimensions are given

Dimension d	1D	2D	3D
$\rho_d(\mathcal{E})$	$\frac{1}{\pi\hbar}\sqrt{\frac{2m_{\mathrm{dos}}^{\mathrm{1D}}}{\mathcal{E}}}$	$\frac{m_{\mathrm{dos}}^{\mathrm{2D}}}{\pi\hbar^2}$	$\frac{m_{\mathrm{dos}}^{\mathrm{3D}}\sqrt{2m_{\mathrm{dos}}^{\mathrm{3D}}\mathcal{E}}}{\pi^2\hbar^3}$
n_d	$N_{\mathrm{C}}^{\mathrm{1D}}\mathcal{F}_{-\frac{3}{2}}\left(-\frac{\mathcal{E}_{\mathrm{C}}-\mathcal{E}_{\mathrm{F}}}{k_{\mathrm{B}}T}\right)$	$N_{\mathrm{C}}^{\mathrm{2D}}\ln\left(1+e^{\mathcal{E}_{\mathrm{F}}/k_{\mathrm{B}}T}\right)$	$N_{\mathrm{C}}^{\mathrm{3D}}\mathcal{F}_{\frac{1}{2}}\left(-\frac{\mathcal{E}_{\mathrm{C}}-\mathcal{E}_{\mathrm{F}}}{k_{\mathrm{B}}T}\right)$
N_{C}^{d}	$g_{\mathrm{S}}g_{\mathrm{V}}\left(\frac{m_{\mathrm{dos}}^{\mathrm{1D}}k_{\mathrm{B}}T}{2\pi\hbar^2}\right)^{1/2}$	$g_{\mathrm{S}}g_{\mathrm{V}}\frac{m_{\mathrm{dos}}^{\mathrm{2D}}k_{\mathrm{B}}T}{2\pi\hbar^2}$	$g_{\mathrm{S}}g_{\mathrm{V}}\left(\frac{m_{\mathrm{dos}}^{\mathrm{3D}}k_{\mathrm{B}}T}{2\pi\hbar^2}\right)^{3/2}$
m_{dos}^{d}	m_z	$m_{yz}=\sqrt{m_y m_z}$	$m_{xyz}=\sqrt[3]{m_x m_y m_z}$

Table 2.1: The density of states, the electron density, the effective density of states and the density of states mass are summarized for one-, two- and three- dimensional systems.

in Table 2.1. It shows a typical energy dependency of $\mathcal{E}^{-1/2}$ in one dimension, $\mathcal{E}^{1/2}$ in three dimensions and a constant behavior in two dimensions.
Equation (2.17) allows to describe the density of states of an arbitrary system. For systems, which are not translationally invariant, the density of states varies locally. Therefore, a local density of states is defined where every state is weighted by its wavefunction [11],

$$\rho(x,\mathcal{E})=\sum_n |\psi_n(x)|^2\delta(\mathcal{E}-\varepsilon_n). \tag{2.19}$$

The density of states can be recovered by employing a spatial integration

$$\rho(\mathcal{E})=\sum_n \delta(\mathcal{E}-\varepsilon_n)\int |\psi_n(x)|^2 dx=\sum_n \delta(\mathcal{E}-\varepsilon_n). \tag{2.20}$$

An even more general case of the density of states is the so-called spectral function

$$\rho(x,x',\mathcal{E})=\sum_n \psi_n(x)\psi_n^*(x)\delta(\mathcal{E}-\varepsilon_n). \tag{2.21}$$

This is an important quantity for the Green's functions formalism and will reappear later in the according sections governing the non-equilibrium Green's functions.

2.2.2 Occupation of States

After having calculated the number of available states, they have to be filled according to an occupation function. Fermions such as electrons need to obey the Pauli exclusion principle, which means that a state can only be occupied by a single particle at once.

Their behavior is described by the Fermi-Dirac distribution function

$$f\left(\mathcal{E}, \mathcal{E}_\mathrm{F}, T\right) = \frac{1}{1 + \exp\left(\dfrac{\mathcal{E} - \mathcal{E}_\mathrm{F}}{k_\mathrm{B} T}\right)} \tag{2.22}$$

where $\mathcal{E}_\mathrm{F}$ is the Fermi level, which is the energy at which the probability that the state is occupied equals the probability that it is empty. Figure 2.4 shows the Fermi-Dirac distribution function. Knowing the distribution function and the density of states it is possible to calculate the number of electrons within a quantum system according to

$$n = \int_{-\infty}^{\infty} \rho(\mathcal{E}) f\left(\mathcal{E}, \mathcal{E}_\mathrm{F}, T\right) \mathrm{d}\mathcal{E}. \tag{2.23}$$

Table 2.1 summarizes the density of electrons in a free electron gas with the given dimensionality. N_C is called the effective density of states in the conduction band which has the band edge at $\mathcal{E}_\mathrm{C}$. The effective masses m_{xyz} and m_{yz} are the respective density of states masses calculated form the coefficients of the effective mass tensor (see Section 2.1.1). The constant g_S gives the degeneracy due to the spin of the electrons, which is twofold (spin up and spin down). The degeneracy of equivalent valleys within a band is given by g_V. Equation (2.23) is of the same form as the so-called Fermi integrals and needs to be evaluated accordingly. The Fermi integral of order j is defined as

$$\mathcal{F}_j(\xi, \zeta) = \frac{1}{\Gamma(j+1)} \int_{\eta_1=\zeta}^{\eta_2=\infty} \frac{\eta^j}{1 + \exp\left(\eta - \xi\right)} \mathrm{d}\eta, \tag{2.24}$$

where $\Gamma(x)$ is the gamma function and

$$\eta = \frac{\mathcal{E} - \mathcal{E}_\mathrm{C}}{k_\mathrm{B} T}, \tag{2.25a}$$

$$-\xi = \frac{\mathcal{E}_\mathrm{C} - \mathcal{E}_\mathrm{F}}{k_\mathrm{B} T}. \tag{2.25b}$$

The complete Fermi integral used for the calculation of the electron density of the free electron gas requires a lower integration boundary of $\zeta = 0$.
In Section 2.1.2 it has been demonstrated, that it is possible to separate the Schrödinger equation, if the potential $V(\mathbf{x})$ meets some special constraints. If it were dependent on one spatial direction solely, the problem is split in a two-dimensional problem that describes the electron behavior within the subband itself and a one-dimensional problem that gives rise to these subbands. If a system with discrete states is occupied with electrons, each subband is filled sequentially. The number of electrons within a subband with index n_x, which is a two-dimensional electron gas, is therefore given by (cf. Table 2.1)

$$n_{n_x} = \frac{m_{yz} k_\mathrm{B} T}{\pi \hbar^2} \ln\left[1 + \exp\left(\frac{\mathcal{E}_\mathrm{F} - \varepsilon_{n_x}}{k_\mathrm{B} T}\right)\right]. \tag{2.26}$$

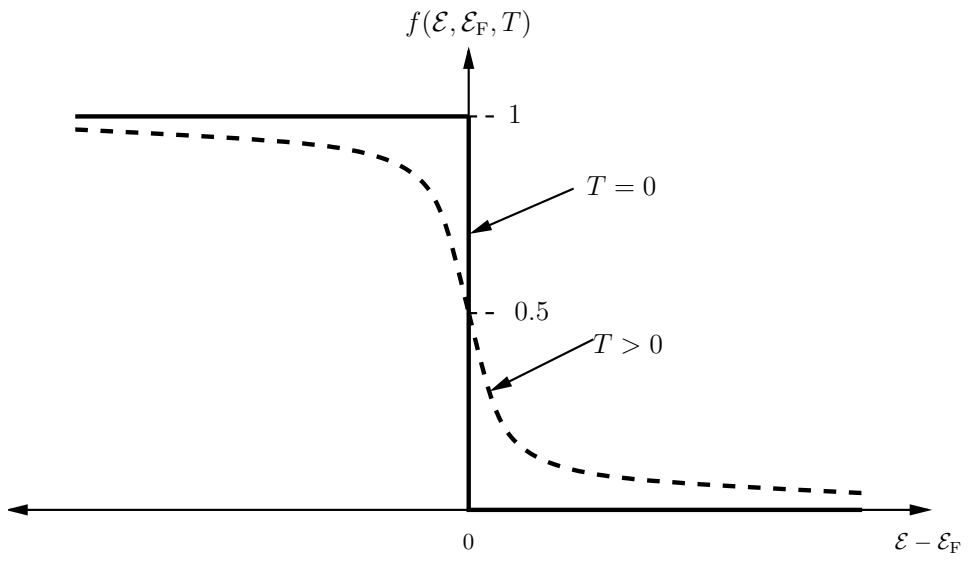

Figure 2.4: Fermi-Dirac distribution function for $T = 0$ K and $T > 0$ K. [12].

Now, the electron density of the complete system can be written as a summation over the electron contributions of all subbands

$$n = \sum_{n_x} n_{n_x} = \sum_{n_x} \frac{m_{yz} k_\mathrm{B} T}{\pi \hbar^2} \ln \left[1 + \exp\left(\frac{\mathcal{E}_\mathrm{F} - \varepsilon_{n_x}}{k_\mathrm{B} T} \right) \right]. \tag{2.27}$$

If the spectrum of states becomes continuous, the summation in equation (2.27) can be approximated as an integral. Instead of the discrete states, the density of states $\rho_x(\mathcal{E}_x)$ of a one-dimensional system arises. These states are filled according to two-dimensional subbands. Therefore, the electron density of these subbands can be interpreted as occupation function $f(\mathcal{E}_x)$ of the one-dimensional density of states $\rho_x(\mathcal{E}_x)$. The overall electron density is given by

$$n = \int_{-\infty}^{\infty} \rho_x(\mathcal{E}_x) \underbrace{\frac{m_{yz} k_\mathrm{B} T}{\pi \hbar^2} \ln \left[1 + \exp\left(\frac{\mathcal{E}_\mathrm{F} - \mathcal{E}_x}{k_\mathrm{B} T} \right) \right]}_{f(\mathcal{E}_x)} \mathrm{d}\mathcal{E}_x = \int_{-\infty}^{\infty} \rho_x(\mathcal{E}_\mathrm{x}) f(\mathcal{E}_x) \mathrm{d}\mathcal{E}_x, \tag{2.28}$$

where $\rho_x(\mathcal{E}_x)$ is acquired by solving the one-dimensional Schrödinger equation.

2.3 Transmission

After the discussion of the separation approach to reduce the Schrödinger equation to a one-dimensional problem, we will now focus on the transmission and reflection of particle waves incident perpendicularly on barriers within the transport direction [14, Chapter 3]. The simplest model of quantum transport in devices is to describe the problem in

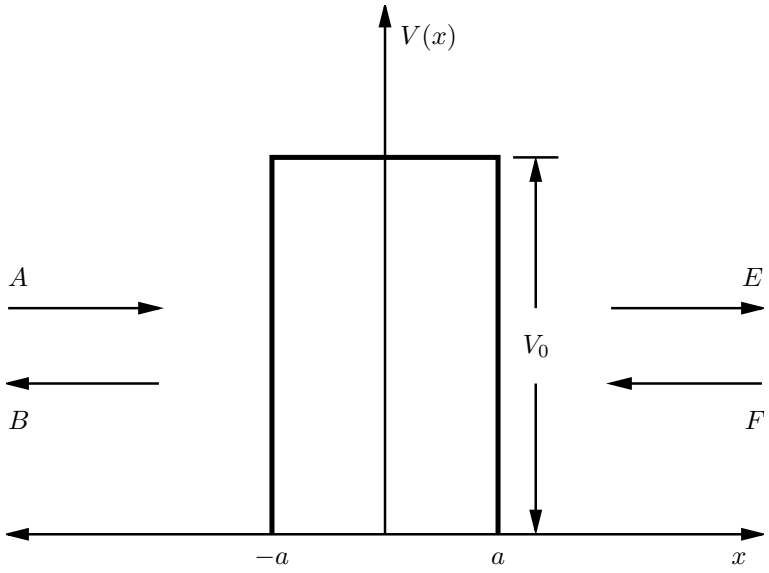

Figure 2.5: A single rectangular potential barrier

terms of the scattering of the electron wave by a spatially varying potential [15]. One assumes that this potential is situated inbetween two electron reservoirs, each emitting particles with an equilibrium distribution into the scattering region. An applied voltage causes two different chemical potentials within the contact regions. The flux of electrons passing between the reservoirs constitutes the electrical current conducted through the device.
In wave mechanics, the particle density is written as

$$\varsigma(\mathbf{x},t) = \Psi(\mathbf{x},t)\Psi^*(\mathbf{x},t). \tag{2.29}$$

Using this quantity, the Schrödinger equation can be rewritten in the form of a continuity equation for $\varsigma(\mathbf{x},t)$,

$$\frac{\partial\varsigma(\mathbf{x},t)}{\partial t} = -\frac{\hbar}{2m_0\imath}\nabla\cdot\left[\Psi^*(\mathbf{x},t)\nabla\Psi(\mathbf{x},t) - \Psi(\mathbf{x},t)\nabla\Psi^*(\mathbf{x},t)\right]. \tag{2.30}$$

With m_0 being the mass of an electron and q_0 the elementary charge, the electron current is given as

$$\mathbf{j} = \frac{\hbar q_0}{2m_0\imath}\left[\Psi^*(\mathbf{x},t)\nabla\Psi(\mathbf{x},t) - \Psi(\mathbf{x},t)\nabla\Psi^*(\mathbf{x},t)\right]. \tag{2.31}$$

2.3.1 Transmission and Scattering Matrix

A single potential barrier with the width $W = 2a$ and the height V_0 as depicted in Figure 2.5 will be considered next [14]. Regarding an electron coming from the left of

the barrier, the single particle Schrödinger equation with a single-band effective mass is again written as

$$\left(-\frac{\hbar^2}{2}\frac{\partial}{\partial x}\frac{1}{m_{\mathrm{x}}(x)}\frac{\partial}{\partial x}+V(x)\right)\psi(x)=\mathcal{E}\psi(x) \tag{2.32}$$

The solution of this equation may be written as piecewise-continuous function

$$\psi(x)=\begin{cases} A\exp(\imath kx)+B\exp(-\imath kx) & x<-a \\ C\exp(\gamma x)+D\exp(-\gamma x) & -a<x<a \\ E\exp(\imath kx)+F\exp(-\imath kx) & x>a \end{cases} \tag{2.33}$$

where

$$k=\frac{\sqrt{2m_x\mathcal{E}}}{\hbar}, \tag{2.34a}$$

$$\gamma=\frac{\sqrt{2m_x(V_0-\mathcal{E})}}{\hbar}. \tag{2.34b}$$

The coefficients A and B are associated respectively with incoming and outgoing waves on the left side relative to the barrier. Likewise, the coefficients E and F are outgoing and incoming waves on the right. For energies $\mathcal{E}<V_0$, the solutions in the barrier are exponentially decaying functions corresponding to evanescent states.
The coefficients C and D may be eliminated using the continuity of the envelope function and its derivative as boundary condition at the interfaces $x=-a$ and $x=a$. This leads to the matrix equation

$$\begin{bmatrix} A \\ B \end{bmatrix}=\begin{bmatrix} M_{11} & M_{12} \\ M_{21} & M_{22} \end{bmatrix}\begin{bmatrix} E \\ F \end{bmatrix} \tag{2.35}$$

where the matrix elements of the transfer matrix $\underline{\mathbf{M}}$ are given by

$$M_{11}=M_{22}^*=\left[\cosh(2\gamma a)-\frac{\imath}{2}\left(\frac{k^2-\gamma^2}{k\gamma}\right)\sinh(2\gamma a)\right]\exp(2\imath ka), \tag{2.36a}$$

$$M_{21}=M_{12}^*=-\frac{\imath}{2}\left(\frac{k^2+\gamma^2}{k\gamma}\right)\sinh(2\gamma a). \tag{2.36b}$$

The transmission and reflection coefficients are associated with the ratio of fluxes. Assuming that there is a wave incident from the left side with amplitude A and no wave from the right side we can set $F=0$. Using equation (2.31) we are able to calculate the probability flux incident to the barrier as

$$f_{\mathrm{inc}}=|A|^2\frac{\hbar k}{m_x}=v|A|^2, \tag{2.37}$$

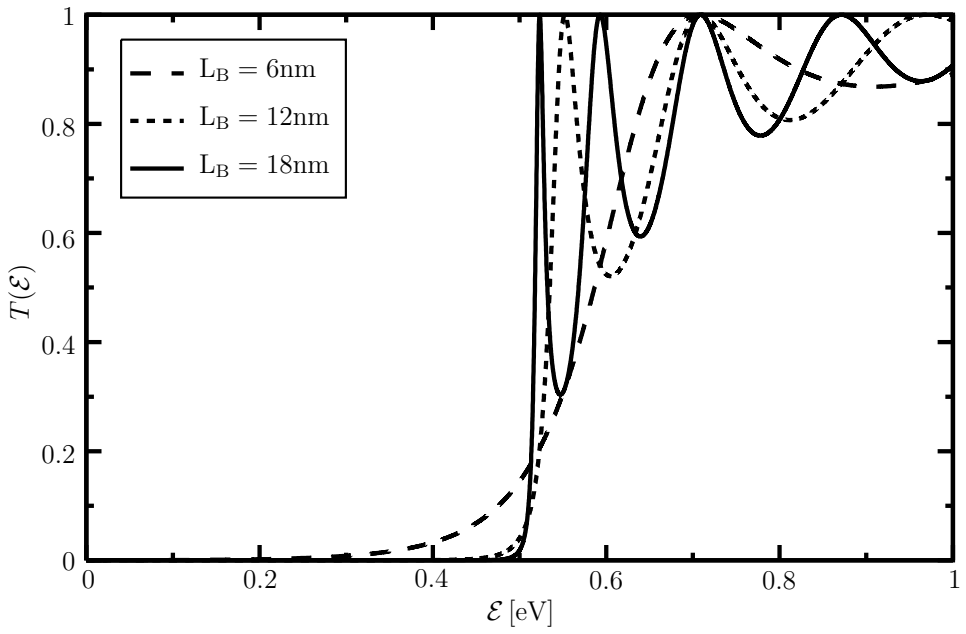

Figure 2.6: Transmission of a single barrier with a height of $V_0 = 0.5$ eV and three different widths.

where $v = (1/\hbar)dE/dk$ denotes the group velocity of a particle of wavevector k (here assuming parabolic bandstructure). For the transmitted wave the probability flux is

$$f_{\text{trans}} = |E|^2 \frac{\hbar k}{m_x} = v|E|^2. \tag{2.38}$$

Hence, the transmission coefficient, defined as the ratio of the transmitted to the incident probability flux density, writes

$$T(\mathcal{E}) = \frac{f_{\text{trans}}}{f_{\text{inc}}} = \frac{|E|^2}{|A|^2} = \frac{1}{|M_{11}|^2}. \tag{2.39}$$

The reflection coefficient is likewise defined as the ratio of the incident to reflected flux,

$$R(\mathcal{E}) = \frac{|B|^2}{|A|^2} = \frac{|M_{21}|^2}{|M_{11}|^2} = |M_{21}|^2 T(\mathcal{E}). \tag{2.40}$$

The transmission of a single barrier with a height of $V_0 = 0.5$ eV and three different widths is shown in Figure 2.6. The matrix equation (2.35) may be rewritten in a way, that it provides a relation between incoming and outgoing fluxes,

$$\begin{bmatrix} B \\ E \end{bmatrix} = \begin{bmatrix} S_{11} & S_{12} \\ S_{21} & S_{22} \end{bmatrix} \begin{bmatrix} A \\ F \end{bmatrix}. \tag{2.41}$$

Here, the matrix $\underline{\mathbf{S}}$ is referred to as the scattering matrix. The transmission and reflection coefficients are obtained as before. For $F = 0$ and the more general case of asymmetric

barriers which give different group velocities v_l for the left and v_r for the right side respectively, the coefficients result from

$$T(\mathcal{E}) = |S_{21}|^2 \frac{v_\mathrm{r}}{v_\mathrm{l}}, \tag{2.42a}$$

$$R(\mathcal{E}) = |S_{11}|^2. \tag{2.42b}$$

Equivalently, the transmission may be calculated for waves incident from the right by letting $A = 0$ which gives

$$T(\mathcal{E}) = |S_{12}|^2 \frac{v_\mathrm{l}}{v_\mathrm{r}}. \tag{2.43}$$

The transmission coefficients obtained are reciprocal and relate to the off-diagonal elements of the scattering matrix. The diagonal elements of the $\underline{\mathbf{S}}$-matrix are the reflection coefficients.
The properties of the scattering matrix are briefly summarized. Due to time reversal symmetry the matrix product of the scattering matrix and its complex conjugate is the unity matrix [14]

$$\underline{\mathbf{S}}^* \underline{\mathbf{S}} = \underline{\mathbf{I}}. \tag{2.44}$$

It follows from (2.44) that

$$|S_{11}|^2 + S_{12}^* S_{21} = 1, \tag{2.45}$$

which simply denotes the conservation of flux

$$T + R = 1. \tag{2.46}$$

To turn the scattering matrix into a unitary matrix

$$\underline{\mathbf{S}}^\dagger \underline{\mathbf{S}} = \underline{\mathbf{I}}, \tag{2.47}$$

the coefficients have to be normalized by the flux ratio $S_{ij}\sqrt{v_i/v_j}$ which leads to

$$\underline{\mathbf{S}} = \begin{bmatrix} r_\mathrm{l} & t_\mathrm{r} \\ t_\mathrm{l} & r_\mathrm{r} \end{bmatrix}. \tag{2.48}$$

The coefficients r_l and t_l denote the reflection and transmission amplitudes from left to right whereas r_r and t_r describe the opposite case from right to the left. The transmission and reflection coefficients are therefore given by $T = |t_\mathrm{l}|^2$ and $R = |r_\mathrm{l}|^2$. Further examples and a more detailed description are presented in [14].

2.3.2 Conductance - The Landauer Formula

If a system is near thermal equilibrium, i.e. the applied voltages are very small, transport can be described using linear response theory. One approach is the Kubo formalism which is based on the fluctuation-dissipation theorem [15–17]. It allows the calculation of the conductivity via the autocorrelation of the current density.
Another widely used approach is the so-called Landauer formula [16, 18]. Assume a one-dimensional system with two ideal contact regions connected to a ballistic conductor between them. The contact shall be reflectionless, i.e. electrons from the ballistic conductor are not reflected entering the contact regions [16]. The contact regions are characterized by their chemical potentials μ_l and μ_r, which is equal to the corresponding quasi-Fermi levels for the mentioned assumptions. Hence, the applied bias is given by $V = \mu_\mathrm{l} - \mu_\mathrm{r}$.
The electron states in the ballistic conductor are given by the subbands starting from certain energy levels ε_n. Therefore, the number of transverse modes which contribute to the current for a certain energy $\mathcal{E}$ is given by

$$M(\mathcal{E}) = \sum_n \theta\left(\mathcal{E} - \varepsilon_n\right). \tag{2.49}$$

The current from a single mode can be calculated separately and then summed up to the total current. For a single mode the $+k$ states, i.e. the states with propagation from left to the right, are occupied with electrons due to the left contact according to a certain distribution function $f^+(\mathcal{E})$. The total current through a ballistic conductor of length L resulting from this electrons in positive k states writes as

$$I^+ = \frac{q_0}{L} \sum_k \nu f^+(\mathcal{E}) = \frac{q_0}{L} \sum_k \frac{1}{\hbar} \frac{\partial \mathcal{E}}{\partial k} f^+(\mathcal{E}), \tag{2.50}$$

where ν denotes the group velocity of the electron gas. This sum can be converted to an integral (including spin) over energy:

$$I^+ = \frac{2q_0}{h} \int_\varepsilon^\infty f^+(\mathcal{E}) \mathrm{d}\mathcal{E}, \tag{2.51}$$

where the lower integration boundary is the cut-off energy ε of the transverse mode. Using equation (2.49) this integral can be rewritten to give the current for multiple modes

$$I^+ = \frac{2q_0}{h} \int_{-\infty}^{+\infty} M(\mathcal{E}) f^+(\mathcal{E}) \mathrm{d}\mathcal{E}. \tag{2.52}$$

For a constant number of modes the current reads

$$I = \frac{2q_0}{h} M(\mu_\mathrm{l} - \mu_\mathrm{r}), \tag{2.53}$$

which allows us to calculate the conductivity, i.e. the contact resistance of a ballistic conductor

$$G_{\mathrm{C}} = \frac{2q_0^2}{h} M. \tag{2.54}$$

Assuming a slightly different geometry with two contact regions connected by two ballistic leads to a conductor with transmission probability T the previous results can be applied again. In the low temperature limit the whole current flows in the energy range $\mu_{\mathrm{l}} < \mathcal{E} < \mu_{\mathrm{r}}$ which leads to an inflow of electrons due to the left lead as expressed be equation (2.53)

$$I_{\mathrm{l}}^{+} = \frac{2q_0}{h} M(\mu_{\mathrm{l}} - \mu_{\mathrm{r}}). \tag{2.55}$$

Knowing the transmission probability the outflux of the right lead is given by

$$I_{\mathrm{r}}^{+} = \frac{2q_0}{h} MT(\mu_{\mathrm{l}} - \mu_{\mathrm{r}}), \tag{2.56}$$

and the remaining electrons are reflected back to the left lead

$$I_{\mathrm{l}}^{-} = \frac{2q_0}{h} M(1-T)(\mu_{\mathrm{l}} - \mu_{\mathrm{r}}). \tag{2.57}$$

Therefore, the total current through the device becomes

$$I = I_{\mathrm{l}}^{+} - I_{\mathrm{l}}^{-} = I_{\mathrm{r}}^{+} = \frac{2q_0}{h} MT(\mu_{\mathrm{l}} - \mu_{\mathrm{r}}), \tag{2.58}$$

which gives rise to the conductance

$$G = \frac{2q_0^2}{h} MT. \tag{2.59}$$

This is the conductivity for a two-probe measurement and includes the contact resistance of the leads [14]. The conductivity of the scatterer alone is given by a four-probe measurement and leads to the original Landauer formula

$$G = \frac{2q_0^2}{h} M \frac{T}{1-T} = \frac{2q_0^2}{h} M \frac{T}{R}. \tag{2.60}$$

Büttiker has generalized this formula to the multichannel case [19]. If there are N conducting channels to the left and N' conducting channels to the right the conductivity is given by

$$G = \frac{2q_0^2}{\pi\hbar} \frac{\sum_{i=1}^{N'} T_i}{1 + \left[\sum_{i=1}^{N} (\nu_i^{\mathrm{l}})^{-1} R_i\right] \left[\sum_{i=1}^{N} (\nu_i^{\mathrm{l}})^{-1}\right]^{-1} - \left[\sum_{i=1}^{N'} (\nu_i^{\mathrm{r}})^{-1} T_i\right] \left[\sum_{i=1}^{N'} (\nu_i^{\mathrm{r}})^{-1}\right]^{-1}}. \tag{2.61}$$

Here ν_i^{l} and ν_i^{r} denote the injection velocities on the left and right side respectively.
Since linear-response theories only study small departures from equilibrium state both the Kubo and Landauer formalism are not able to deal with situations far from equilibrium, i.e. when a large voltage drop occurs [15]. Therefore, more advanced methods as described later in Section 2.4 need to be applied.

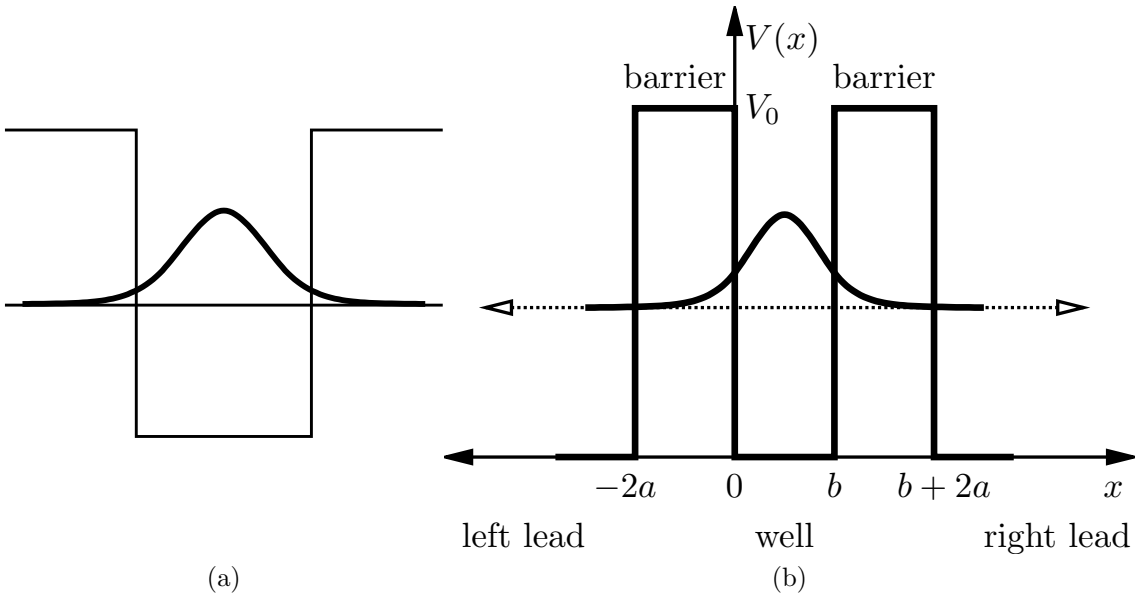

Figure 2.7: (a) A rectangular potential well with a bound state. (b) In a well with barriers of finite thickness a and height V_0 a resonant or quasi-bound state arises.

2.3.3 Resonant Tunneling

In quantum wells with a finite barrier height, quasi bound states (QBS) may occur. The QBS are related to resonances in the transmission of the quantum well. Hence, they are also called resonant states (Fig. 2.7) [11]. The double barrier structures can be treated with the methods that were presented in Section 2.3.1 and applied to a single barrier. The transfer matrix of the barrier is described as before by equations (2.35) and (2.36). Additionally, we have to account for the wave propagation within the well to obtain the full transfer matrix. Since the potential in the well is uniform, just a phase factor depending on the width b and a propagation constant k is introduced [14]. Therefore, the barriers are connected by the transfer matrix

$$\underline{\mathbf{M}}_{\mathrm{W}} = \begin{bmatrix} \mathrm{e}^{-\imath kb} & 0 \\ 0 & \mathrm{e}^{\imath kb} \end{bmatrix}. \tag{2.62}$$

The transfer matrix of the complete double barrier system is given by

$$\underline{\mathbf{M}}_{\mathrm{T}} = \underline{\mathbf{M}}_{\mathrm{L}} \cdot \underline{\mathbf{M}}_{\mathrm{W}} \cdot \underline{\mathbf{M}}_{\mathrm{R}}, \tag{2.63}$$

where $\underline{\mathbf{M}}_{\mathrm{L}}$ and $\underline{\mathbf{M}}_{\mathrm{R}}$ are the transfer matrices of the left and right barrier. As stated in equation (2.39) the transmission coefficient is determined by the coefficient

$$M_{\mathrm{T}11} = M_{\mathrm{L}11} M_{\mathrm{R}11} \mathrm{e}^{-\imath kb} + M_{\mathrm{L}12} M_{\mathrm{R}21} \mathrm{e}^{\imath kb} \tag{2.64}$$

of the transfer matrix.

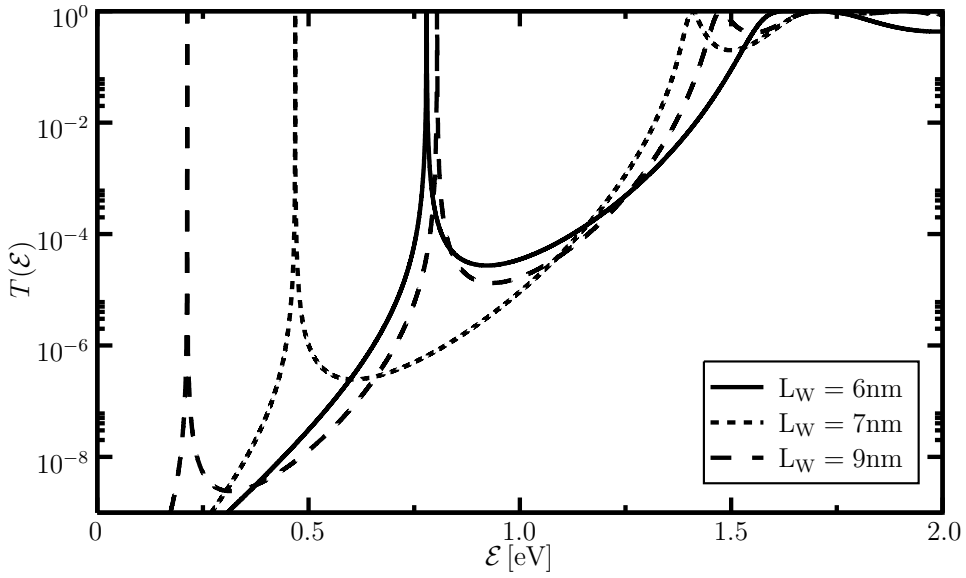

Figure 2.8: Transmission coefficient for a double barrier structure with a height of $V_0 = 1.355$ eV, a barrier width of $L_B = 6$ nm, and three different well widths.

For the geometry in Figure 2.7b with symmetric barriers the propagation constant k is the same in the leads and in the well (cf. equation (2.34a)). Furthermore, for equal barrier width a and height V_0 there is a single attenuation constant γ given by equation (2.34b). Following Ferry [14], the results for a single barrier can be applied to $\underline{\mathbf{M}}_L$ and $\underline{\mathbf{M}}_R$ directly. The matrix element M_{11} of the single barriers can be expressed in polar coordinates

$$M_{11} = m_{11}\mathrm{e}^{\imath\theta}, \tag{2.65}$$

which leads to the magnitude

$$m_{11} = \sqrt{\cosh^2(2\gamma a) + \left(\frac{k^2-\gamma^2}{2k\gamma}\right)^2 \sinh^2(2\gamma a)}, \tag{2.66}$$

and the phase

$$\theta = -\arctan\left[\left(\frac{k^2-\gamma^2}{2k\gamma}\right)\tanh(2\gamma a)\right] + 2ka. \tag{2.67}$$

Therefore, the square of the matrix coefficient (2.64) becomes

$$|M_{T11}|^2 = |m_{11}|^4 + |M_{21}|^4 + 2|m_{11}|^2|M_{21}|^2\cos\big[2(kb-\theta)\big] \tag{2.68}$$

$$= \underbrace{\left(|m_{11}|^2 - |M_{21}|^2\right)^2}_{\det\underline{\mathbf{M}}} + 4|m_{11}|^2|M_{21}|^2\cos^2(kb-\theta). \tag{2.69}$$

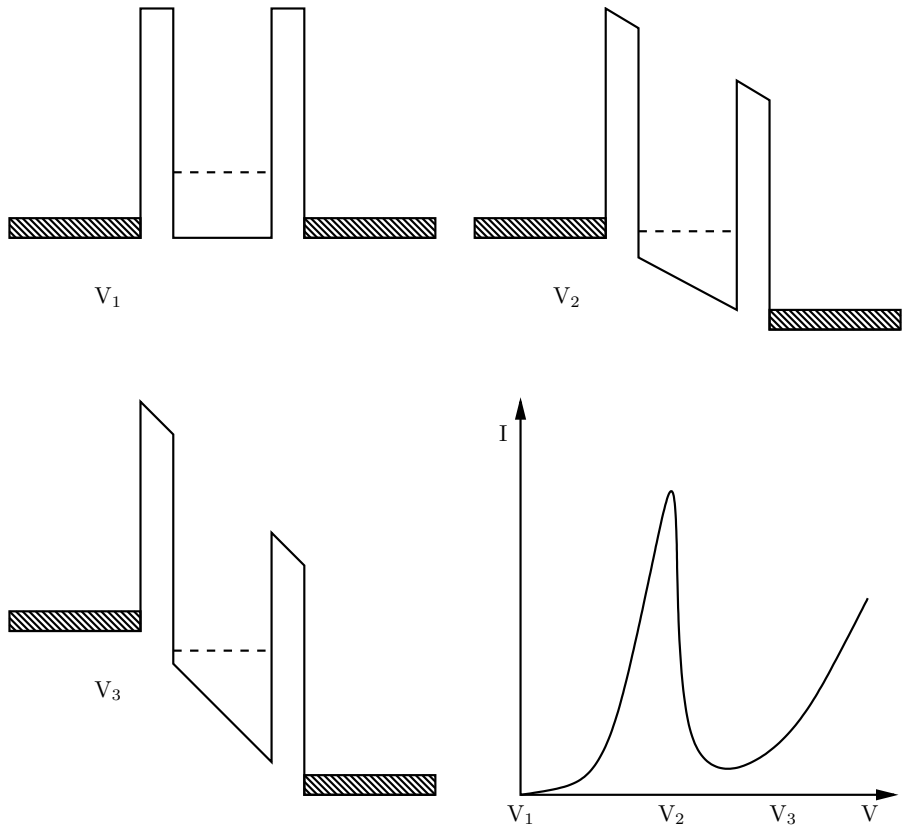

Figure 2.9: Schematic band edge diagram of a resonant tunneling diode and an according I-V characteristic. The hatched areas at the left and right leads symbolize the Fermi sea of electrons. If the bias voltage V_2 is applied, resonance occurs which manifests itself as a peak in the I-V curve.

Since $\det(\underline{\mathbf{M}})$ is unity for a symmetric barrier, the transmission coefficient simplifies further to

$$T(\mathcal{E}) = \frac{1}{|M_{\mathrm{T}11}|^2} = \frac{1}{1 + 4|m_{11}|^2|M_{21}|^2\cos^2(kb-\theta)} = \frac{{T_{\mathrm{B}}}^2}{{T_{\mathrm{B}}}^2 + 4R_{\mathrm{B}}\cos^2(kb-\theta)}. \quad (2.70)$$

The transmission and reflection coefficients T_{B} and R_{B} are given by equations (2.39) and (2.40) derived for the single barrier system.
There are two special cases to consider for the transmission coefficient of a resonant tunneling device. For off-resonance the minimum transmission occurs when the cosine becomes unity, i.e. $kb - \theta = n\pi$

$$T_{\min} = \frac{{T_{\mathrm{B}}}^2}{{T_{\mathrm{B}}}^2 + 4R_{\mathrm{B}}} \sim \frac{{T_{\mathrm{B}}}^2}{4}, \quad (2.71)$$

where the approximation usually holds for typical resonant tunneling devices.

For the second case, the cosine vanishes and the system is in resonance:

$$T_{\max} = 1, \quad \text{for} \quad kb - \theta = (2n+1)\frac{\pi}{2}, \qquad n = 0, 1, \ldots \tag{2.72}$$

If the quasi-bound state within the double barrier device is biased in resonance with the ground state of a lead the transmission becomes unity. This can be clearly seen in Fig. 2.8, where the transmission of a double barrier with a height of $V_0 = 1.355$ eV and a barrier width of $L_B = 3$ nm is plotted for three different well widths.
A schematic band edge diagram of a resonant tunneling device is depicted in Figure 2.9. A quasi-bound state is marked as a dashed line between the two barriers. As the voltage is increased from V_1 to V_2 the current rises up until it reaches its peak at the resonance level (V_2). After the resonance, a region with negative differential resistance occurs and the current drops into a valley after which it starts to grow again (V_3) due to conduction states at higher energies.

2.4 Green's Function Method

In this section, the non-equilibrium Green's functions formalism and its connection to the physical quantities will be presented. First, a basic introduction to the mathematical meaning of Green's functions will be given providing common terminology needed for device simulation. Subsequently, the different types of Green's functions and its application to describe quantum transport phenomena will be discussed.

2.4.1 Introduction to Green's Functions

This section summarizes the introduction of Supriyo Datta [16] which provides the mathematical background. Green's functions provide a tool to solve inhomogeneous differential equation systems. A system with the differential operator D responds with $\underline{\mathbf{R}}$ to an excitation given by $\underline{\mathbf{S}}$,

$$\mathrm{D}\underline{\mathbf{R}} = \underline{\mathbf{S}}. \tag{2.73}$$

A Green's function $G = \mathrm{D}^{-1}$ can be determined, that describes the response by

$$\underline{\mathbf{R}} = \mathrm{D}^{-1}\underline{\mathbf{S}} = G\underline{\mathbf{S}}. \tag{2.74}$$

In an analogous way, one can write

$$(\mathcal{E} - \mathrm{H})\,\psi = \underline{\mathbf{S}}, \tag{2.75}$$

where ψ is the wavefunction, $\underline{\mathbf{S}}$ is an excitation due to a wave incident from a lead and H is the Hamiltonian. Like equation (2.73), the response for this system can be expressed via a Green's function,

$$G = (\mathcal{E} - \mathrm{H})^{-1}. \tag{2.76}$$

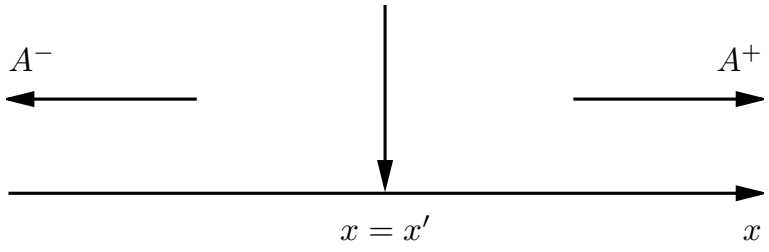

Figure 2.10: Excitation leading to the retarded Green's function

To fully determine the inverse of this differential operator it is necessary to define proper boundary conditions. For a one-dimensional wire with the constant potential energy V_0, the Hamiltonian writes

$$\mathrm{H} = -\frac{\hbar^2}{2m}\frac{\partial^2}{\partial x^2} + V_0. \tag{2.77}$$

Hence, the Green's function of the system is given by

$$G = \left(\mathcal{E} - V_0 + \frac{\hbar^2}{2m}\frac{\partial^2}{\partial x^2}\right)^{-1}, \tag{2.78}$$

which can be rewritten as

$$\left(\mathcal{E} - V_0 + \frac{\hbar^2}{2m}\frac{\partial^2}{\partial x^2}\right) G(x, x') = \delta(x - x'). \tag{2.79}$$

The similarities with the Schrödinger equation (2.4) can be clearly seen

$$\left(\mathcal{E} - V_0 + \frac{\hbar^2}{2m}\frac{\partial^2}{\partial x^2}\right) \psi(x) = 0. \tag{2.80}$$

The difference lies in the source term $\delta(x - x')$ whereby the Green's function $G(x, x')$ describes the propagation of a disturbance at x' to x. Such an excitation causes two waves originating from x' (Fig. 2.10). These wavefunctions with the amplitudes A^+ and A^- are given by

$$G(x, x') = A^+ \exp\big[\imath k\,(x - x')\big], \qquad \text{if } x > x' \tag{2.81a}$$
$$G(x, x') = A^- \exp\big[-\imath k\,(x - x')\big], \qquad \text{if } x < x' \tag{2.81b}$$

with the wave vector $k = \sqrt{2m(E - V_0)}/\hbar$. This is a solution for every point $x \neq x'$ but in order to fulfill equation (2.79) at $x = x'$ additional boundary conditions have to be specified. The Green's function and its derivative need to satisfy:

$$I) \qquad G(x, x')\Big|_{x=x'^+} - G(x, x')\Big|_{x=x'^-} = 0 \tag{2.82a}$$
$$II) \qquad \frac{\partial G(x, x')}{\partial x}\Big|_{x=x'^+} - \frac{\partial G(x, x')}{\partial x}\Big|_{x=x'^-} = \frac{2m}{\hbar^2}. \tag{2.82b}$$

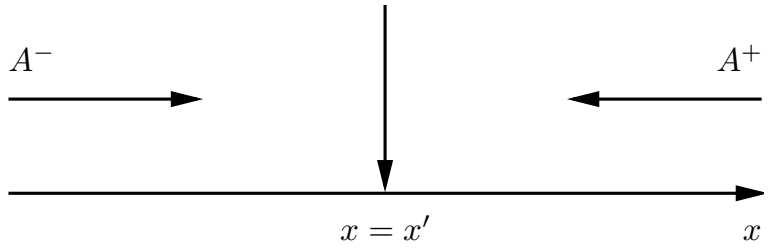

Figure 2.11: Excitation leading to the advanced Green's function

Thereby, the amplitudes of the wave functions are uniquely determined

$$A = A^+ = A^- = -\frac{\imath m}{\hbar^2 k} = -\frac{\imath}{\hbar\nu}, \tag{2.83}$$

with $\nu = (\hbar k)/m$ which leads to the Green's function of an infinite one-dimensional wire

$$G(x, x') = -\frac{\imath}{\hbar\nu} \exp\big[\imath k\,|x - x'|\big]. \tag{2.84}$$

However, equation (2.84) is only one of two possible solutions, which is called the retarded Green's function $G^{\mathrm{R}}(x, x')$. The other solution, called advanced Green's function, consists of incoming waves vanishing at the point of excitation $x = x'$ instead of outgoing waves which originate from it (cf. Fig. 2.11). Hence, two different sets of boundary conditions determine the advanced and retarded Green's function

$$G^{\mathrm{R}}(x, x') = -\frac{\imath}{\hbar\nu} \exp\big[\imath k\,|x - x'|\big], \tag{2.85a}$$

$$G^{\mathrm{A}}(x, x') = +\frac{\imath}{\hbar\nu} \exp\big[-\imath k\,|x - x'|\big]. \tag{2.85b}$$

Here

$$k = \sqrt{2m(E - V_0)}/\hbar \qquad \text{and} \qquad \nu = (\hbar k)/m \tag{2.86}$$

is the wave vector and the particle velocity, respectively.
Another way to account for the boundary conditions is to introduce an infinitesimal imaginary part to the energy. Equation (2.79) then becomes the constituting relation for $G^{\mathrm{R}}(x, x')$. Introducing $\eta > 0$,

$$\left(\mathcal{E} - V_0 + \frac{\hbar^2}{2m}\frac{\partial^2}{\partial x^2} + \imath\eta\right) G^{\mathrm{R}}(x, x') = \delta(x - x'). \tag{2.87}$$

This gives a positive imaginary part in the wavevector k, which furthermore renders the advanced Green's function exponentially growing at the boundary and therefore unphysical. Likewise, with $\eta > 0$ the advanced Green's function is the only acceptable solution of

$$\left(\mathcal{E} - V_0 + \frac{\hbar^2}{2m}\frac{\partial^2}{\partial x^2} - \imath\eta\right) G^{\mathrm{A}}(x, x') = \delta(x - x'). \tag{2.88}$$

This leads to the commonly used definitions of the retarded and advanced Green's functions as

$$G^{\mathrm{R}} = (\mathcal{E} - \mathrm{H} + \imath\eta)^{-1}, \qquad \eta \longrightarrow 0^{+} \tag{2.89a}$$

$$G^{\mathrm{A}} = (\mathcal{E} - \mathrm{H} - \imath\eta)^{-1}, \qquad \eta \longrightarrow 0^{+}. \tag{2.89b}$$

2.4.2 Equilibrium Green's Functions

In this section, the relation of the Green's functions used within this thesis and its origin will be provided. The work on non-equilibrium Green's functions has been pioneered by Martin and Schwinger [20], who provided the base for the work of Kadanoff and Baym [7] and Keldysh [8]. Following Haug [21] the time-ordered single-particle Green's function writes as

$$G\left(\mathbf{x},\mathbf{x}';t,t'\right) = -\frac{\imath}{\hbar}\frac{\langle\Psi_0|T\big(\psi_{\mathrm{H}}(\mathbf{x},t)\psi^{\dagger}_{\mathrm{H}}(\mathbf{x}',t')\big)|\Psi_0\rangle}{\langle\Psi_0|\Psi_0\rangle}, \tag{2.90}$$

where the ground state of the interacting system is given by $\mathrm{H}|\Psi_0\rangle = \mathcal{E}_0|\Psi_0\rangle$ and $T\big(\mathrm{A}(t)\mathrm{B}(t')\big)$ is the time-ordering operator, that moves the operator with the earlier time-argument to the right

$$T\big(\mathrm{A}(t)\mathrm{B}(t')\big) = \theta(t-t')\mathrm{A}(t)\mathrm{B}(t') - \theta(t'-t)\mathrm{A}(t)\mathrm{B}(t'). \tag{2.91}$$

The operators $\psi_{\mathrm{H}}(\mathbf{x},t)$ are in the Heisenberg picture which means that they are time-dependent. Calculating the time derivative of the Green's function gives

$$\begin{aligned}
\imath\hbar\frac{\partial G\left(\mathbf{x},\mathbf{x}';t,t'\right)}{\partial t} &= \delta(t-t')\frac{\langle\Psi_0|\big\{\psi_{\mathrm{H}}(\mathbf{x},t),\psi^{\dagger}_{\mathrm{H}}(\mathbf{x}',t')\big\}|\Psi_0\rangle}{\langle\Psi_0|\Psi_0\rangle} \\
&\quad - \frac{\imath}{\hbar}\frac{\langle\Psi_0|T\big(\imath\hbar\frac{\partial\psi_{\mathrm{H}}(\mathbf{x},t)}{\partial t}\psi^{\dagger}_{\mathrm{H}}(\mathbf{x}',t')\big)|\Psi_0\rangle}{\langle\Psi_0|\Psi_0\rangle} \\
&= \delta(t-t')\delta(\mathbf{x}-\mathbf{x}') - \frac{\imath}{\hbar}\frac{\langle\Psi_0|T\big(\imath\hbar\frac{\partial\psi_{\mathrm{H}}(\mathbf{x},t)}{\partial t}\psi^{\dagger}_{\mathrm{H}}(\mathbf{x}',t')\big)|\Psi_0\rangle}{\langle\Psi_0|\Psi_0\rangle}
\end{aligned} \tag{2.92}$$

where $\{\mathrm{A},\mathrm{B}\}$ denotes an anti-commutator. Equation (2.92) is of the same form as equation (2.74) with the delta functions providing the excitation to the system. Therefore, the time-ordered Green's function defined in (2.90) obeys an inhomogeneous differential equation.
For example, consider free particles with the Hamiltonian $\mathrm{H} = -\frac{\hbar^2}{2m}\int dx\psi^{\dagger}(x)\nabla^2\psi(x)$ following the Heisenberg equation of motion [21]

$$\imath\hbar\frac{\partial\psi_{\mathrm{H}}(x,t)}{\partial t} = \big[\psi_{\mathrm{H}}(x,t),\mathrm{H}\big] = -\frac{\hbar^2\nabla^2_x}{2m}\psi_{\mathrm{H}}(x,t), \tag{2.93}$$

with the square brackets $\big[\cdot,\cdot\big]$ denoting the commutator relation. Therefore, the differential equation of the free particle Green's function turns into the inhomogeneous

Schrödinger equation

$$\Big(\imath\hbar\frac{\partial}{\partial t}+\frac{\hbar^2\nabla_x^2}{2m}\Big)G(x,x';t,t')=\hbar\delta(t-t')\delta(x-x'). \tag{2.94}$$

Additionally to the time-ordered Green's function the retarded and advanced Green's functions as well as the lesser and greater Green's functions are defined as

$$G^{\mathrm{R}}(\mathbf{x},\mathbf{x}';t,t')=-\frac{\imath}{\hbar}\theta(t-t')\langle\{\psi(\mathbf{x},t),\psi^\dagger(\mathbf{x}',t')\}\rangle \tag{2.95a}$$

$$G^{\mathrm{A}}(\mathbf{x},\mathbf{x}';t,t')=\frac{\imath}{\hbar}\theta(t'-t)\langle\{\psi(\mathbf{x},t),\psi^\dagger(\mathbf{x}',t')\}\rangle \tag{2.95b}$$

$$G^{<}(\mathbf{x},\mathbf{x}';t,t')=\frac{\imath}{\hbar}\langle\psi^\dagger(\mathbf{x}',t')\psi(\mathbf{x},t)\rangle \tag{2.95c}$$

$$G^{>}(\mathbf{x},\mathbf{x}';t,t')=-\frac{\imath}{\hbar}\langle\psi(\mathbf{x},t)\psi^\dagger(\mathbf{x}',t')\rangle \tag{2.95d}$$

where the angle brackets $\langle\cdots\rangle$ denote the calculation of the expectation value. The normalization factor $\langle\Psi_0|\Psi_0\rangle$ has been omitted here [21].
The retarded Green's function G^{R} gives the response at time t to a perturbation of the system at an earlier time t'. The lesser Green's function $G^{<}$ is also called particle propagator or correlation function, whereas the greater Green's function is called hole propagator [21]. The differences between the four Green's functions become important when treating non-equilibrium systems, which will be done in the succeeding section.
The Green's functions are related to each other by

$$G^{\mathrm{R}}-G^{\mathrm{A}}=G^{>}-G^{<}, \tag{2.96}$$

and the time-ordered as well as the retarded and advanced Green's functions can be expressed in terms of the lesser and greater Green's functions

$$G(\mathbf{x},\mathbf{x}';t,t')=\theta(t-t')G^{>}(\mathbf{x};t)+\theta(t'-t')G^{<}(\mathbf{x},\mathbf{x}';t,t'), \tag{2.97a}$$

$$G^{\mathrm{R,A}}(\mathbf{x},\mathbf{x}';t,t')=\pm\theta(\pm t\mp t')\big[G^{>}(\mathbf{x},\mathbf{x}';t,t')-G^{<}(\mathbf{x},\mathbf{x}';t,t')\big]. \tag{2.97b}$$

Every Green's functions has its domain, where it is best applied. The time-ordered Green's functions are used for perturbation theory. The retarded and advanced Green's functions allow to treat physical responses and therefore provide information on spectral properties, density of states and scattering rates. The lesser and greater Green's functions describe kinetic properties and allow to obtain physical quantities, i.e. quantum mechanical observables [21]. As an example, the particle density is given by

$$\langle\varsigma(\mathbf{x})\rangle=-\imath G^{<}(\mathbf{x},\mathbf{x},t,t) \tag{2.98}$$

in terms of the lesser Green's function.

2.4.3 Non-Equilibrium Green's Functions

In the following paragraphs the Green's functions defined in (2.95) will be applied to a system under nonequilibrium conditions [16]. Since we are interested in steady-state problems, we make use of the fact, that under this prerequisite the correlation functions only depend on time differences. This can be used to Fourier transform the two-times correlation function (2.95), which gives

$$G^{<}(\mathbf{x},\mathbf{x}';\mathcal{E}) = \int_{-\infty}^{\infty} \frac{1}{\hbar} G^{<}(\mathbf{x},\mathbf{x}';\tau)\, \mathrm{e}^{-\imath\mathcal{E}\tau/\hbar}\mathrm{d}\tau, \qquad \tau = t - t', \tag{2.99}$$

where the energy dependence of the treated particle is revealed.
An important quantity is the so-called density matrix $\rho(\mathbf{x},\mathbf{x}',t)$, which is derived from the two-times correlation function by setting $t = t'$,

$$\rho(\mathbf{x},\mathbf{x}',t) = -\imath G^{<}(\mathbf{x},\mathbf{x}';t,t')\Big|_{t=t'}. \tag{2.100}$$

This is equal to an integration over energy which yields

$$\rho(\mathbf{x},\mathbf{x}',t) = -\imath G^{<}(\mathbf{x},\mathbf{x}';t,t')\Big|_{t=t'} = -\imath \int_{-\infty}^{\infty} G^{<}(\mathbf{x},\mathbf{x}';\mathcal{E})\,\frac{\mathrm{d}\mathcal{E}}{2\pi}. \tag{2.101}$$

Therefore, the electron density (2.98) is given by the diagonal elements of the density matrix:

$$n(\mathbf{x}) = -2\imath \int_{-\infty}^{\infty} G^{<}(\mathbf{x},\mathbf{x};\mathcal{E})\,\frac{\mathrm{d}\mathcal{E}}{2\pi}. \tag{2.102}$$

The factor of two accounts for spin degeneracy.
The lesser and greater Green's function describe the propagation of a particle within a state. To cover the transitions from one state to another the self-energies $\Sigma^{<}(\mathbf{x},\mathbf{x}';t,t')$ and $\Sigma^{>}(\mathbf{x},\mathbf{x}';t,t')$ are introduced. In steady state, a Fourier transformation similar to the procedure for the lesser Green's function gives $\Sigma^{<}(\mathbf{x},\mathbf{x}';\mathcal{E})$ and $\Sigma^{>}(\mathbf{x},\mathbf{x}';\mathcal{E})$. The self-energies allow to describe scattering events and are used to incorporate the effects of leads on a device as described in Section 3.2.
To achieve a more compact notation, the product of two terms is interpreted as a matrix product in the internal variables [21]. The four types of Green's functions and the self energies are related by the kinetic equations

$$G^{<} = G^{\mathrm{R}}\Sigma^{<}G^{\mathrm{A}}, \tag{2.103a}$$

$$G^{>} = G^{\mathrm{R}}\Sigma^{>}G^{\mathrm{A}}. \tag{2.103b}$$

Contrary to the equilibrium case, these have to be solved simultaneously with the equations for the Green's functions [16] given by

$$G^{\mathrm{R}} = \left[\mathcal{E}\underline{\mathbf{I}} - \mathrm{H} - \Sigma^{\mathrm{R}}\right]^{-1}, \tag{2.104a}$$

$$G^{\mathrm{A}} = \left[G^{\mathrm{R}}\right]^{\dagger}. \tag{2.104b}$$

Equation (2.104a) is for the sake of completeness equivalently rewritten in real space representation:

$$\left[\mathcal{E} - \mathrm{H}\right] G^{\mathrm{R}}\left(\mathbf{x}, \mathbf{x}'; \mathcal{E}\right) - \int \Sigma^{\mathrm{R}}\left(\mathbf{x}, \mathbf{x}''; \mathcal{E}\right) G^{\mathrm{R}}\left(\mathbf{x}'', \mathbf{x}'; \mathcal{E}\right) \mathrm{d}\mathbf{x}'' = \delta\left(\mathbf{x} - \mathbf{x}'\right). \tag{2.105}$$

To solve equations (2.103) and (2.104), the knowledge of the retarded self-energy Σ^{R} and the lesser and greater self-energies $\Sigma^{<}$ and $\Sigma^{>}$ is necessary. The self-energies to incorporate the leads are derived in Section 3.2. The modeling of scattering requires great care. The modeling of electron-phonon interactions and the resulting self-energies will be given in the following Section 2.4.4. More details on self-energies have been given by Mahan [22].
A further important quantity, the current density (2.31), can be expressed in terms of the non-equilibrium Green's functions [16]

$$\mathbf{j}(\mathbf{x}, \mathcal{E}) = -\frac{\imath\hbar q_0}{2m_0}\left[(\nabla - \nabla')\psi(\mathbf{x})\psi^*(\mathbf{x}')\right]\Big|_{\mathbf{x}'=\mathbf{x}}. \tag{2.106}$$

Here, the gradient operators ∇ and ∇' act on $\mathbf{x}$ and $\mathbf{x}'$, respectively. The definition of the lesser Green's function is used to substitute $\psi(\mathbf{x})\psi^*(\mathbf{x}')$. Furthermore, considering the steady-state condition gives a factor of 2π. Hence, we derive the current density at the energy $\mathcal{E}$ as

$$\mathbf{j}(\mathbf{x}, \mathcal{E}) = -\frac{\hbar q_0}{2m_0}\frac{1}{2\pi}\left[(\nabla - \nabla')G^{<}\left(\mathbf{x}, \mathbf{x}'; \mathcal{E}\right)\right]\Big|_{\mathbf{x}'=\mathbf{x}}. \tag{2.107}$$

Finally, integration over energy and taking the electron spin into account gives the overall current density

$$\mathbf{j}(\mathbf{x}) = -2\frac{\hbar q_0}{2m_0}\int_{-\infty}^{\infty}\left[(\nabla - \nabla')G^{<}\left(\mathbf{x}, \mathbf{x}'; \mathcal{E}\right)\right]\Big|_{\mathbf{x}'=\mathbf{x}}\frac{\mathrm{d}\mathcal{E}}{2\pi}. \tag{2.108}$$

2.4.4 Scattering

The self-energies depend on the type of phase breaking interaction that is modeled. They can be obtained by applying perturbation theory. As a result, the form of the self-energies depends on the order of the perturbation. As an example, the incorporation of electron-phonon interaction in the self-consistent Born approximation will be given according to [16]. More sophisticated modeling approaches to other scattering processes

can be found in [22].
The lesser and greater self-energies for the electron-phonon interaction read

$$\Sigma^{<}_{\text{e-ph}}(\mathbf{x},\mathbf{x}';\mathcal{E}) = \int D(\mathbf{x},\mathbf{x}';\hbar\omega)\, G^{<}(\mathbf{x},\mathbf{x}';\mathcal{E}-\hbar\omega)\,\mathrm{d}(\hbar\omega), \tag{2.109a}$$

$$\Sigma^{>}_{\text{e-ph}}(\mathbf{x},\mathbf{x}';\mathcal{E}) = \int D(\mathbf{x},\mathbf{x}';\hbar\omega)\, G^{>}(\mathbf{x},\mathbf{x}';\mathcal{E}+\hbar\omega)\,\mathrm{d}(\hbar\omega). \tag{2.109b}$$

Hence, $D(\mathbf{x},\mathbf{x}';\hbar\omega)$ describes the spatial correlation and energy spectrum of the phase-breaking scatterers [16]. Absorption occurs if $\hbar\omega > 0$ and emission occurs in the opposite case. Given the number of phonons $N_{\mathbf{q}}$ with the wavevector $\mathbf{q}$ and frequency $\omega_{\mathbf{q}}$ where a single phonon exerts a potential $V_{\mathbf{q}}$ on an electron, we get

$$\begin{aligned} D(\mathbf{x},\mathbf{x}';\hbar\omega) = \sum_{\mathbf{q}} |V_{\mathbf{q}}|^2 \Big\{ &\exp\big[-\imath\mathbf{q}\cdot(\mathbf{x}-\mathbf{x}')\big] N_{\mathbf{q}}\,\delta(\omega-\omega_{\mathbf{q}}) \\ &+ \exp\big[+\imath\mathbf{q}\cdot(\mathbf{x}-\mathbf{x}')\big]\,(N_{\mathbf{q}}+1)\,\delta(\omega+\omega_{\mathbf{q}})\Big\}. \end{aligned} \tag{2.110}$$

Assuming thermal equilibrium, the number of phonons is given by the Bose-Einstein distribution

$$N_{\mathbf{q}} = \frac{1}{\exp\left(\dfrac{\hbar\omega_{\mathbf{q}}}{k_{\mathrm{B}}T}\right)-1}. \tag{2.111}$$

The retarded self-energy is given by

$$\Sigma^{\mathrm{R}}_{\text{e-ph}}(\mathbf{x},\mathbf{x}';\mathcal{E}) = \Gamma^{\mathrm{H}}_{\text{e-ph}}(\mathbf{x},\mathbf{x}';\mathcal{E}) + \frac{\imath}{2}\Gamma_{\text{e-ph}}(\mathbf{x},\mathbf{x}';\mathcal{E}), \tag{2.112}$$

where

$$\Gamma^{\mathrm{H}}_{\text{e-ph}}(\mathbf{x},\mathbf{x}';\mathcal{E}) = \mathfrak{P}\int \frac{\Gamma_{\text{e-ph}}(\mathbf{x},\mathbf{x}';\mathcal{E}')}{\mathcal{E}-\mathcal{E}'}\mathrm{d}\mathcal{E}'. \tag{2.113}$$

In (2.113) $\mathfrak{P}$ denotes the principal part which yields the Hilbert transform of the broadening $\Gamma_{\text{e-ph}}$. The broadening depends on the lesser and greater self-energies via the relation

$$\Gamma_{\text{e-ph}}(\mathbf{x},\mathbf{x}';\mathcal{E}) = \imath\big(\Sigma^{>}_{\text{e-ph}}(\mathbf{x},\mathbf{x}';\mathcal{E}) - \Sigma^{<}_{\text{e-ph}}(\mathbf{x},\mathbf{x}';\mathcal{E})\big). \tag{2.114}$$

Therefore, the retarded self-energy in the defining equation $G^{\mathrm{R}} = \big[\mathcal{E}\underline{\mathbf{I}} - \mathrm{H} - \Sigma^{\mathrm{R}}\big]^{-1}$ for the retarded Green's function itself is connected to the lesser and greater self-energies in the lesser Green's function $G^{<} = G^{\mathrm{R}}\Sigma^{<}G^{\mathrm{A}}$ and greater Green's function $G^{>} = G^{\mathrm{R}}\Sigma^{>}G^{\mathrm{A}}$. This couples the retarded and advanced Green's functions to the lesser and greater Green's functions. Hence, a computationally very demanding self-consistent calculation of the self-energies (2.109), (2.112) and Green's functions (2.103) and (2.104) is required.

A little inaccuracy sometimes saves a ton of explanation.

H. H. Munro

CHAPTER 3

Numerical Methods

For nanoscaled devices, numerical simulation based on the non equilibrium Green's functions (NEGF) formalism has been successfully applied by several groups [9,23–25]. After depicting a method to solve for the Schrödinger equation, the numerical implementation of the non-equilibrium Green's functions formalism introduced in the previous section is described. A very efficient implementation of this method has been achieved by means of a recursive algorithm [10].
Proper integration methods are vital for the stability and accuracy of NEGF simulations. This chapter is concluded with an overview of numerical integration methods, that were adopted for the NEGF solver.

3.1 Numerical Solution of Schrödinger Equation

In this section, numerical methods based on spatial discretization to directly solve for the Schrödinger equation will be presented. The closed and the open quantum system will be discussed separately but their mathematical similarities will be pointed out.

3.1.1 Closed Boundaries

The time-independent Schrödinger equation can be solved numerically by applying a finite difference scheme. For the one-dimensional time-independent Schrödinger equation

$$\left(-\frac{\hbar^2}{2}\frac{\partial}{\partial x}\frac{1}{m_x(x)}\frac{\partial}{\partial x}+V(x)\right)\psi(x)=\mathcal{E}\psi(x), \tag{3.1}$$

where the position-dependent inverse effective mass $1/m_x(x)$ is evaluated from the effective mass tensor. For a discretization, the first and second derivative of the wave function have to be determined. For a uniform grid (Fig. 3.1) $x_j = j\Delta x$ and the values

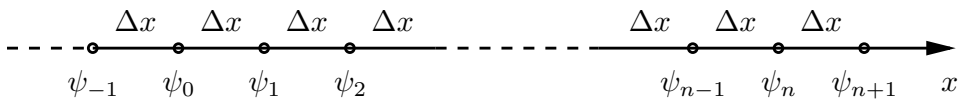

Figure 3.1: Discretization points on an equidistant one-dimensional grid

of the wavefunction are given as $\psi_j = \psi(x_j)$. The application of central finite differences gives

$$\frac{\partial}{\partial x}\psi(x_j) = \frac{\psi_{j+1} - \psi_{j-1}}{2\Delta x} + O(\Delta x^2), \tag{3.2}$$

for the first and

$$\frac{\partial^2}{\partial x^2}\psi(x_j) = \frac{\psi_{j+1} - 2\psi_j + \psi_{j-1}}{\Delta x^2} + O(\Delta x^2), \tag{3.3}$$

for the second derivative of the wavefunction ψ with a remaining second order error $O(\Delta x^2)$ due to the Taylor series expansion. This leads [15] to a set of equations of the form

$$\mathrm{H}\psi_j = -s_j\psi_{j-1} + d_j\psi_j - s_{j+1}\psi_{j+1} = \mathcal{E}\psi_j, \tag{3.4}$$

which allows one to write the Hamiltonian as a tridiagonal matrix. The equation system reads

$$\underbrace{\begin{bmatrix} d_1 - \mathcal{E} & -s_2 & & & & \\ -s_2 & d_2 - \mathcal{E} & -s_3 & & & \\ & -s_3 & d_3 - \mathcal{E} & -s_4 & & \\ & & \ddots & \ddots & \ddots & \\ & & & -s_{n-1} & d_{n-1} - \mathcal{E} & -s_n \\ & & & & -s_n & d_n - \mathcal{E} \end{bmatrix}}_{\mathrm{H}} \begin{bmatrix} \psi_1 \\ \psi_2 \\ \psi_3 \\ \vdots \\ \psi_{n-1} \\ \psi_n \end{bmatrix} = \mathbf{0}. \tag{3.5}$$

The coefficients of the Hamiltonian matrix d and s take account for variations in the effective mass like heterojunctions correctly. Is is required, that the wavefunction $\psi(x)$ and $\frac{1}{m_x(x)}\frac{\partial}{\partial x}\psi(x)$ are continuous to ensure conservation of current. A piece-wise linear wave function between adjacent mesh points is eligible and yields the following discretization [15]

$$d_j = \frac{\hbar^2}{2\Delta x^2}\left(\frac{1}{m_{j-1} + m_j} + \frac{1}{m_j + m_{j+1}}\right) + V_j, \tag{3.6a}$$

$$s_j = \frac{\hbar^2}{2\Delta x^2}\frac{1}{m_{j-1} + m_j}. \tag{3.6b}$$

Here, V_j is the potential and m_j is the effective mass at grid point x_j. This results in an eigenvalue problem that can be solved fast and accurately with standard numerical methods.

3.1.2 Open Boundaries

The methods described in the previous section have to be expanded for the application to open quantum systems connected to leads. The approach by Lent and Kirkner [26], the so-called the quantum transmitting boundary method (QTBM) will be presented as proposed by Frensley [15]. The quantum transmitting boundary conditions are determined by a linear combination of the values of the wavefunction ψ on two neighboring grid points. Therefore, the system defined by (3.5) with the endpoints $j = 1$ and $j = n$ will be extended by an additional boundary point at each side. The wavefunctions take the form

$$\psi_j = a_1 \mathrm{e}^{(j-1)\imath k_1 \Delta x} + b_1 \mathrm{e}^{(1-j)\imath k_1 \Delta x} \qquad \text{for } j \leq 1, \tag{3.7a}$$

$$\psi_j = a_n \mathrm{e}^{(n-j)\imath k_n \Delta x} + b_n \mathrm{e}^{(j-n)\imath k_n \Delta x} \qquad \text{for } j \geq n, \tag{3.7b}$$

where k_1 and k_n are the wave vectors. They may be found by solving the Schrödinger equation at the boundaries, which leads to the dispersion relation

$$\mathcal{E} = d_1 - s_1 \left(\mathrm{e}^{\imath k_1 \Delta x} + \mathrm{e}^{-\imath k_1 \Delta x} \right), \tag{3.8a}$$

$$\mathcal{E} = d_n - s_n \left(\mathrm{e}^{\imath k_n \Delta x} + \mathrm{e}^{-\imath k_n \Delta x} \right). \tag{3.8b}$$

The wavefunctions at the boundary of the simulation domain are given by

$$\psi_1 = a_1 + b_1, \tag{3.9a}$$

$$\psi_n = a_n + b_n. \tag{3.9b}$$

They are connected to the nearby wavefunctions

$$\psi_0 = a_1 \mathrm{e}^{-\imath k_1 \Delta x} + b_1 \mathrm{e}^{\imath k_1 \Delta x}, \tag{3.10a}$$

$$\psi_{n+1} = a_n \mathrm{e}^{-\imath k_n \Delta x} + b_n \mathrm{e}^{\imath k_n \Delta x}. \tag{3.10b}$$

The two unknowns b_1 and b_n are eliminated using equations (3.9) and (3.10) which leaves a_1 and a_n to be determined by

$$a_1 = \frac{\psi_0 - \mathrm{e}^{\imath k_1 \Delta x} \psi_1}{e^{-\imath k_1 \Delta x} + \mathrm{e}^{\imath k_1 \Delta x}} = \alpha_1 \psi_0 + \beta_1 \psi_1, \tag{3.11a}$$

$$a_n = \frac{\psi_{n+1} - \mathrm{e}^{\imath k_n \Delta x} \psi_n}{e^{-\imath k_n \Delta x} + \mathrm{e}^{\imath k_n \Delta x}} = \alpha_n \psi_{n+1} + \beta_n \psi_n. \tag{3.11b}$$

This eventually results in a $(n+2)$-dimensional equation system

$$\begin{bmatrix} \alpha_1 & \beta_1 & & & & & \\ -s_1 & d_1 - \mathcal{E} & -s_2 & & & & \\ & -s_2 & d_2 - \mathcal{E} & -s_3 & & & \\ & & \ddots & \ddots & \ddots & & \\ & & & -s_n & d_n - \mathcal{E} & -s_{n+1} & \\ & & & & \beta_n & \alpha_n & \end{bmatrix} \begin{bmatrix} \psi_0 \\ \psi_1 \\ \psi_2 \\ \vdots \\ \psi_n \\ \psi_{n+1} \end{bmatrix} = \begin{bmatrix} a_1 \\ 0 \\ 0 \\ \vdots \\ 0 \\ a_n \end{bmatrix}. \tag{3.12}$$

By setting $a_1 = 1$ and $a_n = 0$, the wave function for a left-incident wave is obtained by solving the system for ψ_j. For the numerical solution of the open quantum system it is to be mentioned that (3.12) represents a complex non-Hermitian matrix contrary to (3.5) of a closed system which results in a Hermitian Hamiltonian matrix. But since it is tridiagonal, fast numerical methods may be applied advantageously.
The QTBM is closely related to the non-equilibrium Green's functions formalism, which is discussed in further detail in Section 3.2.4.

3.2 Numerical Solution of NEGF

Various numerical techniques have been proposed to implement the non-equilibrium Green's functions formalism. In the following, derivations of a discretized representation of the Green's functions are given. A numerical solution procedure using matrix operations, as well as highly efficient use of a recursive algorithm are described.

3.2.1 Hamiltonian

When dealing with one-dimensional devices it is convenient to split the Hamiltonian into a longitudinal and a transversal part [27]. Therefore, the procedure presented in Section 2.2 may be applied. The effective mass Hamiltonian (2.11) yields the longitudinal Hamiltonian in transport direction

$$\mathrm{H} = -\frac{\hbar^2}{2}\frac{\partial}{\partial z}\frac{1}{m_z(z)}\frac{\partial}{\partial z} + V(z) \tag{3.13}$$

A discretization of this Hamiltonian can be determined with the central differences scheme (cf. Section 3.1.1). Using a one-dimensional infinite simulation domain the discretized Hamiltonian is an infinite-dimensional matrix of the form [16]

$$\mathrm{H} = \begin{bmatrix} \ddots & -t_{i-2,i-1} & 0 & 0 & 0 \\ -t_{i-1,i-2} & V_{i-1} + 2t_{i-1,i-1} & -t_{i-1,i} & 0 & 0 \\ 0 & -t_{i,i-1} & V_i + 2t_{i,i} & -t_{i,i+1} & 0 \\ 0 & 0 & -t_{i+1,i} & V_{i+1} + 2t_{i+1,i+1} & -t_{i+1,i+2} \\ 0 & 0 & 0 & -t_{i+2,i+1} & \ddots \end{bmatrix} \tag{3.14}$$

where V_i is the potential at grid point i. The coefficients $t_{i,j}$ for a uniform grid with spacing a are given by [23]

$$t_{i,i} = \frac{\hbar^2}{2a^2}\left(\frac{1}{m^+} + \frac{1}{m^-}\right) + V_j, \tag{3.15a}$$

$$t_{i,i\pm1} = \frac{\hbar^2}{2a^2}\frac{1}{m_{j\pm1} + m_j}. \tag{3.15b}$$

For a non-uniform grid one has to ensure hermiticity of the Hamiltonian $t_{i,i+1} = t^{\dagger}_{i+1,i}$ [28].

3.2.2 Discretization of Green's Functions

After obtaining the Hamiltonian, the retarded Green's function (see Section 2.4) can be calculated by the matrix inversion

$$G^{\mathrm{R}} = [(\mathcal{E} + \imath\eta)\underline{\mathbf{I}} - \mathrm{H}]^{-1}\,, \tag{3.16}$$

where $\eta \to 0^+$ has to be considered in the correct limit. This matrix is infinite dimensional and so it has to be truncated correctly to reflect open boundary conditions [16]. By partitioning the matrix into a device region and a contact region one obtains the matrix equation:

$$\begin{bmatrix} G^{\mathrm{R}} & G_{\mathrm{DC}} \\ G_{\mathrm{CD}} & G_{\mathrm{C}} \end{bmatrix} = \begin{bmatrix} \mathcal{E}\underline{\mathbf{I}} - \mathrm{H} & -\tau \\ -\tau^\dagger & (\mathcal{E} + \imath\eta)\underline{\mathbf{I}} - \mathrm{H_C} \end{bmatrix}^{-1}. \tag{3.17}$$

The unknown retarded Green's function G^{R} of the device needs to be determined. It does not include the infinitesimal imaginary part $\imath\eta$ because this term is introduced via the coupling to the contact region as shown by [16, page 146]. Hence, the retarded Green's function writes as

$$G^{\mathrm{R}} = [\mathcal{E}\underline{\mathbf{I}} - \mathrm{H} - \Sigma]^{-1}\,. \tag{3.18}$$

The interaction with the lead is taken into account via the self-energy Σ which is given by

$$\Sigma = \tau G^R_{\mathrm{C,isolated}} \tau^\dagger, \tag{3.19}$$

with the retarded Green's function of the isolated contact as

$$G^R_{\mathrm{C,isolated}} = [(\mathcal{E} + \imath\eta)\underline{\mathbf{I}} - \mathrm{H_C}]^{-1}\,. \tag{3.20}$$

A remarkable simplification is achieved, because the coupling parameter τ is only nonzero for points adjacent to the contact region. Hence, the Green's function of the isolated lead can usually be calculated analytically.
For the one-dimensional lattice, the self-energy due to a semi-infinite lead can be determined by the discretized Schrödinger equation at the boundary of the device and contact region.

$$\varepsilon_1\psi_1 = -t\psi_0 + (V_1 + 2t)\psi_1 - t\psi_2 \tag{3.21}$$

Here, ε_1 is given by equation (2.14) and $t = \hbar^2/(2ma^2)$ for an equidistant grid with constant mass. This assumption is eligible for the calculation of the self-energy of a semi-infinite wire [27]. To eliminate the wavefunction ψ_0 just outside the device, one has to consider, that the retarded Green's function gives the response for excitation within the device and therefore only outgoing waves are to be assumed at the boundaries.

$$\psi_0 = \psi_1 \exp(\imath k_1 a) \tag{3.22}$$

Therefore, the Schrödinger equation at the boundary becomes

$$\varepsilon_1\psi_1 = -t\exp(\imath k_1 a)\,\psi_1 + (V_1 + 2t)\psi_1 - t\psi_2 \tag{3.23}$$

Hence, the self-energy of a semi-infinite lead on the left of the device is a matrix with only one non-zero element at the upper left:

$$\Sigma^{\mathrm{R}}_{\mathrm{L};1,1}(\mathcal{E}) = -t\exp(\imath k_1 a) \tag{3.24}$$

Similarly, the self-energy of the right lead is given by the non-zero element

$$\Sigma^{\mathrm{R}}_{\mathrm{R};N,N}(\mathcal{E}) = -t\exp(\imath k_2 a) \tag{3.25}$$

where the wave vectors are to be determined via the dispersion relation and therefore give the energy dependence of the self-energies.
The retarded Green's function with a $N \times N$ Hamiltonian of the device region and the self-energies Σ^{R}_i that take the leads into account exactly, is given by

$$G^R(\mathcal{E}) = \left[\mathcal{E}\underline{\mathbf{I}} - \mathrm{H} - \Sigma^{\mathrm{R}}_{\mathrm{L}} - \Sigma^{\mathrm{R}}_{\mathrm{R}}\right]^{-1}. \tag{3.26}$$

The self-energies are non-Hermitian and their anti-Hermitian parts are given by

$$\Gamma_{\mathrm{L}} = \imath\left[\Sigma^{\mathrm{R}}_{\mathrm{L}} - \Sigma^{\mathrm{A}}_{\mathrm{L}}\right] = -2\Im\left\{\Sigma^{\mathrm{R}}_{\mathrm{L}}\right\} = \frac{\hbar}{\tau_{\mathrm{L}}(\mathcal{E})} \tag{3.27}$$

$$\Gamma_{\mathrm{R}} = \imath\left[\Sigma^{\mathrm{R}}_{\mathrm{R}} - \Sigma^{\mathrm{A}}_{\mathrm{R}}\right] = -2\Im\left\{\Sigma^{\mathrm{R}}_{\mathrm{R}}\right\} = \frac{\hbar}{\tau_{\mathrm{R}}(\mathcal{E})} \tag{3.28}$$

which are called broadening. They can be seen as the scattering rate of the electrons in the device into the lead region and vice versa [27, 28]. Having calculated the retarded Green's function, we are able to determine the requested physical quantities. The density of states is given by

$$\rho(\mathbf{x},\mathbf{x},\mathcal{E}) = -\frac{1}{\pi}\Im\left\{G^{\mathrm{R}}(\mathbf{x},\mathbf{x},\mathcal{E})\right\}, \tag{3.29}$$

but to obtain the electron density an integration over energy space is necessary. The electron density at grid point i of an equidistant grid with grid spacing a writes as [28]:

$$n_i = -\frac{2\imath}{a}\int\left[G^{\mathrm{R}}_{i,i}\Sigma^{<}_{\mathrm{L}}G^{\mathrm{A}}_{i,i} + G^{\mathrm{R}}_{i,i}\Sigma^{<}_{\mathrm{R}}G^{\mathrm{A}}_{i,i}\right]\frac{\mathrm{d}\mathcal{E}}{2\pi}. \tag{3.30}$$

The new quantity introduced here is the lesser self-energy. It is given by [29]

$$\Sigma^{<}_{\mathrm{L}}(\mathcal{E}) = \imath\Gamma_{\mathrm{L}} f_{\mathrm{L}}(\mathcal{E}), \tag{3.31a}$$

$$\Sigma^{<}_{\mathrm{R}}(\mathcal{E}) = \imath\Gamma_{\mathrm{R}} f_{\mathrm{R}}(\mathcal{E}), \tag{3.31b}$$

for the left and right lead, respectively, where $f_{\mathrm{L}}(\mathcal{E})$ and $f_{\mathrm{R}}(\mathcal{E})$ are the Fermi-Dirac occupation functions. Furthermore, this integral may include the effect of the transverse

direction by a modified occupation function as pointed out in Section 2.2.2. Similarly, the current density from grid point i to grid point $i+1$ is given by

$$j_{i,i+1} = q_0 \frac{\hbar}{2ma^2} 2 \int \left[G^{\mathrm{R}}_{i,i+1} \Sigma^{<}_{\mathrm{L}} G^{\mathrm{A}}_{i,i+1} - G^{\mathrm{R}}_{i+1,i} \Sigma^{<}_{\mathrm{R}} G^{\mathrm{A}}_{i+1,i} \right] \frac{\mathrm{d}\mathcal{E}}{2\pi}. \tag{3.32}$$

A different way to define the electron and current density is achieved by using correlation functions. The lesser Green's function is determined by the equation

$$\left[\mathcal{E}\underline{\mathbf{I}} - \mathrm{H} - \Sigma^{\mathrm{R}}_{\mathrm{L}} - \Sigma^{\mathrm{R}}_{\mathrm{R}} \right] G^{<}(\mathcal{E}) = \Sigma^{<}(\mathcal{E})\, G^{\mathrm{A}}(\mathcal{E}), \tag{3.33}$$

where $\Sigma^{<}$ is the self-energy matrix due to the leads containing the non-zero elements $\Sigma^{<}_{1,1} = \Sigma^{<}_{\mathrm{L}}$ and $\Sigma^{<}_{N,N} = \Sigma^{<}_{\mathrm{R}}$. After solving for $G^{<}$ by a full matrix inversion, the electron and current densities (coherent transport, [28]), are given by

$$n_i = -\frac{2\imath}{a} \int G^{<}_{i,i}(\mathcal{E}) \frac{\mathrm{d}\mathcal{E}}{2\pi}, \tag{3.34a}$$

$$j_{i,i+1} = q_0 \frac{\hbar}{2ma^2} 2 \int \left[G^{<}_{i,i+1}(\mathcal{E}) - G^{<}_{i+1,i}(\mathcal{E}) \right] \frac{\mathrm{d}\mathcal{E}}{2\pi}. \tag{3.34b}$$

The evaluation of the electron and current densities demands two numerical operation. First, the inversion and the multiplications to obtain the retarded and lesser Green's functions are very time costly. To circumvent this problem, the recursive Green's function algorithm was developed, which will be presented in the succeeding section. Second, the integration over energy spaces requires special care. Small peaks within the energy integration in the Green's functions need to be resolved correctly but simultaneously the number of energy grid points for the numerical integration should be kept low due to memory requirements. Therefore an adaptive numerical integration method was developed (cf. Section 3.3).

3.2.3 Recursive Green's Function Algorithm

The inversion of a matrix is a very time consuming computer operation. Since only the diagonal and first off-diagonal elements of the retarded and lesser Green's function are needed, an algorithm that only calculates these elements is desirable. The recursive Green's function algorithm by Svizhenko [10] accomplishes this demand.

Recursive Algorithm for the Retarded Green's Function

The retarded Green's function G^{R} of a one-dimensional system given by a $N \times N$ Hamiltonian is defined by

$$\left(\mathcal{E}\underline{\mathbf{I}} - \mathrm{H} - \Sigma_{\mathrm{L}} - \Sigma_{\mathrm{R}} - \Sigma_{\mathrm{S}} \right) G^{\mathrm{R}} = \mathrm{A} G^{\mathrm{R}} = \underline{\mathbf{I}}, \tag{3.35}$$

where Σ_{L} and Σ_{R} are the self-energies due to the left and right lead and Σ_{S} is the self-energy due to scattering events, which can be combined into the retarded self-energy

Algorithm 1 Recursive algorithm for the retarded Green's function

$G^{\mathrm{Rl},1}_{1,1} := \dfrac{1}{\mathrm{A}_{1,1}}$ ▷ Initialize first element
for $i = 1 : N-1$ **do**
  $G^{\mathrm{Rl},i+1}_{i+1,i+1} := \dfrac{1}{\mathrm{A}_{i+1,i+1} - \mathrm{A}_{i+1,i} G^{\mathrm{Rl},i}_{i,i} \mathrm{A}_{i,i+1}}$ ▷ Left connected Green's function
end for
$G^{\mathrm{R}}_{N,N} := G^{\mathrm{Rl},N}_{N,N}$ ▷ Nth element of ▷ retarded Green's function
for $i = N-1 : 1$ **do**
  $G^{\mathrm{R}}_{i+1,i} := -G^{\mathrm{R}}_{i+1,i+1} \mathrm{A}_{i+1,i} G^{\mathrm{Rl},i}_{i,i}$ ▷ Off-diagonal element
  $G^{\mathrm{R}}_{i,i+1} := -G^{\mathrm{Rl,i}}_{i,i} \mathrm{A}_{i,i+1} G^{\mathrm{R}}_{i+1,i+1}$ ▷ Off-diagonal element
  $G^{\mathrm{R}}_{i,i} := G^{\mathrm{Rl},i}_{i,i} - G^{\mathrm{Rl},i}_{i,i} \mathrm{A}_{i,i+1} G^{\mathrm{R}}_{i+1,i}$ ▷ Diagonal element
end for

$\Sigma^{\mathrm{R}} = \Sigma_{\mathrm{L}} + \Sigma_{\mathrm{R}} + \Sigma_{\mathrm{S}}$. The left connected Green's function $G^{\mathrm{Rl},i}$ is defined by the first $i \times i$ elements of (3.35).

$$\mathrm{A}_{1:i,1:i} G^{\mathrm{Rl},i} = \underline{\mathbf{I}}_{i\times i}. \tag{3.36}$$

Similarly, the $(i+1) \times (i+1)$ dimensional left connected Green's function $G^{\mathrm{Rl},i+1}$ is given. The element $G^{\mathrm{Rl},i+1}_{i+1,i+1}$ can be expressed via $G^{\mathrm{Rl},i}$ by using Dyson's equation [14,28]

$$G^{\mathrm{Rl},i+1}_{i+1,i+1} = \frac{1}{\mathrm{A}_{i+1,i+1} - \mathrm{A}_{i+1,i} G^{\mathrm{Rl},i}_{i,i} \mathrm{A}_{i,i+1}}. \tag{3.37}$$

The last element $G^{\mathrm{Rl},N}_{N,N}$ is equal to the fully connected retarded Green's function $G^{\mathrm{R}}_{N,N}$. The remaining elements of the fully connected retarded Green's function are to be calculated by the relation

$$\begin{aligned} G^{\mathrm{R}}_{i,i} &= G^{\mathrm{Rl},i}_{i,i} + G^{\mathrm{Rl},i}_{i,i} \left(\mathrm{A}_{i,i+1} G^{\mathrm{R}}_{i+1,i+1} \mathrm{A}_{i+1,i} \right) G^{\mathrm{Rl},i}_{i,i} \\ &= G^{\mathrm{Rl},i}_{i,i} - G^{\mathrm{Rl},i}_{i,i} \mathrm{A}_{i,i+1} G^{\mathrm{R}}_{i+1,i}. \end{aligned} \tag{3.38}$$

The off-diagonal elements of the retarded Green's function are given by

$$G^{\mathrm{R}}_{i+1,i} = -G^{\mathrm{R}}_{i+1,i+1} \mathrm{A}_{i+1,i} G^{\mathrm{Rl},i}_{i,i}, \tag{3.39a}$$

$$G^{\mathrm{R}}_{i,i+1} = -G^{\mathrm{Rl,i}}_{i,i} \mathrm{A}_{i,i+1} G^{\mathrm{R}}_{i+1,i+1}. \tag{3.39b}$$

The diagonal and the first off-diagonal elements of the retarded Green's function are needed for the recursive algorithm for the electron correlation (i.e. lesser Green's) function. The whole recursive algorithm for the retarded Green's function is summarized in Alg. 1.

Algorithm 2 Recursive algorithm for the lesser Green's function

$G^{<\mathrm{l},1}_{1,1} := G^{\mathrm{Rl},1}_{1,1}\Sigma^{<}_{1,1}G^{\mathrm{Al},1}_{1,1}$ ▷ Initialize first element
for $i = 1 : N-1$ **do**
  $G^{<\mathrm{l},i+1}_{i+1,i+1} = G^{\mathrm{Rl},i+1}_{i+1,i+1}\left(\Sigma^{<}_{i+1,i+1} + \sigma^{<}_{i+1}\right)G^{\mathrm{Al},i+1}_{i+1,i+1}$ ▷ Left connected Green's function
end for
$G^{<}_{N,N} := G^{<\mathrm{l},N}_{N,N}$ ▷ Nth element of ▷ lesser Green's function
for $i = N-1 : 1$ **do**
  $G^{<}_{i+1,i} = G^{\mathrm{R}}_{i+1,i+1}\mathrm{A}_{i+1,i}G^{<\mathrm{l},i}_{i,i} + G^{<}_{i+1,i+1}\mathrm{A}^{\dagger}_{i+1,i}G^{\mathrm{Al},i}_{i,i}$ ▷ Off-diagonal element
  $G^{<}_{i,i} = G^{<\mathrm{l},i}_{i,i} + G^{\mathrm{Rl},i}_{i,i}\left(\mathrm{A}_{i,i+1}G^{<}_{i+1,i+1}\mathrm{A}^{\dagger}_{i+1,i}\right)G^{\mathrm{Al},i}_{i,i}$
  $+\left[G^{<\mathrm{l},i}_{i,i}\mathrm{A}^{\dagger}_{i,i+1}G^{\mathrm{A}}_{i+1,i} + G^{\mathrm{R}}_{i,i+1}\mathrm{A}_{i+1,i}G^{<\mathrm{l},i}_{i,i}\right]$ ▷ Diagonal element
end for

Recursive Algorithm for the Lesser Green's Function

The constituting equation of the lesser Green's function writes as

$$\left(\mathcal{E}\underline{\mathbf{I}} - \mathrm{H} - \Sigma^{\mathrm{R}}\right)G^{<} = \mathrm{A}G^{<} = \Sigma^{<}G^{\mathrm{A}}. \tag{3.40}$$

Here $\Sigma^{<}$ is the lesser self-energy and G^{A} is the advanced Green's function, i.e. the Hermitian conjugate of the retarded Green's function. A left connected Green's function is defined

$$\mathrm{A}_{1:i,1:i}G^{<\mathrm{l},i} = \Sigma^{<}_{1:i,1:i}G^{\mathrm{Al},i}_{1:i,1:i}, \tag{3.41}$$

which also allows the calculation of $G^{<\mathrm{l},i+1}$ using a recursive algorithm,

$$G^{<\mathrm{l},i+1}_{i+1,i+1} = G^{\mathrm{Rl},i+1}_{i+1,i+1}\left(\Sigma^{<}_{i+1,i+1} + \sigma^{<}_{i+1}\right)G^{\mathrm{Al},i+1}_{i+1,i+1}, \tag{3.42}$$

with $\sigma^{<}_{i+1} = \mathrm{A}_{i+1,i}G^{<\mathrm{l},i}_{i,i}\mathrm{A}^{\dagger}_{i,i+1}$. The self-energies are assumed to be diagonal matrices. The knowledge of the left connected lesser Green's function and the main and second diagonals of the retarded Green's function permits the calculation of the electron correlation function. Its second diagonal is given by

$$G^{<}_{i+1,i} = G^{\mathrm{R}}_{i+1,i+1}\mathrm{A}_{i+1,i}G^{<\mathrm{l},i}_{i,i} + G^{<}_{i+1,i+1}\mathrm{A}^{\dagger}_{i+1,i}G^{\mathrm{Al},i}_{i,i} \tag{3.43}$$

which is used for the calculation of the main diagonal

$$G^{<}_{i,i} = G^{<\mathrm{l},i}_{i,i} + G^{\mathrm{Rl},i}_{i,i}\left(\mathrm{A}_{i,i+1}G^{<}_{i+1,i+1}\mathrm{A}^{\dagger}_{i+1,i}\right)G^{\mathrm{Al},i}_{i,i}$$
$$+\left[G^{<\mathrm{l},i}_{i,i}\mathrm{A}^{\dagger}_{i,i+1}G^{\mathrm{A}}_{i+1,i} + G^{\mathrm{R}}_{i,i+1}\mathrm{A}_{i+1,i}G^{<\mathrm{l},i}_{i,i}\right]. \tag{3.44}$$

The presented algorithm allows the evaluation of the correlation functions and hence, the desired physical quantities by a highly efficient algorithm without time consuming matrix-matrix operations. The recursive algorithm for the lesser Green's function is finally composed by the steps illustrated in Alg. 2.

3.2.4 Analogies to QTBM

Using the quantum transmitting boundary method, the equation system to be solved writes as

$$\underbrace{\begin{bmatrix} \alpha_1 & \beta_1 & & & & & \\ -s_1 & d_1-\mathcal{E} & -s_2 & & & & \\ & -s_2 & d_2-\mathcal{E} & -s_3 & & & \\ & & \ddots & \ddots & \ddots & & \\ & & & -s_n & d_n-\mathcal{E} & -s_{n+1} & \\ & & & & \beta_n & \alpha_n & \end{bmatrix}}_{\mathrm{D}} \underbrace{\begin{bmatrix} \psi_0 \\ \psi_1 \\ \psi_2 \\ \vdots \\ \psi_n \\ \psi_{n+1} \end{bmatrix}}_{\underline{\mathbf{R}}} = \underbrace{\begin{bmatrix} a_1 \\ 0 \\ 0 \\ \vdots \\ 0 \\ a_n \end{bmatrix}}_{\underline{\mathbf{S}}} . \tag{3.45}$$

Comparing (3.45) with $\mathrm{D}\underline{\mathbf{R}} = \underline{\mathbf{S}}$ in Section 2.4.1, the matrix on the left hand side can be identified as the inverse of the retarded Green's function. Therefore, the quantum transmitting boundary method equation system is equivalent with the non-equilibrium Green's functions in the ballistic case,

$$\left[\mathcal{E}\underline{\mathbf{I}} - \mathrm{H} - \Sigma_{\mathrm{L}}^{\mathrm{R}} - \Sigma_{\mathrm{R}}^{\mathrm{R}}\right]\psi = \underline{\mathbf{S}} = \imath\Gamma. \tag{3.46}$$

The matrix coefficients a_1 and a_n (3.11) correspond to the self-energies of the left and the right lead contained in the broadening Γ in equation (3.46).

3.3 Adaptive Energy Integration

The numerical evaluation of the physical quantities requires a discretized representation of the energy space. A simple approach using an equidistant energy grid suffers from two problems. Too few grid points are not able to correctly resolve narrow resonances, whereas a vast number can lead to an unpredictable summation of numerical errors and to intractable memory requirements. These effects cause poor or even unstable convergency of a self-consistent Poisson loop [30]. Therefore, adaptive energy integration on a non-equidistant grid is the method of choice to increase accuracy, numerical stability, and memory efficiency.
An adaptive algorithm has been developed, which is depicted in Fig. 3.2. Additional grid points are inserted as long as the local error criterion regarding the electron concentration is not met. This procedure is repeated until the whole energy space is covered.

In the following sections different numerical integration methods implemented with adaptive grid refinement will be presented.

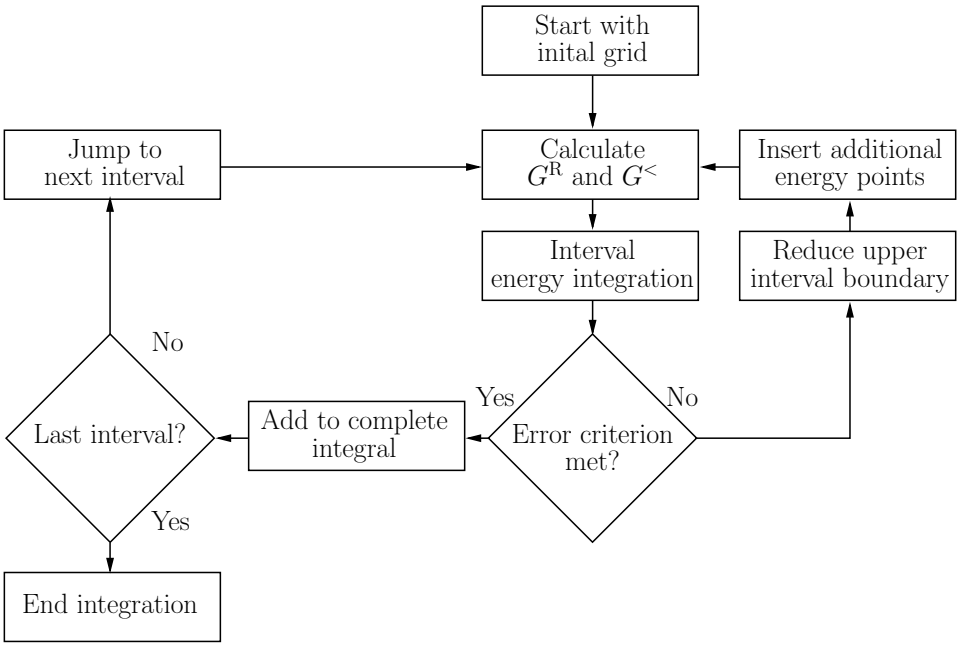

Figure 3.2: Illustration of the adaptive integration algorithm with grid refinement. Grid points are added as long as the error criterion is not met.

3.3.1 Simpson's Rule

The Simpson rule[1] is a closed Newton-Cotes rule of second order. The integral of an function $f(x)$ over an interval $[a, b]$ is given by

$$I_1 = \frac{b-a}{6}\left[f(a) + 4f\left(\frac{a+b}{2}\right) + f(b)\right]. \tag{3.47}$$

$f(x)$ is interpolated by a parabola, hence Simpson's rule gives an exact result for polynomials up to second degree only. One strategy to decrease the interpolation error is to subdivide the interval into two equal parts and to apply Simpson's rule on each subinterval. This leads to the composite Simpson's rule which, for five grid points, writes as

$$I_2 = \frac{b-a}{12}\left[f(a) + 4f\left(\frac{a+b}{4}\right) + 2f\left(\frac{a+b}{2}\right) + 4f\left(3\frac{a+b}{4}\right) + f(b)\right]. \tag{3.48}$$

An illustration of a grid on which these two rules are applied is depicted in Fig. 3.3. To obtain an error criterion for the adaptive integration algorithm (Fig. 3.2) mentioned before, the electron concentration within the current integration interval is calculated using the 3-point Simpson rule and the 5-point composite Simpson's rule. This leads to a local error which is compared to the desired tolerance factor τ

$$\left|\frac{I_1 - I_2}{I_2}\right| < \tau. \tag{3.49}$$

[1] after Thomas Simpson, English mathematician, 1710-1761

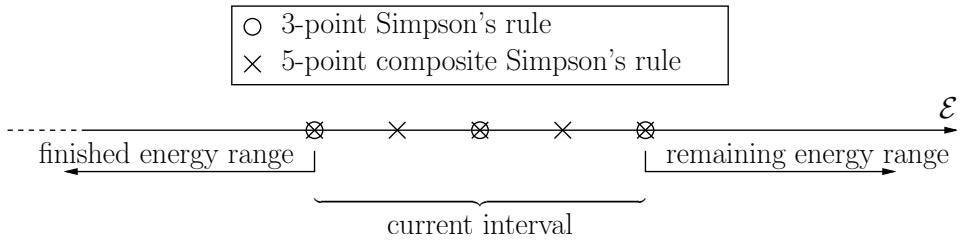

Figure 3.3: The deviation of two integration methods applied to the same integration interval is used as a local error criterion.

If the condition in equation (3.49) is met, the integral is accurate enough and no more grid refinement in the given interval is needed.

3.3.2 Akima Interpolation

The Akima interpolation is a method to fit curves as it would be done in a natural way by humans [31]. A piecewise function, composed of polynomials up to third degree, is fitted to the data points. The slopes of two adjacent points defines the polynomial between them. The interpolation method uses five grid points X_1, X_2, X_3, X_4 and X_5 to determine the slope t of the curve at point X_3 (cf. Fig. 3.4). m_1, m_2, m_3 and m_4 are the slopes of the line segments $\overline{X_1X_2}$, $\overline{X_2X_3}$, $\overline{X_3X_4}$ and $\overline{X_4X_5}$, respectively. Akima defines the slope t as

$$t = \frac{|m_4 - m_3|\, m_2 + |m_2 - m_1|\, m_3}{|m_4 - m_3| + |m_2 - m_1|}. \tag{3.50}$$

This imposes that $t = m_2$ if $m_1 = m_2$ and $m_3 \neq m_4$, and $t = m_3$ if $m_3 = m_4$ and $m_1 \neq m_2$. Furthermore, if $m_2 = m_3$ the slope becomes $t = m_2 = m_3$. Although the slope is not defined under the condition $m_1 = m_2 \neq m_3 = m_4$, Akima equates the slope to $t = \frac{1}{2}(m_2 + m_3)$. This assures invariance under a linear scale transformation of the coordinate system.
A piece of the curve between two consecutive grid points will be fitted in such a manner that the curve passes through the points and will have the slopes t_1 and t_2, determined by the procedure described above. This gives rise to four conditions which allow to calculate a polynomial of third order between two points (x_1, y_1) and (x_2, y_3)

$$f(x) = y_1 \quad \text{and} \quad f'(x) = t_1 \quad \text{at } x = x_1, \tag{3.51a}$$
$$f(x) = y_2 \quad \text{and} \quad f'(x) = t_2 \quad \text{at } x = x_2. \tag{3.51b}$$

An interpolation polynomial could be chosen to have the following form

$$f(x) = p_0 + p_1(x - x_1) + p_2(x - x_1)^2 + p_3(x - x_1)^3, \tag{3.52}$$

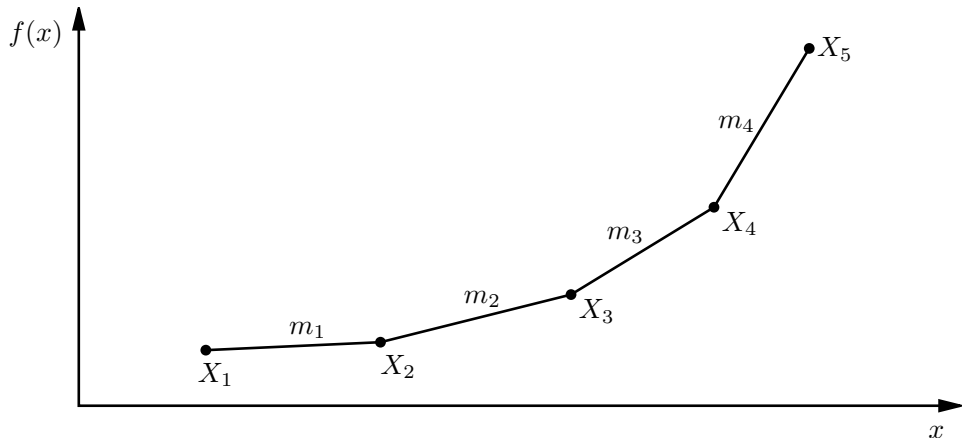

Figure 3.4: Points used to calculate the slope at point X_3

where the coefficients p_i are therefore given by

$$p_0 = y_1, \tag{3.53a}$$
$$p_1 = t_1, \tag{3.53b}$$
$$p_2 = \frac{3\dfrac{y_2 - y_1}{x_2 - x_1} - 2t_1 - t_2}{x_2 - x_1}, \tag{3.53c}$$
$$p_3 = \frac{t_1 + t_2 - 2\dfrac{y_2 - y_1}{x_2 - x_1}}{(x_2 - x_1)^2}. \tag{3.53d}$$

The interpolation polynomial (3.52) can be integrated easily. Hence, the integral of the fitted curve $f(x)$ in the interval $[x_1, x_2]$ writes as

$$F(x)\Big|_{x_1}^{x_2} = \frac{p_3}{4}(x_2 - x_1)^4 + \frac{p_2}{3}(x_2 - x_1)^3 + \frac{p_1}{2}(x_2 - x_1)^2 + p_0(x_2 - x_1). \tag{3.54}$$

3.3.3 Polynomial Interpolation

Simpson's rule is based on equidistant grid points and the interpolation polynomial is only of second order. Hence a more general approach with non-equidistant grid points and arbitrary degree would be eligible. For a monomial power basis the interpolation polynomial on N nodes takes the form

$$p(x) = a_1 + a_2 x + a_3 x^2 + \cdots + a_N x^{N-1} = \sum_{i=1}^{N} a_i x^{i-1}. \tag{3.55}$$

Algorithm 3 Fast Algorithm to solve Vandermonde system [32]

function VANDERMONDE($[x_1, x_2, \ldots, x_N], [y_1, y_2, \ldots, y_N]$)
  for $i = 1 : N$ **do**
    $a_i := y_i$ ▷ Copy **y** to **a**
  end for
  for $i = 1 : N$ **do**
    for $j = N : (-1) : i + 1$ **do**
      $a_j := (a_j - a_{j-1})/(x_j - x_{j-i})$ ▷ Apply divided differences scheme
    end for
  end for
  for $i = N - 1 : (-1) : 1$ **do**
    for $j = i : N - 1$ **do**
      $a_j := a_j - x_i a_{j+i}$ ▷ Apply Horner's rule
    end for
  end for
  return $[a_1, a_2, \ldots, a_N]$ ▷ Return coefficient vector **a**
end function

To obtain the coefficient vector $\mathbf{a} = [a_1, a_2, a_3, \ldots, a_N]^T$ it is necessary to solve a $N \times N$ dimensional equation system

$$\underbrace{\begin{bmatrix} 1 & x_1 & \cdots & x_1^{N-1} \\ 1 & x_2 & \cdots & x_2^{N-1} \\ \vdots & & \ddots & \vdots \\ 1 & x_N & \cdots & x_N^{N-1} \end{bmatrix}}_{\underline{\mathbf{V}}} \begin{bmatrix} a_1 \\ a_2 \\ \vdots \\ a_N \end{bmatrix} = \begin{bmatrix} y_1 \\ y_2 \\ \vdots \\ y_N \end{bmatrix}, \tag{3.56}$$

where $\underline{\mathbf{V}}$ is called the Vandermonde matrix. Unfortunately this system is very ill-conditioned and hence its solution numerically unstable. Björk and Pereyra [32] developed an algorithm (Alg. 3) that is able to calculate the coefficient vector **a** in a very fast and stable manner.
In a first step, divided differences are used to obtain the coefficients in Newton basis. The second step applies Horner's rule to compute the vector **a**. The algorithm never builds the whole equation system since only the grid point vector $\mathbf{x} = [x_1, x_2, \ldots, x_N]$ and the right-hand side vector $\mathbf{y} = [y_1, y_2, \ldots, y_N]$ are needed. Hence, no memory for the whole Vandermonde matrix $\underline{\mathbf{V}}$ needs to be associated.
After applying the Björck and Pereya algorithm to obtain the coefficients of the polynomial, the integral of the interval $[x_1, x_N]$ of the interpolation function can be calculated. For an arbitrary even number N of grid points, a subset of $(N + 1)/2$ grid points may be used to obtain a second polynomial and consequentially a second integral. These two results are then compared and yield the error criterion for the adaptive integration algorithm. Unfortunately polynomial interpolation functions on equidistant points suffer

from Runge's phenomenon for a higher degree. This results in oscillations towards the both ends of the interval which have to be carefully considered. They can be avoided by using non-equidistant grid points as done by the Clenshaw-Curtis Rule described in the succeeding section.

3.3.4 Clenshaw-Curtis Integration

A method to circumvent oscillations of the interpolation polynomial is to use a non-equidistant grid, i.e. to use more grid points at the interval borders. Fejér [33] proposed to use the zeros of the Chebyshev polynomial $T_n = \cos(n \arccos x)$ in the interval $]-1, 1[$ as quadrature points of the integral of $f(x)$,

$$\int_{-1}^{1} f(x)\mathrm{d}x = \sum_{k=0}^{n} w_k f(x_k). \tag{3.57}$$

For Fejér's second rule, the $n-1$ extreme points of T_n are used. Clenshaw and Curtis [34] extended this open rule to a closed form which includes the boundary points $x_0 = -1$ and $x_n = 1$ of the interval $[-1, 1]$, i.e. the $n+1$ quadrature points are to be found at

$$x_k := \cos(\vartheta_k), \quad \vartheta_k := k\frac{\pi}{n}, \quad k = 0, 1, \ldots, n. \tag{3.58}$$

The weights w_k of equation (3.57) are to be obtained by an explicit expression or by means of discrete Fourier transforms [35]. For a low number of n, the explicit expressions of the Clenshaw-Curtis weights are sufficient regarding calculation speed and numerical accuracy, determined by:

$$w_k = \frac{c_k}{n}\left(1 - \sum_{j=1}^{\lfloor n/2 \rfloor} \frac{b_j}{4j^2 - 1}\cos(2j\vartheta_k)\right), \quad k = 0, 1, \ldots, n. \tag{3.59}$$

The coefficients b_j and c_k are defined as

$$b_j = \begin{cases} 1, & \text{if } j = n/2 \\ 2, & \text{if } j < n/2 \end{cases} \quad \text{and} \quad c_k = \begin{cases} 1, & \text{if } k = 0 \mod n \\ 2, & \text{otherwise.} \end{cases} \tag{3.60}$$

A useful property of the Clenshaw-Curtis rule is the possibility to create subsets of the quadrature nodes, i.e. to move from $n+1$ points to $2n+1$ points only the function values of the inserted n points need to be evaluated.

3.3.5 Comparison of Integration Methods

Concluding this section, a comparison of the advantages and disadvantages of the presented adaptive integration methods is given. In order to achieve convergence within a self-consistent NEGF-Poisson loop using Simpson's rule, a stringent error criterion has

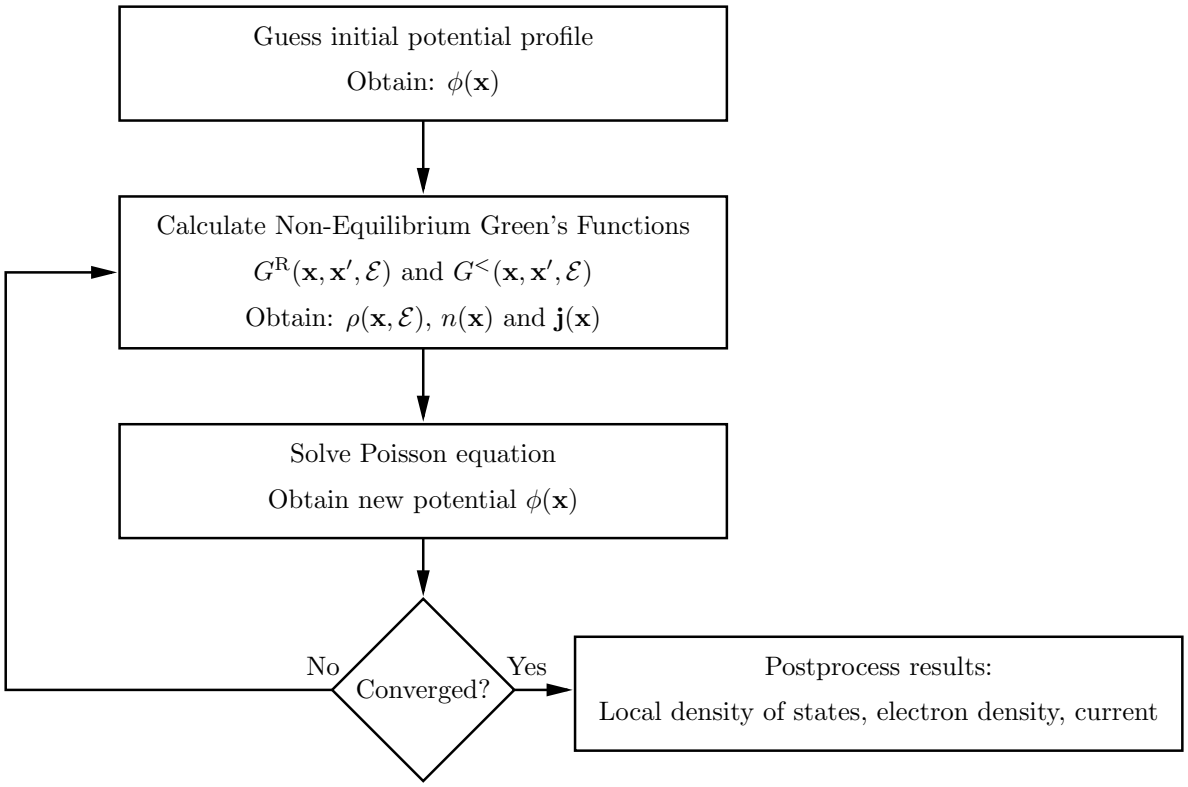

Figure 3.5: Self consistent calculation of potential and electron density

been necessary, which leads to a huge amount of grid points. The Akima interpolation has not proven suitable for the application in the Green's function solver, as it did not allow a stable grid refinement for sudden strong variations in the local density of states. The polynomial interpolation worked best for an order of five and nine but suffered from Runge's phenomenon for a higher polynomial degree. The Clenshaw-Curtis integration is based on an interpolation method using Chebyshev nodes and therefore circumvents this disadvantage. Because of its numerical stability, computation time, and memory consumption the two latter approaches rendered most applicable within the NEGF formalism.

3.4 Self Consistent Solution

Charged carriers within a semiconductor device influence the electrostatic potential, which is expressed by Poisson's equation

$$\nabla \cdot (\tilde{\varepsilon} \nabla \phi) = \varrho. \tag{3.61}$$

In semiconductors charge is due to ionized dopants (N_{A} and N_{D}), electrons and holes.

$$\varrho(\phi) = -q_0\big(n(\phi) - p(\phi) + N_{\mathrm{A}} - N_{\mathrm{D}}\big) \tag{3.62}$$

Charge itself depends on the electrostatic potential since electron and hole concentrations are influenced by the band edge energy and the Fermi level. Therefore it is necessary to calculate the space charge distribution obtained through the non-equilibrium Green's functions and the potential profile resulting from Poisson's equation within a self consistent iteration scheme. The basic principle is depicted in Fig. 3.5. A Poisson solver using a predictor corrector approach is provided by the Vienna Schrödinger Poisson Solver [12]. This scheme requires an estimation of the local derivative of the carrier concentration with respect to the electrostatic potential $\mathrm{d}\varrho/\mathrm{d}\varphi$. The non-equilibrium Green's functions formalism allows to obtain the carrier concentration and this derivative in a similar manner.

We have to remember that what we observe is not nature herself, but nature exposed to our method of questioning.

WERNER HEISENBERG

CHAPTER 4

Results

The non-equilibrium Green's functions method as described in the previous chapters was implemented in C++ within the framework of the Vienna Schrödinger Poisson solver developed at the Institute for Microelectronics at the Technical University of Vienna [36]. Ballistic quantum transport is simulated for a simple single barrier. The local density of states, the occupation and its transmission function have been evaluated. Furthermore, resonant tunneling has been investigated. The results are split into two parts. First a linear potential drop across the device was assumed. Then the effects of charge on the band edge was taken into account by a self-consistent solution with the Poisson equation. The simulation output of the one-dimensional physical quantities is given as a .crv file. They were processed with XMGRACE. Two-dimensional quantities such as the local density of states have been displayed using the IBM DATA EXPLORER.

4.1 Single Barrier

A symmetric rectangular potential barrier with a height of $V_0 = 0.5\,\text{eV}$ and the width of 6 nm was simulated first. The effective mass $m_x = 0.05m_0$ is assumed to be constant across the whole simulation region.
In Figure 4.1, the local density of states of the unbiased barrier is shown. Because of the ballistic simulation, the interference due to the reflections of the electrons at the barrier can be seen clearly. The band edge of the device is marked in red. It is recognizeable that the electrons are allowed to penetrate into the barrier, which would be forbidden classically. This is also illustrated in Figure 4.2 showing the energetic distribution of the electrons in the semiconductor structure by occupying the local density of states.
The last figure for the rectangular barrier shows its transmission coefficient plotted over the energy range from 0 to 1 eV (Fig. 4.3). Comparison with the analytical result for the same barrier depicted in Figure 2.6 shows perfect agreement.

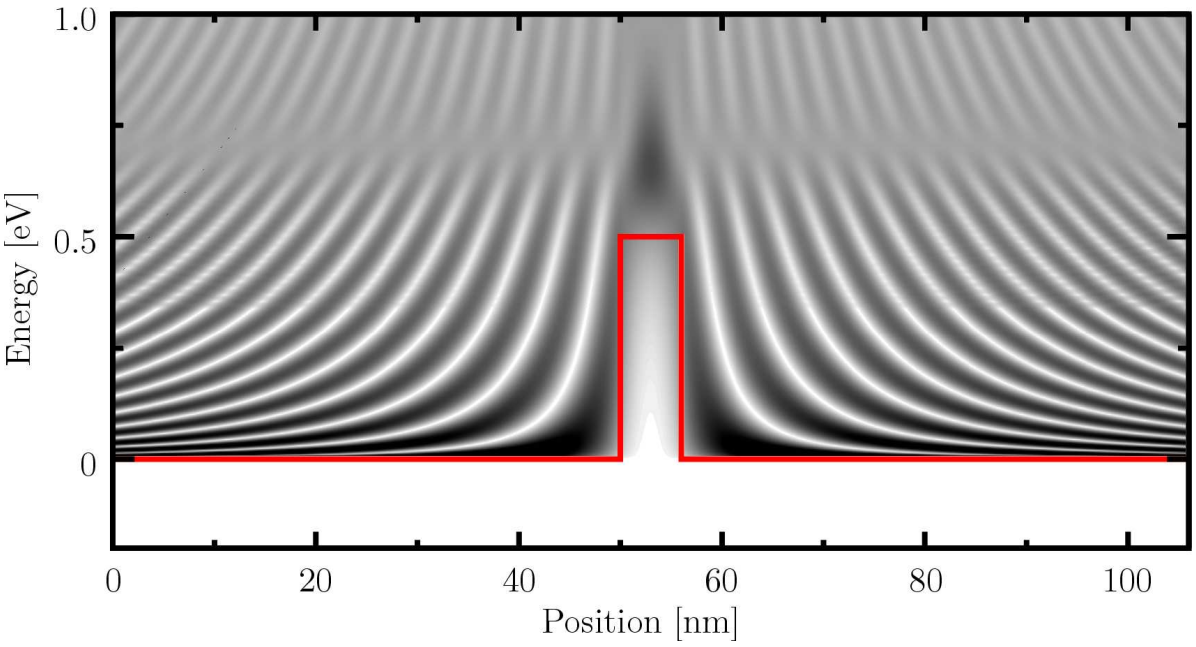

Figure 4.1: The local density of states of a single barrier with a height of 0.5 eV and a width of 6 nm. The effective mass $m_x = 0.05m_0$ is assumed to be constant across the whole device. The band edge is marked by a red line.

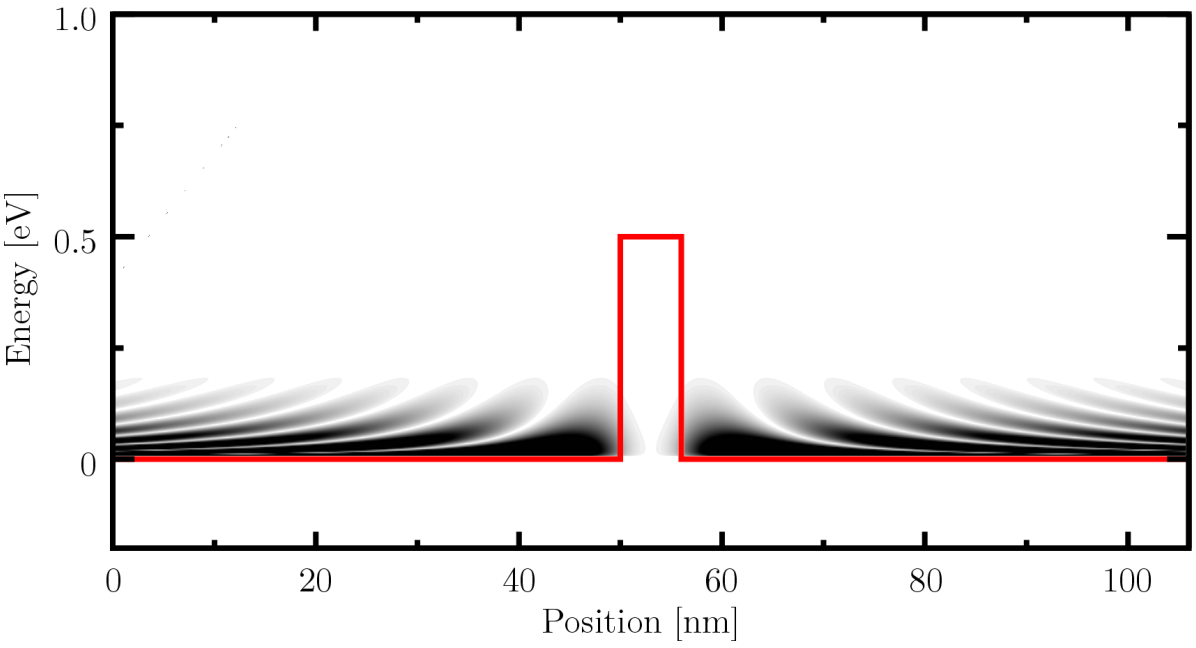

Figure 4.2: Occupied density of states for a single barrier.

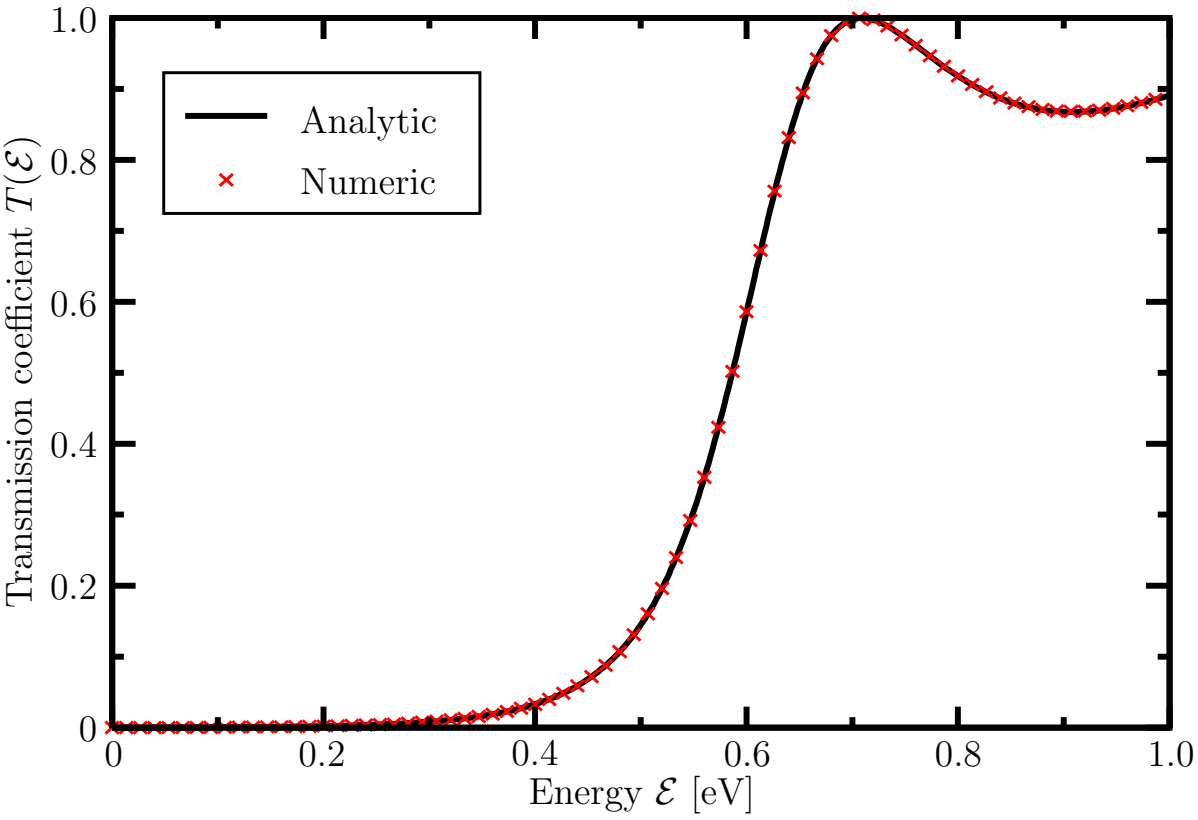

Figure 4.3: Transmission coefficient plotted over energy for the device in Figure 4.1. The numerical solution perfectly agrees with the analytical calculation.

4.2 Resonant Tunneling Diodes

This section provides the results of a simulation of a GaAs/AlAs/GaAs resonant tunneling device. The AlAs barriers are 1.355 eV high and 3 nm wide. They are separated from the contact region by an undoped 2 nm GaAs spacer layer. The contacts are made of a 50 nm region with a doping of $N_\mathrm{D} = 1.0 \times 10^{18}\,\mathrm{cm}^{-3}$ and a highly doped 20 nm layer next to the lead with $N_\mathrm{D} = 5.0 \times 10^{18}\,\mathrm{cm}^{-3}$. The well is made of undoped GaAs with a width of 9 nm. The effective mass of GaAs is $m_{x,\mathrm{GaAs}} = 0.067 m_0$ and for AlAs $m_{x,\mathrm{AlAs}} = 0.15 m_0$. The device is discretized on a uniform spatial grid with a constant grid spacing of $\Delta x = 0.1\,\mathrm{nm}$.
This section is divided into two parts. The results assuming a linear potential drop across the double barrier structure are shown in the succeeding Section 4.2.1. The self-consistent solution is given in Section 4.2.2.

4.2.1 Linear Potential Drop

For the simulations in this section, the potential drop under bias occurs over the spacer, barrier and well layers. In the contact regions, the potential is assumed to be constant.

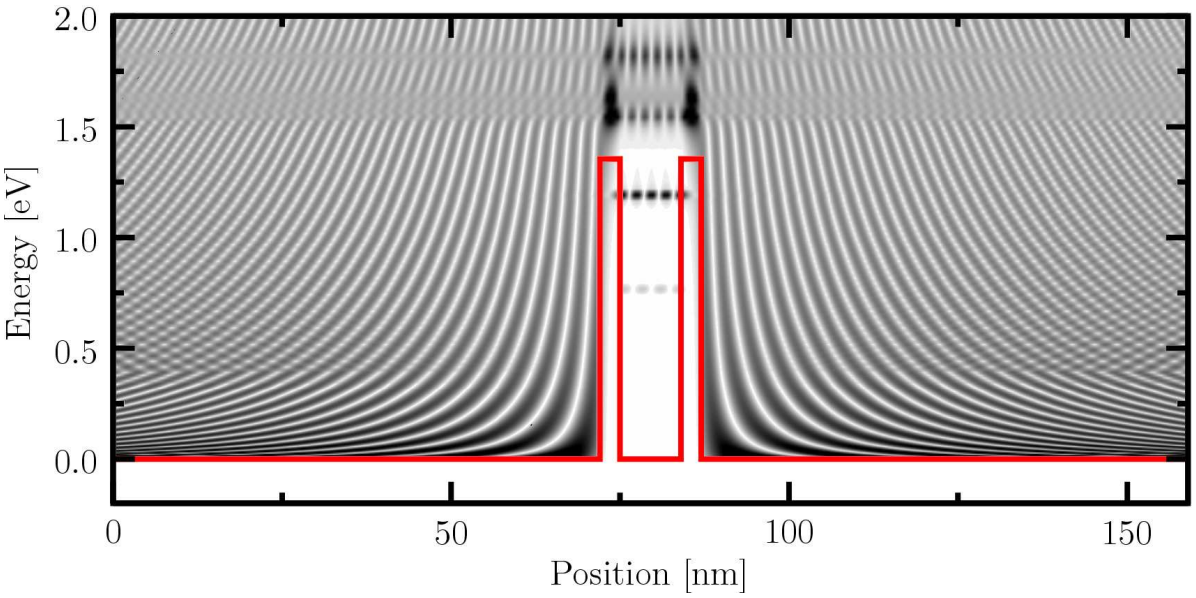

Figure 4.4: Local density of states of a GaAs/AlAs/GaAs resonant tunneling device with a barrier width of 3 nm and height of 1.355 eV. The GaAs well width is 9 nm. The effective mass of GaAs is $m_{x,\mathrm{GaAs}} = 0.067m_0$ and for AlAs $m_{x,\mathrm{AlAs}} = 0.15m_0$. The density of states of the lowest quasi-bound states in the well is too low to be visualized, only the fourth and fifth resonance can be seen clearly. As for the single barrier structure in Section 4.1 wave function penetration into the barriers occur.

Figure 4.4 shows the local density of states of the double barrier structure described in Section 4.2 without bias. The wave function penetration of the electrons into the barriers can be seen clearly. It is important to note, that the value of the local density of states of the lowest resonant states within the well is too low to be displayed. However, the higher quasi-bound states can be recognized at an energy level of about 0.75 eV.
Assuming a linear potential drop, the local density of states of the RTD under a bias of 0.3 V is shown in Figure 4.5.
In Figures 4.6 and 4.7 the occupied states are depicted without and with applied bias, respectively. Under bias, that is chosen around the second resonance, the occupation in the well can be seen clearly.
The transmission probability for this structure is illustrated in Figure 4.8. The sharply peaked resonances reach a transmission of 1.
The current-voltage curve in Figure 4.9 shows that for a decreasing well width, the resonance levels are shifted to higher energies. The peaks in the IV-curve are therefore shifted to higher voltages. After a resonance the negative differential resistance, that is typical for a resonant tunnel device, is reproduced.

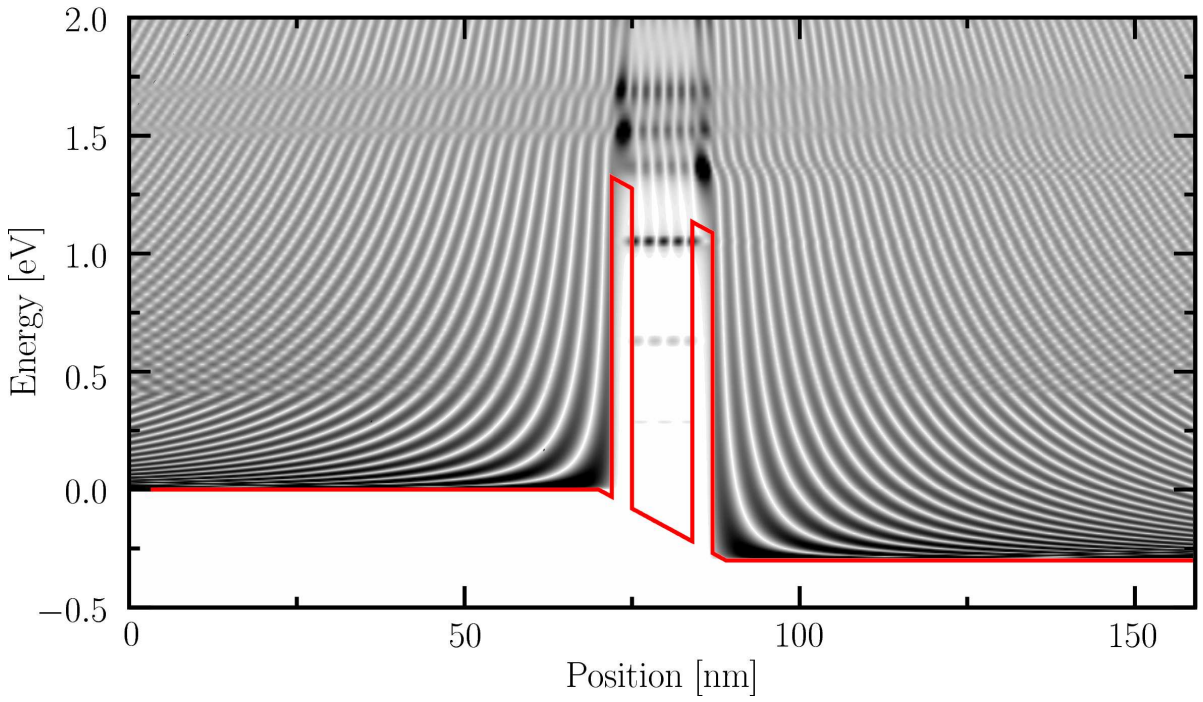

Figure 4.5: Local density of states for the resonant tunneling device with a bias of 0.3 V.

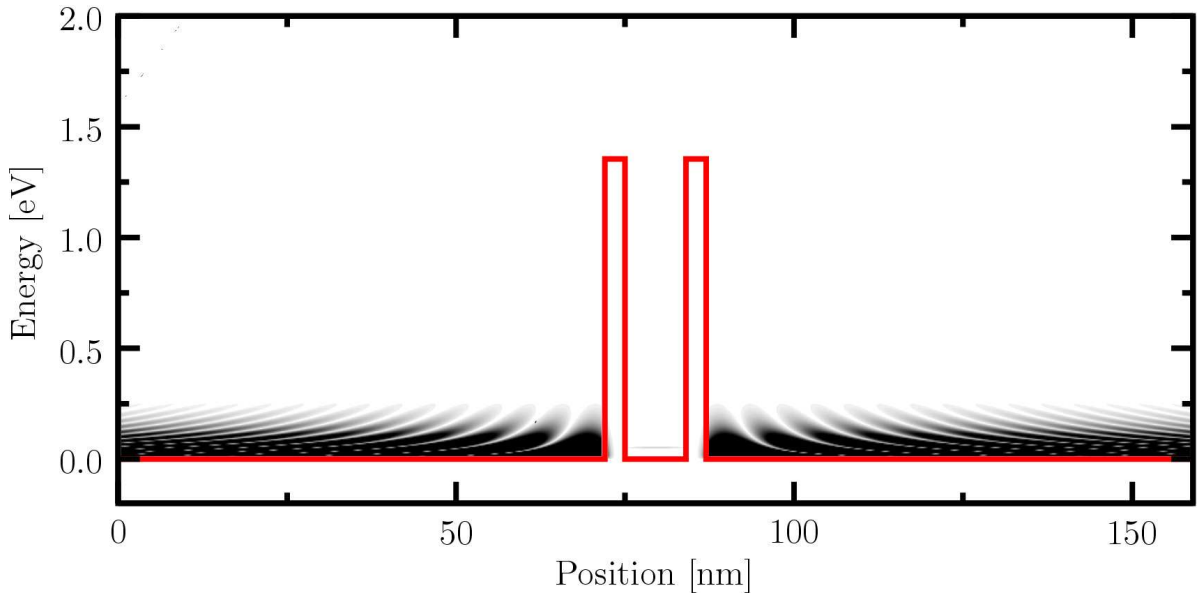

Figure 4.6: Occupied density of states of the RTD without bias.

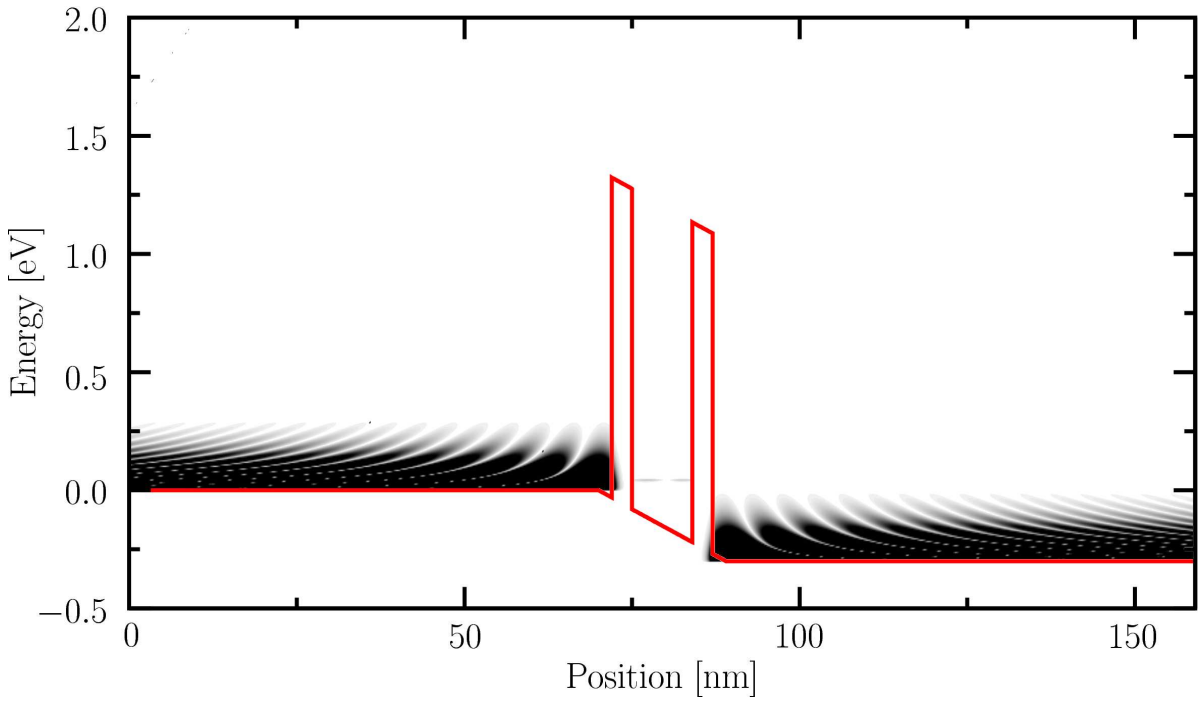

Figure 4.7: Occupied density of states of the RTD in Figure 4.4 with applied bias of 0.3 V. The occupation of the second quasi-bound state in the well can be seen.

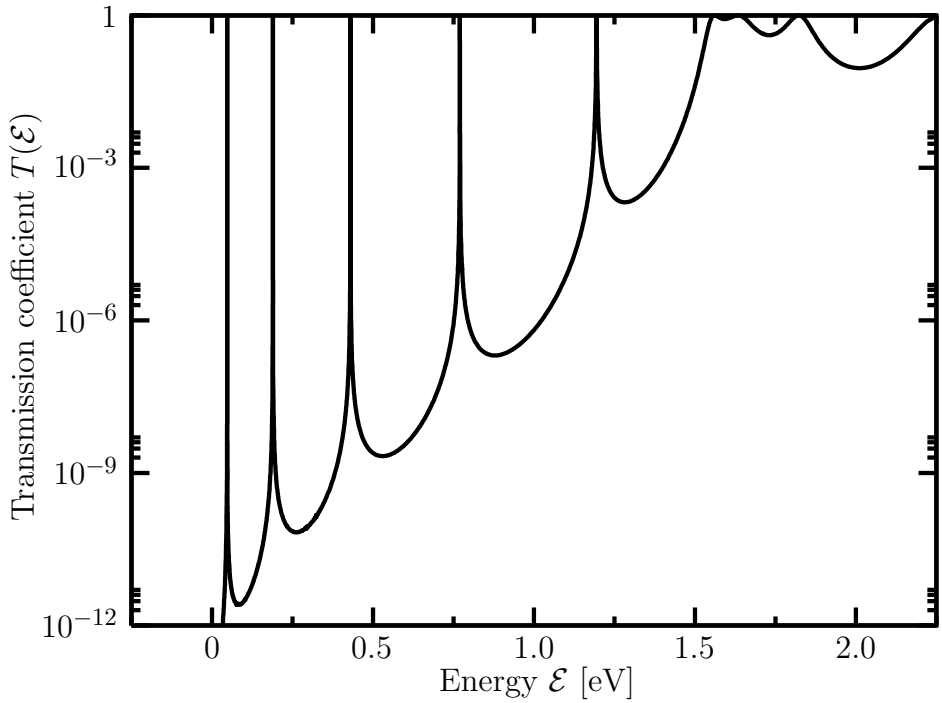

Figure 4.8: Calculated transmission probability of the resonant tunneling device presented in Figure 4.4. The sharp resonances reach a transmission probability of 1.

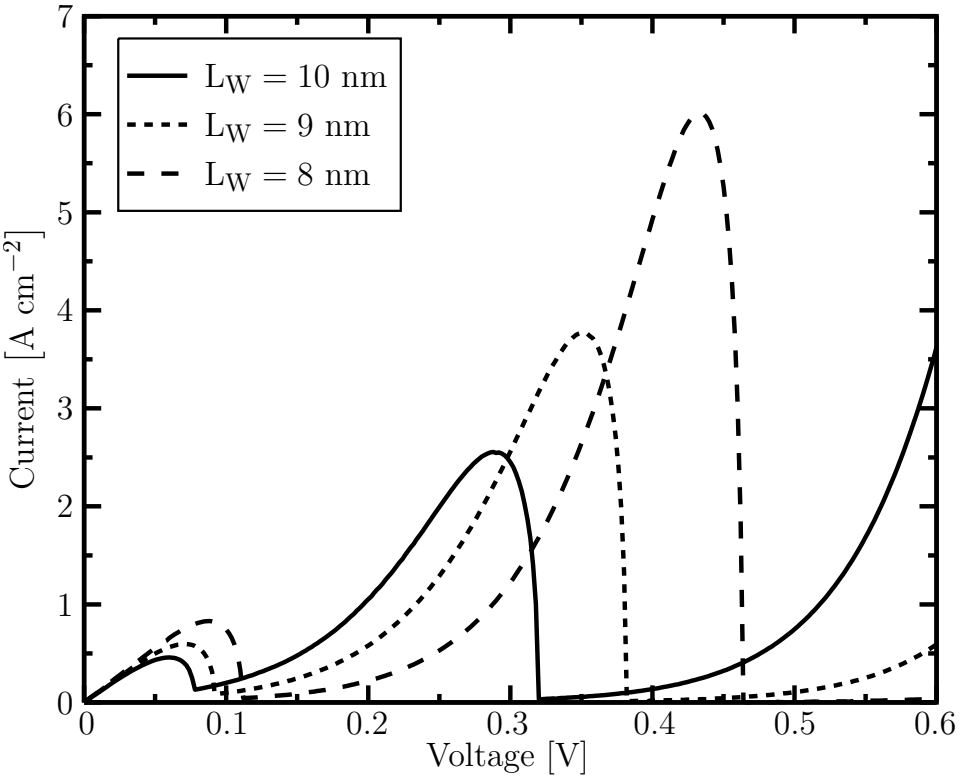

Figure 4.9: Calculation of a current-voltage curve of the double barrier structure in Fig. 4.4 with three different well widths. A reduction of the well width shifts the resonance levels to higher energies. Hence, the peaks in the IV-curve occur at higher bias.

4.2.2 Self Consistent Simulation

The double barrier device is simulated within a self-consistent loop of the non-equilibrium Green's functions solver and the Poisson solver.
Using the self-consistent Schrödinger-Poisson loop, the resulting local density of states of the resonant tunneling device is illustrated in Figure 4.10. A higher doping within the contact region leads to a bending of the conduction band edge. Likewise, the carriers in the GaAs well have an effect on the band edge. The influence of the spacer layer on the left and the right of the barriers is shown. Due to the sharpness of the first resonant state, it could not be displayed in the figure. The other quasi-bound states can be identified.
In Figure 4.11 the local density of states is given for a bias of 0.46 V. This is around the second resonant level. A triangular potential well that forms in the left contact region can be recognized. Electrons incident from the left device region are able to occupy the quasi-bound state in the well, that lies at the same energy level. This is depicted likewise in Figure 4.13 which shows the occupation of the states and especially the quasi-bound states in the well. The electrons filling the contact regions are clearly distinguishable.
Figure 4.12 gives the occupation of the density of states if no bias is applied.

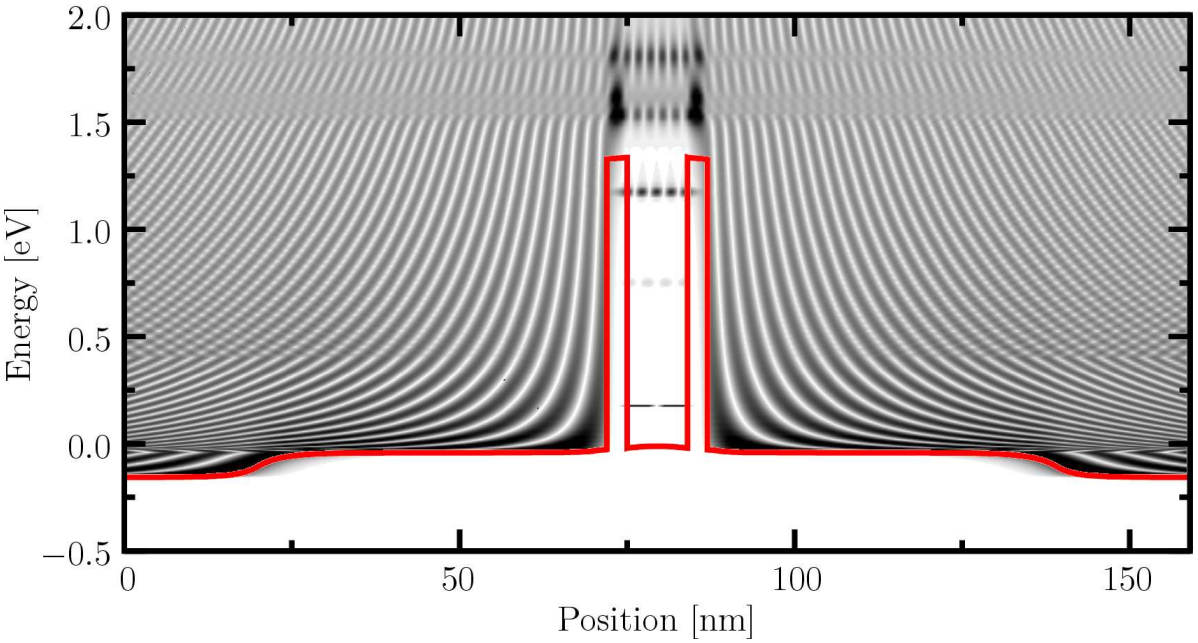

Figure 4.10: Local density of states of a GaAs/AlAs/GaAs resonant tunneling device with a barrier width of 3 nm and height of 1.355 eV. A GaAs well width of 9 nm is assumed. As effective mass of GaAs $m_{x,\mathrm{GaAs}} = 0.067m_0$ and AlAs $m_{x,\mathrm{AlAs}} = 0.15m_0$ is given. Due to the sharpness of the lowest quasi-bound state in the well, it can not be recognized. Contrary, the higher resonances can be clearly seen. The wave function penetration into the barriers is depicted. Near the left and right leads a high doping was used, which yields a bending of the conduction band edge. Within the well, the influence of the carriers can be seen by the deflection of the band edge.

The band edge of the resonant tunneling device is given in Figure 4.14. The electron concentration that results from the self-consistent calculation is depicted. It particularly illustrates the penetration of the electrons into the barriers and the high carrier concentration in the quantum well due to the quasi-bound states that appear in this region.
To depict the current, that is carried by the resonant states, the current density spectrum at a bias of 0.46 V is given in a semi-logarithmic plot. It shows that most of the current is provided through the sharply peaked resonances. The contribution of the first resonance is much lower, since its energy lies below the conduction band edge of the left lead, as seen in Figure 4.13. The quasi-bound states above the third resonance can not contribute to the current, because the electrons have not occupied this states yet, since their energy is too high for this bias. Therefore, only the second quasi-bound state, that is in resonance with the contact region, and the third quasi-bound state can be seen in the range of the illustrated eight decades.

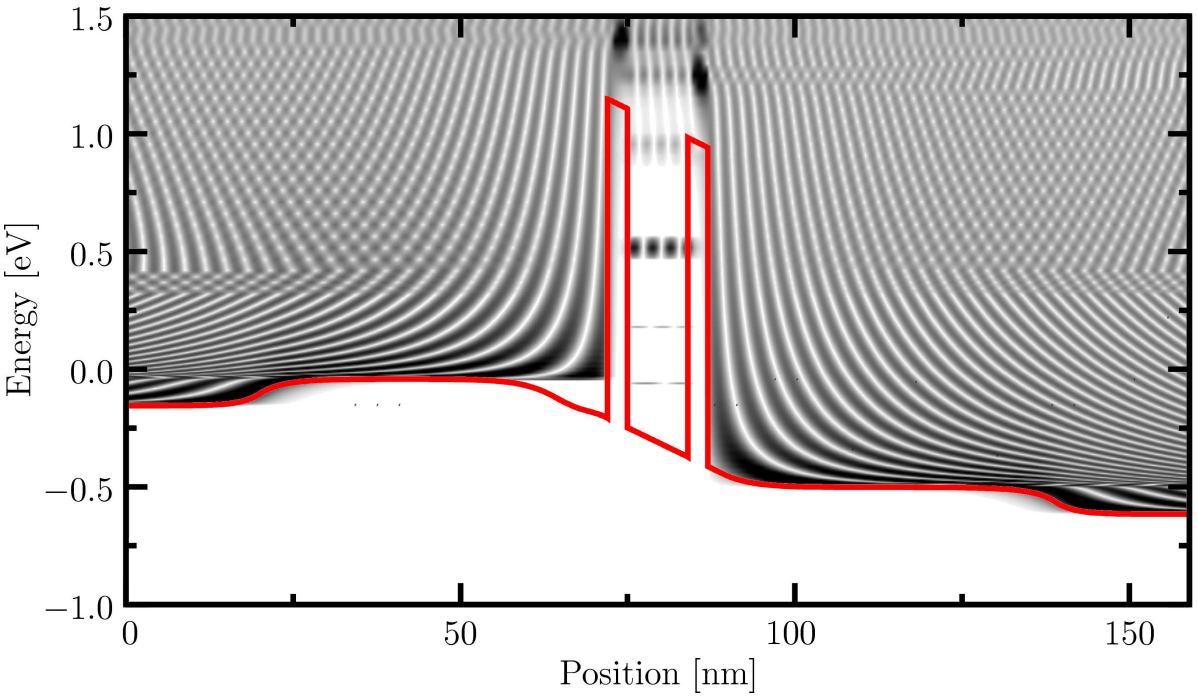

Figure 4.11: Self-consistent calculation of the local density of states for the resonant tunneling device biased in the second resonance at 0.46 V.

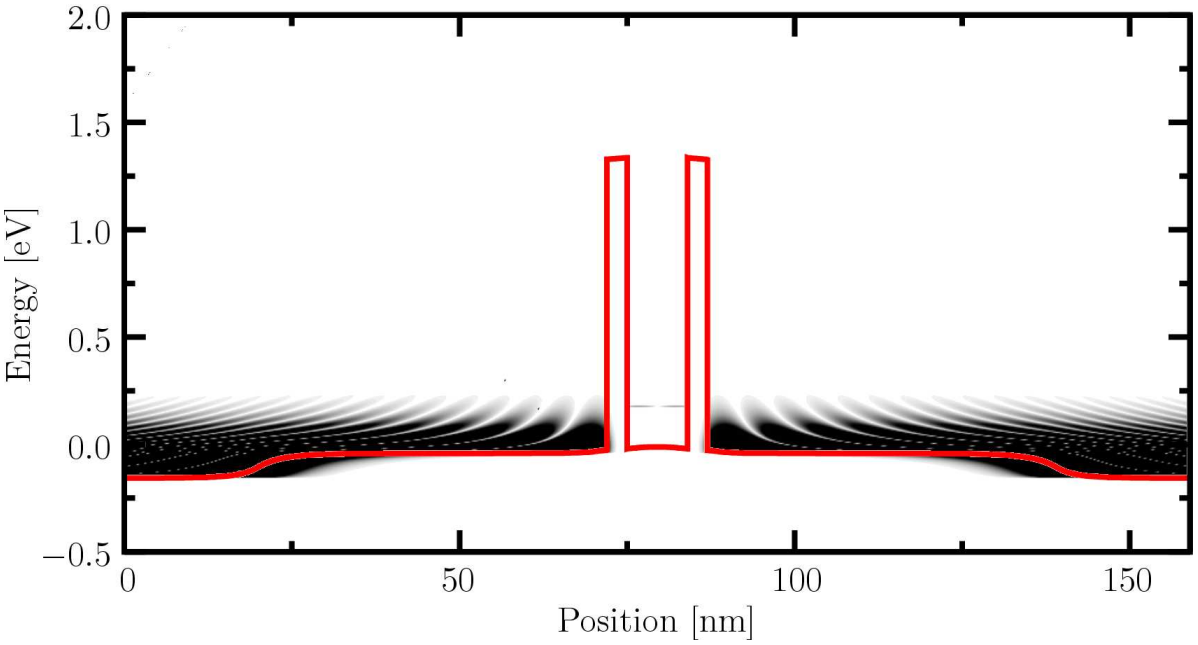

Figure 4.12: Self-consistent calculation of the occupied density of states for the resonant tunneling device without bias. Only the second resonant level is noticeably occupied.

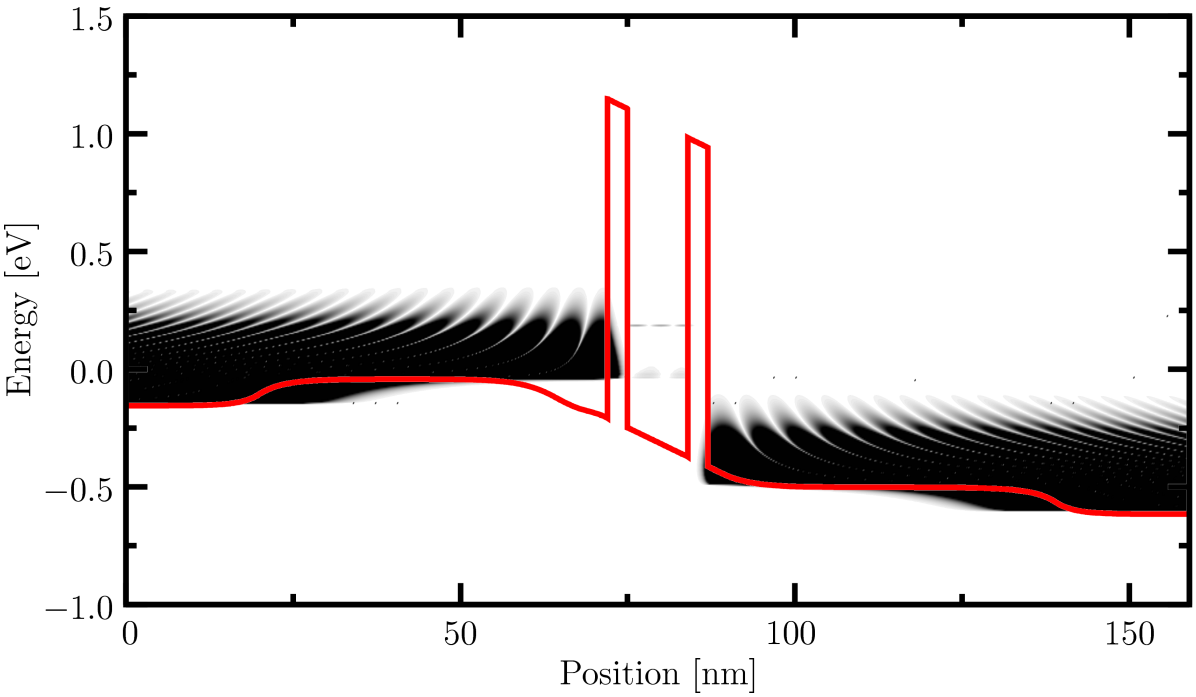

Figure 4.13: Self-consistent calculation of the occupied density of states for the resonant tunneling device biased in the second resonance at 0.46 V.

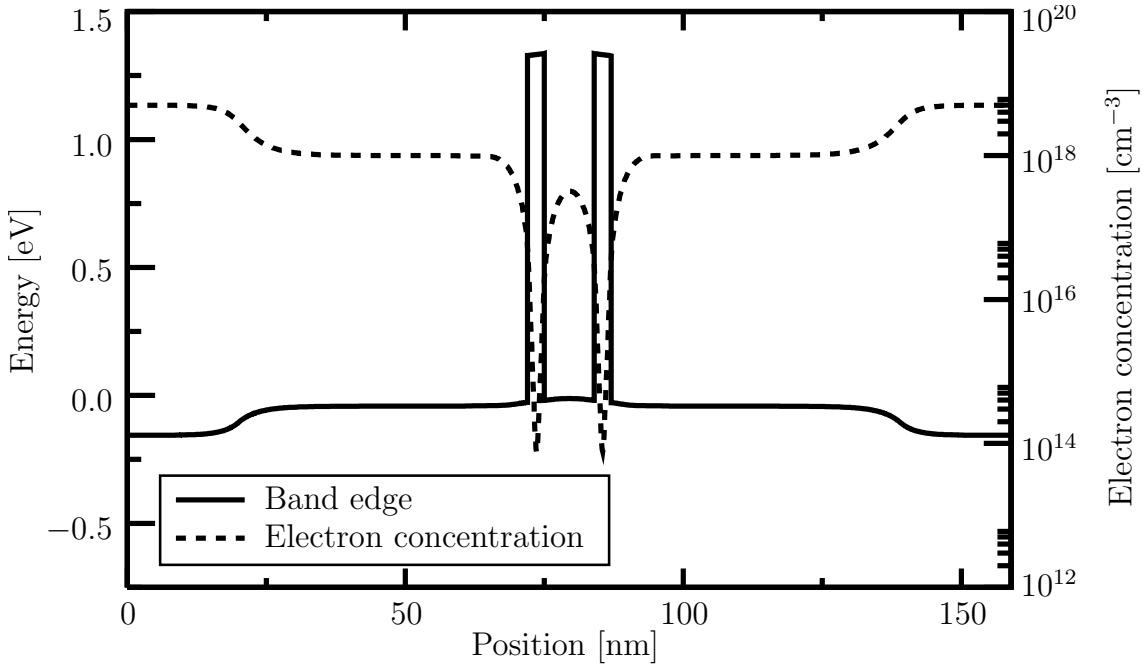

Figure 4.14: Self-consistent calculation of the band edge and the carrier concentration of the resonant tunneling device.

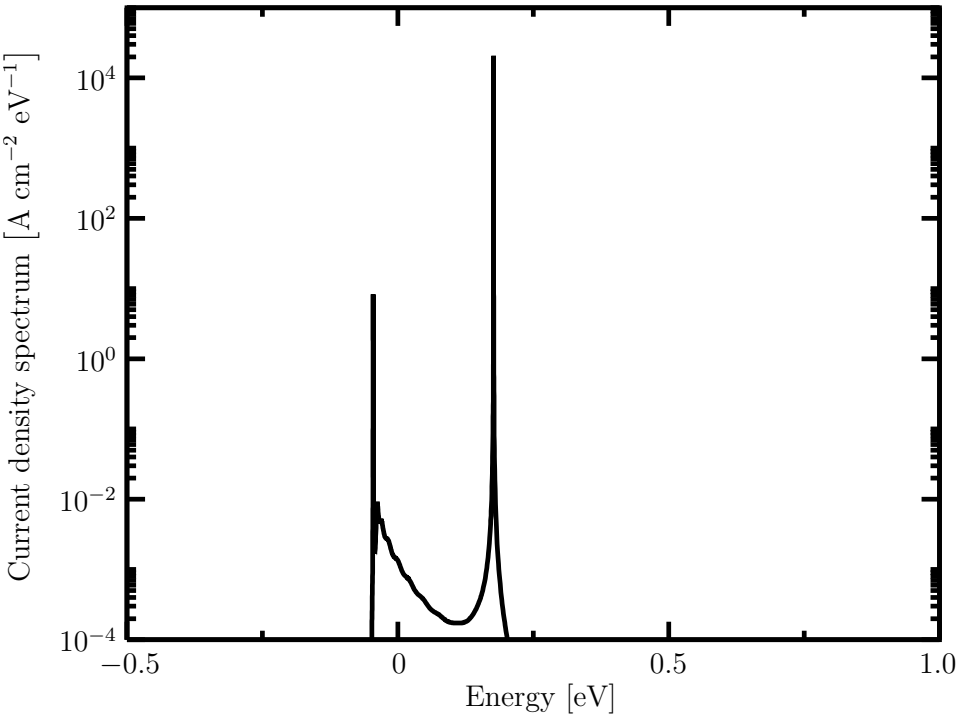

Figure 4.15: Current density spectrum of the resonant tunneling device. The bias of 0.46 V leads to a high current at the energy of the second resonant level as well as the third quasi-bound-state.

The current-voltage characteristic for the resonant tunneling device with three different well widths is given in Figure 4.16. Comparing the results of the self-consistent solution and the linear potential drop (Fig. 4.9) a more abrupt change from the peak current to the valley current in the negative differential resistance regime can be seen for the former figure.
The IV-curve shows how the peak to valley ratio of the current rises with decreasing well width due to broader resonances. Furthermore, a shorter well leads to resonances at higher energy levels. This yields the shift of the current peak to higher voltages.
The self-consistent simulation takes account of the doping of the resonant tunneling device. A Schrödinger-Poisson solver loop ensures charge neutrality and therefore adjusts the conduction band edge correspondingly. This leads to an overall higher current in the self-consistent simulation.

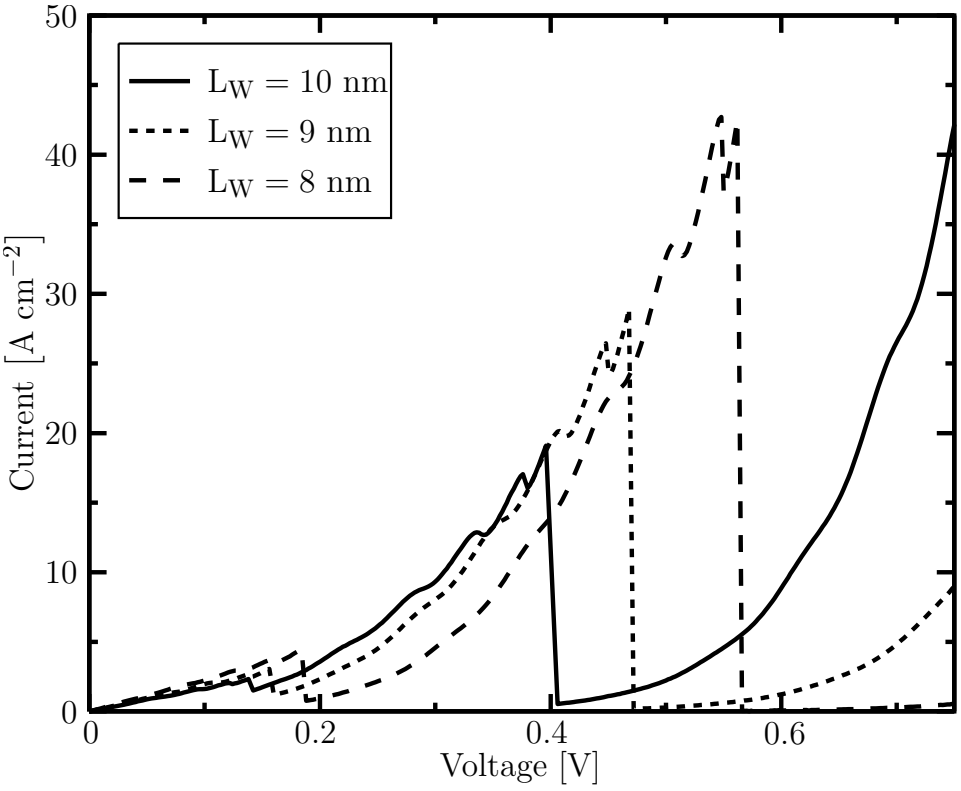

Figure 4.16: Self consistent calculation of the current-voltage characterstic of the device from Figure 4.10 with a variation of the GaAs well width. Compared to the IV characteristic of the non-self-consistent simulation, the peaks are much sharper. The higher current is a result of the charge neutrality of the ionized dopants and the free carriers by the self-consistent simulation. That yields a total shift of the conduction band edge and therefore has an effect on the current.

In all things success depends on previous preparation, and without such previous preparation there is sure to be failure.

CONFUCIUS

CHAPTER 5

Summary and Outlook

Quantum transport in systems with open boundary conditions was investigated. The non-equilibrium Green's functions formalism for one-dimensional devices was implemented within the framework of the Vienna Schrödinger Poisson solver.
Starting from the time-independent effective mass Schrödinger equation the concept of the local density of states was introduced. Assuming a Fermi-Dirac distribution function the occupation of states was derived. Tunneling through single and double barrier structures has been examined by means of the transmission formalism. The basic theory of Green's functions has been presented. Its application to solve the Schrödinger equation with emphasis on quantum transport phenomena has been pointed out. All assumptions in order to allow a numerical treatment of the non-equilibrium Green's functions formalism were stated clearly. To ensure a performant implementation of the Green's functions method an efficient recursive algorithm has been applied. A major issue of the realization is the numerical integration over the discrete energy space. In order to keep the memory requirements low an adaptive energy grid refinement proved necessary. Various quadrature rules, namely Simpson's rule, Akima interpolation, polynomial interpolation, and the Clenshaw-Curtis rule, have been examined were only the latter two were identified to be applicable for this case. To include the effects due to electrostatics, a self-consistent Schrödinger-Poisson loop is required. The developed simulation model has been applied to single and double barrier structures. As physical quantities of interest, the transmission, the local density of states, and the occupation have been evaluated. Furthermore, the current-voltage characteristics of resonant tunneling devices posing the typical negative differential resistance have been shown.
For future development, the adaption of a more sophisticated Hamiltonian could reproduce the dispersion relation for high energetic electrons and holes. Furthermore, the treatment of phase-breaking interactions to describe incoherent transport should be incorporated.

Bibliography

[1] "International Technology Roadmap for Semiconductors." http://www.itrs.net.

[2] S. Selberherr, *Analysis and Simulation of Semiconductor Devices*. Springer, 1984.

[3] M. S. Lundstrom, *Fundamentals of Carrier Transport*. Cambridge University Press, 2000.

[4] T. Grasser, T.-W. Tang, H. Kosina, and S. Selberherr, "A Review of Hydrodynamic and Energy-Transport Models for Semiconductor Device Simulation," *Proceedings of the IEEE*, vol. 91, pp. 251–274, Feb 2003.

[5] M. V. Fischetti, "Theory of Electron Transport in Small Semiconductor Devices Using the Pauli Master Equation," *Journal of Applied Physics*, vol. 83, no. 1, pp. 270–291, 1998.

[6] H. Kosina, V. Sverdlov, and T. Grasser, "Wigner Monte Carlo Simulation: Particle Annihilation and Device Applications," in *International Conference on Simulation of Semiconductor Processes and Devices*, pp. 357–360, 2006.

[7] L. P. Kadanoff and G. Baym, *Quantum Statistical Mechanics: Green's Frunction Methods in Equilibrium and Nonequilibrium Problems*. W.A. Benjamin, 1962.

[8] L. V. Keldysh, "Diagram Technique for Nonequilibrium Processes," *Soviet Physics JETP*, vol. 20, p. 1018, 1965.

[9] R. C. Bowen, G. Klimeck, R. K. Lake, W. R. Frensley, and T. Moise, "Quantitative Simulation of a Resonant Tunneling Diode," *Journal of Applied Physics*, vol. 81, pp. 3207–3213, April 1997.

[10] A. Svizhenko, M. P. Anantram, T. R. Govindan, B. Biegel, and R. Venugopal, "Two-Dimensional Quantum Mechanical Modeling of Nanotransistors," *Journal of Applied Physics*, vol. 91, pp. 2343–2354, February 2002.

[11] J. H. Davies, *The Physics of Low-Dimensional Semiconductors: An Introduction*. Cambridge University Press, 1998.

[12] M. Karner, "Multi-Dimensional Simulation of Closed Quantum Systems," Master's thesis, Technische Universität Wien, 2004.

[13] S.-E. Ungersböck, "Numerische Berechnung der Bandstruktur von Halbleitern," Master's thesis, Technische Universität Wien, 2002.

[14] D. K. Ferry and S. M. Goodnick, *Transport in Nanostructures*, vol. 6 of *Cambridge Studies in Semiconductor Physics and Microelectronic Engineering*. Cambridge University Press, 1997.

[15] W. R. Frensley, "Quantum Transport," in *Heterostructures and Quantum Devices* (N. G. Einspruch and W. R. Frensley, eds.), vol. 24 of *VLSI Electronics: Microstructure Science*, Academic Press, Inc., 1994.

[16] S. Datta, *Electronic Transport in Mesoscopic Systems*. Cambridge University Press, 1995.

[17] R. Kubo, "Statistical-Mechanical Theory of Irreversible Processes," *Journal of the Physical Society of Japan*, vol. 12, pp. 570–586, June 1957.

[18] R. Landauer, "Spatial Variation of Currents and Fields Due to Localized Scatterers in Metallic Conduction," *IBM Journal of Research and Development*, vol. 1, no. 3, p. 223, 1957.

[19] M. Büttiker, Y. Imry, R. Landauer, and S. Pinhas, "Generalized Many-Channel Conductance Formula with Application to Small Rings.," *Physical Review B: Condensed Matter*, vol. 31, pp. 6207–6215, May 1985.

[20] P. C. Martin and J. Schwinger, "Theory of Many Particle Systems.I," *Physical Review*, vol. 115, no. 6, pp. 1342 – 1373, 1959.

[21] H. Haug and A.-P. Jauho, *Quantum Kinetics in Transport and Optics of Semiconductors*, vol. 123 of *Springer Series in Solid-State Sciences*. Springer-Verlag, 1998.

[22] G. D. Mahan, *Many-Particle Physics*. Physics of Solids and Liquids, Plenum Press, 2 ed., 1990.

[23] R. Lake, G. Klimeck, R. C. Bowen, and D. Jovanovic, "Single and Multiband Modeling of Quantum Electron Transport through Layered Semiconductor Devices," *Journal of Applied Physics*, vol. 81, pp. 7845–7869, June 1997.

[24] A. Cresti, R. Farchioni, G. Grosso, and G. P. Parravicini, "Keldysh-Green Function Formalism for Current Profiles in Mesoscopic Systems," *Physical Review B*, vol. 68, p. 075306, 2003.

[25] M. Pourfath, H. Kosina, and S. Selberherr, "A Fast and Stable Poisson-Schrödinger Solver for the Analysis of Carbon Nanotube Transistors," *Journal of Computational Electronics*, vol. 5, pp. 155–159, 2006.

[26] C. S. Lent and D. J. Kirkner, "The Quantum Transmitting Boundary Method," *Journal of Applied Physics*, vol. 67, pp. 6353–6359, May 1990.

[27] S. Datta, "Nanoscale Device Modeling: The Green's Function Method," *Superlattices and Microstructures*, vol. 28, no. 4, pp. 253–259, 2000.

[28] M. P. Anantram, M. S. Lundstrom, and D. E. Nikonov, "Modeling of Nanoscale Devices," *ArXiv Condensed Matter e-prints*, October 2006.

[29] S. Datta, *Quantum Transport: Atom to Transistor*. Cambridge University Press, 2005.

[30] D. John, L. Castro, P. Pereira, and D. Pulfrey, "A Schrödinger-Poisson Solver for Modeling Carbon Nanotube FETs," in *Nanotech*, vol. 3, pp. 65–68, 2004.

[31] H. Akima, "A New Method of Interpolation and Smooth Curve Fitting Based on local Procedures," *Journal of the Association for Computing Machinery*, vol. 17, pp. 589–602, October 1970.

[32] A. Bjorck and V. Pereyra, "Solution of Vandermonde Systems of Equations," *Mathematics of Computation*, vol. 24, pp. 893–903, Oct 1970.

[33] L. Fejér, "Mechanische Quadraturen mit positiven Cotesschen Zahlen," *Mathematische Zeitschrift*, vol. 37, pp. 287—-309, 1933.

[34] C. W. Clenshaw and A. R. Curtis, "A Method for Numerical Integration on an Automatic Computer," *Numerical Mathematics*, vol. 2, pp. 197—205, 1960.

[35] J. Waldvogel, "Fast Construction of the Fejér and Clenshaw-Curtis Quadrature Rules," *BIT Numerical Mathematics*, vol. 46, pp. 195–202, 2006.

[36] M. Karner, A. Gehring, S. Holzer, M. Pourfath, M. Wagner, H. Kosina, T. Grasser, and S. Selberherr, "VSP - A Multi-Purpose Schrödinger-Poisson Solver for TCAD Applications," in *11^{th} International Workshop on Computational Electronics Book of Abstracts*, pp. 255–256, 2006.